(2)

NAVAL POSTGRADUATE SCHOOL

Monterey, California

THESIS

PRELIMINARY INVESTIGATION OF THE
SHOCK-BOUNDARY LAYER INTERACTION
IN A SIMULATED FAN PASSAGE

by

Christopher C. Collins

March 1991

Thesis Advisor: Raymond P. Shreeve

REPORT DOCUMENTATION PAGE

1a REPORT SECURITY CLASSIFICATION Unclassified	1b RESTRICTIVE MARKINGS
2a SECURITY CLASSIFICATION AUTHORITY	3 DISTRIBUTION/AVAILABILITY OF REPORT Approved for public release; distribution is unlimited
2b DECLASSIFICATION/DOWNGRADING SCHEDULE	
4 PERFORMING ORGANIZATION REPORT NUMBER(S)	5 MONITORING ORGANIZATION REPORT NUMBER(S)
6a NAME OF PERFORMING ORGANIZATION Naval Postgraduate School 6b OFFICE SYMBOL (*If applicable*) AA	7a NAME OF MONITORING ORGANIZATION Naval Postgraduate School
6c ADDRESS (*City, State, and ZIP Code*) Monterey, CA 93943-5000	7b ADDRESS (*City, State, and ZIP Code*) Monterey, CA 93943-5000
8a NAME OF FUNDING/SPONSORING ORGANIZATION 8b OFFICE SYMBOL (*If applicable*)	9 PROCUREMENT INSTRUMENT IDENTIFICATION NUMBER
8c ADDRESS (*City, State, and ZIP Code*)	10 SOURCE OF FUNDING NUMBERS Program Element No / Project No / Task No / Work Unit Accession Number

11 TITLE (*Include Security Classification*)
PRELIMINARY INVESTIGATION OF THE SHOCK-BOUNDARY LAYER INTERACTION IN A SIMULATED FAN PASSAGE

12 PERSONAL AUTHOR(S) Collins, Christopher Clay

13a TYPE OF REPORT	13b TIME COVERED	14 DATE OF REPORT (*year, month, day*)	15 PAGE COUNT
Engineer's Thesis	From To	March 1991	130

16 SUPPLEMENTARY NOTATION
The views expressed in this thesis are those of the author and do not reflect the official policy or position of the Department of Defense or the U.S. Government

17 COSATI CODES			18 SUBJECT TERMS (*continue on reverse if necessary and identify by block number*)
FIELD	GROUP	SUBGROUP	Shock-Boundary Layer Interaction Transonic Cascade Wind Tunnel Transonic Cascade Flow Computation

19 ABSTRACT (*continue on reverse if necessary and identify by block number*)

A two dimensional, two passage simulation of the relative flow through a transonic fan at M = 1.4 was designed with a view to providing an apparatus in which to assess the effectiveness of passive vortex generator techniques in alleviating shock-boundary layer interaction effects. The design of the model and the results of six test runs in the transonic cascade blowdown wind tunnel are described. Schlieren photographs of the shock structure were obtained at back pressures lower than the design value. The back-pressure control valve was identified as being critical to completing the experimental simulation. The flow through the cascade gemetry was computed at design pressure ratio using an Euler code. Modifications to the grid are recommended before thin-layer Navier-Stokes calculations are performed.

NO SOFTWARE DEVELOP PER TELECON
RAYMOND SHREEVE NPS/AA/SF

NWW 11/19/91

20 DISTRIBUTION/AVAILABILITY OF ABSTRACT	21 ABSTRACT SECURITY CLASSIFICATION	
☒ UNCLASSIFIED/UNLIMITED ☐ SAME AS REPORT ☐ DTIC USERS	Unclassified	
22a NAME OF RESPONSIBLE INDIVIDUAL Raymond P. Shreeve	22b TELEPHONE (*Include Area code*) (408) 646-2593	22c OFFICE SYMBOL AA/SF

DD FORM 1473, 84 MAR — 83 APR edition may be used until exhausted / All other editions are obsolete — SECURITY CLASSIFICATION OF THIS PAGE
Unclasssified

Approved for public release; distribution is unlimited.

Preliminary Investigation of the
Shock-Boundary Layer Interaction in a Simulated Fan Passage

by

Christopher C. Collins
Lieutenant , United States Navy
B.S.E.E., United States Naval Academy, 1984

Submitted in partial fulfillment
of the requirements for the degree of

AERONAUTICAL AND ASTRONAUTICAL ENGINEER

from the

NAVAL POSTGRADUATE SCHOOL
March 1991

Author: Christopher C Collins
Christopher C. Collins

Approved by: Raymond P Shreeve
Raymond P. Shreeve, Thesis Advisor

Garth Hobson, Second Reader

John Ekaterinaris, Second Reader

E.R. Wood
Dr. E.R. Wood, Chairman
Department of Aeronautical Engineering

Richard S. Elster
Dr. Richard Elster, Dean of Instruction

ABSTRACT

A two-dimensional, two-passage simulation of the relative flow through a transonic fan at M = 1.4 was designed with a view to providing an apparatus in which to assess the effectiveness of passive vortex generator techniques in alleviating shock-boundary layer interaction effects. The design of the model and the results of six tests in the transonic cascade blowdown wind tunnel are described. Schlieren photographs of the shock structure were obtained at back pressures lower than the design value. The back-pressure control valve was identified as being critical to completing the experimental simulation. The flow through the cascade geometry was computed at design pressure ratio using an Euler code. Modifications to the grid are recommended before thin-layer Navier-Stokes calculations are performed.

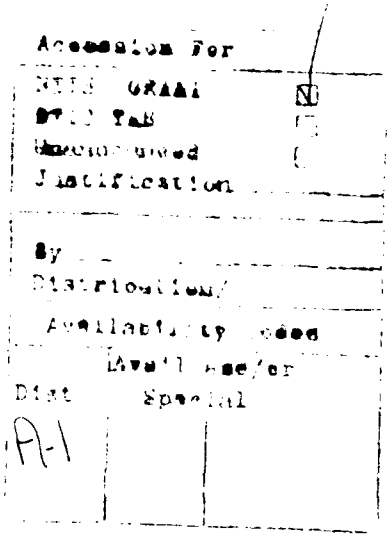

TABLE OF CONTENTS

I. INTRODUCTION 1

A. SHOCK-BOUNDARY LAYER INTERACTION 1

B. VORTEX GENERATING DEVICES 2

1. Vortex Generators 3

2. Vortex Generator Jets 4

C. 2-D FAN PASSAGE SIMULATION 6

II. EXPERIMENTAL SIMULATION 8

A. TRANSONIC CASCADE WIND TUNNEL 8

1. Wind Tunnel Description 8

2. Data Acquisition System 9

3. Optical System 10

B. TEST SECTION DESIGN 10

1. Design of the Blading 10

2. Design of the Side Pieces, Inner Plates and Windows 11

C. EXPERIMENTAL RESULTS 12

III. NUMERICAL SIMULATION 15

A. COMPUTATIONAL SCHEME 15

B. GRID GENERATION 15

C. COMPUTED RESULTS 16

IV. DISCUSSION OF RESULTS 18

A. EXPERIMENTAL 18

B. NUMERICAL 19

V. CONCLUSIONS AND RECOMMENDATIONS 21

APPENDIX A. MACHINE DRAWINGS OF TEST SECTION COMPONENTS . 57

APPENDIX B. DATA ACQUISITION PROGRAM 70

APPENDIX C. PROGRAM TO DRAW A WEDGE-ARC CASCADE 73

APPENDIX D. DESCRIPTION OF THE NUMERICAL METHOD 75

A. REYNOLDS-AVERAGED NAVIER-STOKES EQUATIONS 75

B. TURBULENCE MODELING 79

1. Baldwin-Lomax Model 79

2. Johnson-King Model 80

C. COMPUTATIONAL METHOD 82

1. Discontinuous Solutions and Entropy Method 82

2. Upwinding Schemes for Linear Hyperbolic PDE's 87

3. Conservative Schemes and Shock-Capturing Theory 89

a. Monotone Schemes 90

b. TVD Schemes 92

4. Development of Flow Simulation Code 94

APPENDIX E. GRAPE 104

APPENDIX F. GRAPE INPUT FILES 107

LIST OF REFERENCES 113

INITIAL DISTRIBUTION LIST 117

LIST OF TABLES

TABLE IA. Run 001 Pressure Data, $p_2/p_1 = 0.765$ 23

TABLE IB. Run 001 Pressure Data, $p_2/p_1 = 1.39$ 23

TABLE IC. Run 006 Pressure Data, $p_2/p_1 = 1.97$ 23

LIST OF FIGURES

Figure 1. Shock-Induced Separation on a Fan Blade [Ref. 1] 24

Figure 2. Vortex Generator Configurations [Ref. 2] 25

Figure 3. Typical Surface Pressure Distribution in the Interaction Region 26

Figure 4. Vortex Generator Jets Configuration [Ref. 2] 27

Figure 5. Cascade Geometry 28

Figure 6. Schematic of Transonic Cascade Wind Tunnel 29

Figure 7. RHS of Transonic Cascade Wind Tunnel 30

Figure 8. LHS of Transonic Cascade Wind Tunnel 31

Figure 9. *Test Section Interior (w/o blades)* 32

Figure 10. Schematic of Back Pressure Valve 32

Figure 11. Back Pressure Valve 33

Figure 12. Control Valve 34

Figure 13. Control Panel 34

Figure 14. Schematic of the Data Acquisition System 35

Figure 15. Data Acquisition System 36

Figure 16. Schematic of Optical System 37

Figure 17. LHS of Optical System 38

Figure 18. Schematic of Test Section 39

Figure 19. Test Section Inner Wall and Center Blade 40

Figure 20. Test Section Upper Blade 41

Figure 21. Test Section Lower Blade 42

Figure 22. Test Section Inner Plate and Model Blade 43

Figure 23. Test Section Side Piece 44

Figure 24. Run 001 Schlieren - $p_2/p_1 = 0.765$ 45

Figure 25. Run 001 Schlieren - $p_2/p_1 = 1.39$ 45

Figure 26. Channel C-grid 46

Figure 27. Cascade C-grid 47

Figure 28. Detailed View of Cascade C-grid 48

Figure 29. Detail of Leading Edge of Cascade C-grid 49

Figure 30. Detail of Trailing Edge of Cascade C-grid 50

Figure 31. Multiple Plot Cascade C-grid 51

Figure 32. Detailed View of Boundary Area 52

Figure 33. Channel Flow Mach Number Contours 53

Figure 34. Cascade Flow Mach Number Contours 54

Figure 35. Cascade Flow Pressure Contours 55

Figure 36. Cascade Blade Surface C_p Distribution 56

Figure A1. Test Section Side Piece 58

Figure A2. Test Section Inner Frame 59

Figure A3. Test Section Inner Frame and Blades 60

Figure A4. Detailed View of Side Piece Slot 61

Figure A5. Side Piece Window Retainer Frame 62

Figure A6. Side Piece Window 63

Figure A7. Sectioned View of Window Section 64

Figure A8. Detailed View of Window Slot 65

Figure A9. Test Section Top Blade 66

Figure A10. Test Section Middle Blade 67

Figure A11. Test Section Lower Blade 68

Figure A12. Pressure Tap Locations on Lower Blade 69

Figure B1. Data Acquisition Program TXC001 70

Figure B1 (cont). Data Acquisition Program TXC001 71

Figure B1 (cont). Data Acquisition Program TXC001 72

Figure C1. Cascade Geometry Program SSCB03 73

Figure C1 (cont). Cascade Geometry Program SSCB03 74

Figure D1. Comparison of Turbulence Model Predictions [Ref. 23] 102

Figure D2. Viscous Flow Validation [Ref. 23] 103

Figure F1. GRAPE Input for Channel C-grid 110

Figure F1 (cont). GRAPE Input for Channel C-grid 108

Figure F1 (cont). GRAPE Input for Channel C-grid 109

Figure F2. GRAPE Input for Cascade C-grid 110

Figure F2 (cont). GRAPE Input for Cascade C-grid 111

Figure F2 (cont). GRAPE Input for Cascade C-grid 112

ACKNOWLEDGEMENTS

I would like to extend my acknowledgements in particular to the following people without whom I would have not accomplished as much as I have.

Professor Raymond Shreeve: For his unselfish guidance and support as my Thesis Advisor

Garth Hobson: For his help with GRAPE and grid generation

John Eketerinaris: For his development of my understanding of numerical schemes

Don Harvey: For his superb craftsmanship in machining the test section components

Rick Still: For his tireless support on all technical matters

Pat Hickey, Ted Best and Alan McGuire: For their support whenever necessary and finally,

Kathleen Collins: For her unfailing devotion through many long days and nights Thank you very much.

I. INTRODUCTION

A. SHOCK-BOUNDARY LAYER INTERACTION

The motivation for the present study is as introduced in Ref. 1:

Outboard of approximately 50-60% span on current fan designs, the peak relative Mach Number reaches 1.3. There is a normal shock wave that stands in front of the passage that is of sufficient strength to separate the boundary layer on the suction side, as shown in Fig. 1. Depending on the strength of the shock-boundary layer interaction, the boundary layer may or may not reattach itself to the suction side. As a result of this separation, there is little or no pressure recovery downstream of the shock and there are high total pressure losses. If this separation is able to be suppressed, which would improve the boundary layer characteristics downstream of the shock, the stage pressure rise would increase and the fan efficiency would improve. In addition, the fan rotation speed could increase, allowing a reduction in size and weight and more efficient turbine speeds.

A diagram of the basic flow features of the shock-boundary layer interaction are shown at the bottom of Fig. 1. The step increase across the shock cannot be handled by the subsonic portion of the boundary layer; therefore, this pressure rise is partially transmitted upstream through the subsonic region. This results in the divergence of the stream lines and formation of compression waves upstream of the shock. If the shock

pressure rise is sufficiently strong, the boundary layer will separate and cause a more severe thickening of the upstream boundary layer. This will cause the coalescence of the compression waves into the leading shock. In order for the flow to turn back towards the axial direction, a rear shock is formed. The leading and rear shock combination is called the lambda foot. The total pressure loss through the lambda foot is lower than the loss across the normal shock, resulting in a free shear layer originating at the shock triple point. The undisturbed boundary layer thickness at the shock location, δ_0, is the normalizing length used in describing the geometry of the interaction.

Recent experiments have examined several concepts which have been proposed for suppressing the induced separation caused by the shock-boundary layer interaction. Three methods investigated at the United Technologies Research Center (UTRC) include low-profile vortex generators, a porous wall with a passive cavity and surface contouring [Ref. 1]. Additional methods examined at the NASA Langley Research Center include large eddy breakup Devices (LEBU) at small angle of attack, spanwise cylinders and vortex generator jets [Ref. 2]. The most promising and adaptable for modern transonic cascades are the vortex generators and the vortex generator jets.

B. VORTEX GENERATING DEVICES

One proposed method for supressing or eliminating the shock-induced separation is by the replenishment of the boundary layer momentum near the surface [Ref. 2]. Replenishment can be effected by a redirection of the momentum in the free stream or outer region of the boundary layer into the near-wall flow. A mechanism for effecting

the momentum transfer is via the introduction of streamwise vorticity. Such a momentum exchange in the boundary layer can enable the layer to adjust to the sudden pressure rise without separation [Ref. 1]. Various techniques can be used to introduce streamwise vorticity. Two techniques, vortex generators and vortex generator jets, are described in the following sections.

1. Vortex Generators

Passive vortex generators with a height on the order of the boundary layer thickness have long been known to increase the mixing between external streams and the boundary layer. Such vortex generators, producing relatively large streamwise trailing vortices, have been used effectively to delay boundary separation, to enhance aircraft wing lift and to avoid or delay separation in subsonic diffusers [Ref. 2]. However, because of the fullness of the mean velocity profile of high Reynolds Number turbulent boundary layers, a reduction of the height of the vortex generators to a fraction (25-50%) of the boundary layer height has been proposed [Ref. 2]. The small profile offers smaller perturbations to the supersonic freestream. Also, they are rugged in design, capable of withstanding centrifugal loads and other harsh conditions. Lastly, they have demonstrated a working flow incidence of $\pm 5°$ [Ref. 1]. The low-profile vortex generators, shown in Fig. 2, were tested in a flow in which the boundary layer was approximately 1.28 in. thick. They include the doublet and the wishbone [Ref. 2]. Other designs include the asymmetric candleflame and the singlet (a doublet with the second wedge removed) [Ref. 1].

UTRC investigated the effects of low-profile vortex generators on suppressing shock-induced separation in a slowly diverging circular duct. Details of the experiment

are found in Ref. 1. The shock position within the duct was controlled using a translating plug valve following the test section. Wall pressure distributions through the interaction region were obtained and surface flow structure was observed using an oil flow technique.

The results showed that the pressure rise increased towards the ideal value when vortex generators were attached upstream, and the region of the pressure rise was shortened. Thus the shock-induced separation was substantially reduced. Depending on the configuration of vortex generators, the shock-boundary layer interaction length could be shortened by approximately 50%. Also, the displacement and momentum boundary layer thicknesses downstream were substantially reduced. A sketch which illustrates changes in the pressure recovery obtained with vortex generators is shown in Fig. 3 in comparison with the ideal pressure recovery and the baseline pressure recovery.

Of the remaining methods of suppressing shock-induced separation investigated in Ref. 1, the porous wall with the passive cavity did reduce the shock loss, but the boundary layer development was aggravated. Also, significant mixing losses occured downstream. The use of surface contouring moderately reduced the boundary layer thickness, but did not affect the size of the separation region.

2. Vortex Generator Jets

The use of vortex generator jets was first proposed by Wallis [Ref. 3] in Australia. The vortex jets are usually, but not as intended here, an active method where jets of air are blown through holes in the solid surface. The holes are inclined at an angle to the surface and skewed with respect to the freestream. A schematic of the arrangement (taken from Ref. 2) is shown in Fig. 4. The arrangement of the jets on the surface is

much like the arrangement of solid vortex generators. The relatively weak counter-rotating vortices that are formed within the jet fluid in crossflow are replaced by a stronger streamwise vortex trail in the ambient fluid downstream of injection and close to the surface [Ref. 2].

Vortex generator jets have proven effective in reducing the extent of the turbulent boundary layer separation resulting from adverse pressure gradients. However, the status is summarized in the following points stated in Ref. 4:

- The feasibility of the technology is not firmly established
- It is possible to adapt the arrangement passively to fans because of the cascade arrangment
- There is a negligible drag penalty of the vortex generator jets when compared to the vortex generators when the jets are off.

The effect of skewed jets and their relative angles (θ) to the freestream on separation in a subsonic diffusing flow were investigated in Ref. 4. The jets were skewed 45° to the vertical and θ was varied from 0° (downstream) to 180° (upstream). The following conclusions were reached.

- Substantial reduction of the size of the stall region size occurred for jet velocity ratios > 0.8.
- Jets pointing directly upstream were ineffective due to weak vortex formation.
- Jet arrays that cause counter-rotating vortex pairs can cause significant spanwise variations.
- Spanwise average reattachment location seems to be more strongly affected than the detachment location

C. 2-D FAN PASSAGE SIMULATION

The promising results of the UTRC experiment suggested the need for an evaluation of the concept in an actual transonic fan configuration. A full-scale simulation would be desirable, but such an experiment has the potential problem of not being definitive because of extreme difficulty in measurement and, therefore, in adequately assessing the results. Hence, a steady 2-D stream-surface simulation was undertaken in the present study. The combination of an experimental and computational simulation was the approach taken in an attempt to establish a representative baseline flow geometry in which to verify the effectiveness of the proposed vortex generators in alleviating the shock-induced separation.

The geometry for the 2-D experiment was a simulation of the relative flow on an advanced fan rotor at approximately 63% of the span. The 2-D model used in the experiment was based on the stream surface geometry, but the blade profile was approximated (closely) as a wedge arc for ease in manufacture. This was a logical step since steamline contraction could not be simulated in the experiment. The geometry of the 2-D simulation is shown in Fig. 5.

In reporting the generation of the baseline flow geometry in the present document, Section II describes the experimental simulation and Section III describes the numerical simulation. As originally conceived, from the experimental simulation, measurements of surface pressures and schlieren photographs of the shock-boundary layer interaction were to be obtained. Measured boundary pressures were then to be used as input boundary

conditions for the numerical simulation, and a comparison could be made of both shock-boundary layer interaction structure and distribution of surface pressure. However, as described in the results given in Section IV, while the experimental apparatus was relatively successful, it could not be operated at sufficiently high back-pressures (>2x upstream) to produce a proper simulation of the fan shock structure at design conditions. Also given in Section IV are the results of a computation of the flow for the design pressure ratio of 2.28 using an Euler code. It was noted that, in the absence of viscosity in the code calculations at design pressure ratio, and with too low a back-pressure in the experiment, both computation and schlieren results showed qualitative agreement for shock structure at the entrance to the passage. It was concluded, in Section V, that improvement (through a refinement in the design of the valve) in the control of the back-pressure is required to properly simulate fan conditions. Grid refinement is required to continue the computational simulation.

Details of the experiment are given in Appendices A - C and details of the numerical approach and the grid generation code are given in Appendices D - F.

II. EXPERIMENTAL SIMULATION

A. TRANSONIC CASCADE WIND TUNNEL

1. Wind Tunnel Description

The original specifications, design and construction of the Transonic Cascade Wind Tunnel are described in Ref. 5. Subsequent modifications to the tunnel are described in Ref. 6.

The apparatus is a blowdown device with a design Mach number of 1.4 and a design total pressure of 50 psia. A schematic of the Transonic Cascade Wind Tunnel is shown in Fig. 6. The tunnel was relocated (to Bldg. 216 at NPS) and operated with a new 300 psia air supply system in the course of the present work. A photograph of the right hand side of the wind tunnel is shown in Fig. 7, and a photograph of the left hand side is shown in Fig. 8. A tubular flow straightener is used to remove the swirl induced by the upstream pipe bends and the control valve. The settling chamber is composed of a flat, perforated plate diffuser followed by a screen to reduce the turbulence level and promote flow uniformity. There is a round (10 in. diameter) to rectangular (2.0 in x 4.5 in) transition section from the settling chamber to the supersonic nozzle. The tunnel uses a 2-dimensional converging-diverging nozzle to accelerate to M = 1.4. A photograph of the interior of the test section (without blades) is shown in Fig. 9. Aft of the test section is a back pressure valve that is used to adjust the shock location within the test model. The back pressure valve is a "ramp and drum" throttle valve with the ramp actuated after

the flow "starts" by a pneumatic cylinder. A schematic of the back pressure valve is shown in Fig. 10, and a photograph of the exterior of the valve is shown in Fig. 11. The exhaust is ducted to a sound suppressor outside of the building. The tunnel start-up is controlled by a pneumatic control valve. A photograph of the control valve is shown in Fig. 12, and a photograph of the control panel is shown in Fig. 13.

2. Data Acquisition System

The data acquisition system used in the experiment is described in detail in Ref. 7. A schematic of the system is shown in Fig. 14, and a view of the system is shown in Fig. 15. The BASIC code used to record the tunnel reference pressure measurements (using an uninstrumented bottom blade) is given in Appendix B, Fig. B1. The Scanivalve port number and corresponding pressure location were as follows:

- Port 1 - Atmospheric pressure
- Port 2 - Calibration pressure (50 psia)
- Port 4 - Plenum pressure
- Port 6 - Upstream static pressure
- Port 8 - Downstream static pressure

Intervening ports were vented to the atmosphere to verify that the measured pressures had time to become steady state.

3. Optical System

A schematic of the optical system is shown in Fig. 16. The system included a continuous light source schlieren system and a spark source schlieren system. The continuous light source was a 100 W mercury vapor arc lamp, and the spark source was a 200 - 300 nsec spark discharge. The parabolic lens provided a parallel light beam through the test section. The parabolic mirror, mirror 2 in Fig. 16, on the far side of the test section focused the parallel beam onto the knife edge located in front of the camera box unit. At the rear of the camera box was a viewing screen behind a shutter capable of automatic or manual operation. The minimum exposure time was one-thousandth of a second. A Polaroid film holder could be inserted into the camera box when needed. In the present experiment black-and-white Polaroid Type 52 film was used. A front surface flat mirror, mirror 1 in Fig. 10, was inserted between the continuous light source and the parabolic lens when the spark source was to be operated. Mirror one was positioned and aligned using a highly focused flashlight. Both the continuous light source and the spark source were filtered to provide high resolution schlieren photographs. A view of the left hand side of the optical system is shown in Fig. 17.

B. TEST SECTION DESIGN

1. Design of the Blading

Based on stream-surface conditions through the 3-D fan blade, the 2-D experiment was designed to retain the approximate geometry while simplifying curvatures for ease of manufacture. It was found that the stream-surface fan blade profile could be

approximated by a wedge-arc blade shape having a flat pressure side and equal leading and trailing edge radii as listed in Fig. 5. The leading and trailing edge radii were 0.015 in, and the chord of the blade was 6.000 in. The suction surface starting at the leading edge was inclined to the pressure surface at 3.5° to a point 2.85 in. along the pressure surface. The suction surface wedge was blended to the trailing edge radius by an arc of radius 13.53 in.

The test section geometry (oriented to allow the flow direction to be horizontal) was composed of three partial blades defining two blade passages, as shown in Fig 18. The top passage was to be the control passage while the bottom passage was to be used to study the effects of the vortex generators. For the experiment with the vortex generator jets, the bottom blade was for control, while holes were to be drilled in the center blade. A photograph of the model blade is shown in Fig. 19, while the machine drawing of the model blade is given in Appendix A, Fig. A10. Figures 20 and 21 show views of the upper and lower partial blades respectively, while the machine drawings of the blades are given in Appendix A, Figs. A9 and A11 respectively. Appendix A, Fig. A12, details the location of the pressure taps for the instrumented lower blade. Figure 22 shows all three blades attached to the inner plate.

2. Design of the Side Pieces, Inner Plates and Windows

The design of the test section was driven by three major considerations: nozzle wall boundary layer diversion from the nozzle, wave cancellation from the leading edges of the blades and optical accessibility. Boundary layer diversion for the top and bottom of the test section was accomplished through bleed channels above the top blade and below

the bottom blade, using existing ducting [Ref. 5]. Side wall boundary layer diversion was provided by designing an inner plate which began near the leading edges of the blades. Figure 19 shows a photograph of the inner plate and center blade, while Appendix A, Fig. A2, shows the machine drawing of the inner plate. The exhaust for the diverted side wall boundary layer was through a slot in the side piece. Figure 23 shows a photograph of the side piece and Appendix A, Fig. A1, shows the machine drawing of the side piece. Appendix A, Fig. A4, details the design of the side piece exhaust slot. In addition, the side piece and inner plate incorporated a window for optical measurements. The window was made of 3/4 in. Plexiglas, and was designed to allow viewing access to the anticipated shock-boundary interaction regions in both passages. Preliminary tests indicated that the thick Plexiglas would give acceptable schlieren quality. Lastly, the cancellation of weak waves from the leading edge was effected by adjusting bleed through a porous wall on the top of the test section forward of the top blade [Ref. 6 and 8].

C. EXPERIMENTAL RESULTS

Six test runs were made. The first experiment, Run 001, was with the back pressure valve initially completely open. The flow angle of incidence (to the suction surface) was set at 1.15^0. Figure 24 shows the continuous light schlieren photograph which was obtained. The photograph shows an oblique shock leading from the leading edge of the middle blade to the suction surface of the bottom blade. The multiple waves on the top blade are from the porous wall, which was not adjusted to reduce reflections. The parallel weaker oblique shock in the lower passage is believed to originate at the

intersection of the leading edge of the supporting tab on the middle blade and the inner frame. Once the photograph was taken the back pressure valve was slowly closed in an effort to bring the oblique shock forward. Figure 25 shows the continuous light schlieren photograph when the back pressure valve was rotated to fully close the gap between the eccentrically mounted cylinder and the (fully raised) ramp. The oblique shock is seen to have moved forward towards the leading edge in both passages. The shock appears to be near normal impinging on the boundary layer. Tables IA and IB lists the pressure recordings for Run 001.

The experimental pressure ratio p_2/p_1 was found to be 0.765 with the back pressure valve open. With the back pressure valve fully closed, $p_2/p_1 = 1.39$. Calculations for the fan geometry indicated that the pressure ratio should be 2.28 on design when a strong normal shock would exist across the blade passage. On inspection, the throat of the valve in the fully closed position when added to the spaces around the sides of the ramp gave an area which was too large to achieve the desired throttling.

Run 002 was made after the actuator was adjusted to allow the ramp and drum to fully close when the drum was actuated. However, the pressure ratio p_2/p_1 obtained in Run 002 was 1.26. No photographs were taken of this run. Run 003 was made with the actuation pressure increased to 600 psia. Again, inadequate pressure ratios were obtained. The schlieren photographs and pressure measurements (not shown) were very similar to those recorded in Run 001.

Run 004, with the ramp actuator operated at 750 psia, showed no improvement. Run 005 was run with the back-pressure valve mechanically fixed in a "closed" position

using a pipe sleeve around the actuator rod. Of concern was the possibility of the flow not starting. Although the flow was started successfully through the model, it was found that the ramp was 1/16 - 1/8 in. lower than was required to fully close, and, again, the required control was inadequate. For Run 006, the ramp was wedged in the fully up position and the spaces between the ramp and duct walls were sealed using composite material plates. During this test, a maximum back-pressure ratio $p_2/p_1 = 1.98$ was obtained before the wedge holding the pipe in place and one composite plate gave way. As the back-pressure approached 1.98, the shock location moved toward the leading edge of the blade; however, the motion was very unsteady and very sensitive to the back-pressure valve position. Table IC lists the pressures recorded in Run 006. No schlieren photograph was attempted in Run 006 in view of the need to observe the shock movement while experimenting with the valve position.

III. NUMERICAL SIMULATION

A. COMPUTATIONAL SCHEME

The computational code used in the present work was based on the thin-layer Navier-Stokes equations. The scheme used a body-fitted coordinate system, and was a full upwind algorithm based on Roe flux-difference splitting. The Baldwin-Lomax turbulence model was used except near shock impingement. The Johnson-King turbulence model was used to model the shock-induced separation. Lastly, the Osher-Chakravarthy TVD scheme for flux-limiting was used. Details of the development of the numerical code and background theory are found in Appendix D.

B. GRID GENERATION

The grid for the numerical scheme was generated using the GRAPE grid generation code, described in Appendix E. Two different grids were generated: a channel passage C-grid, to be used to carry out a preliminary calculation of the flow over a single blade between parallel walls, and a cascade C-grid, to be used to compute the flow through the simulated fan passage.

The channel passage C-grid was an 199 x 64 grid suitable for Euler calculations. The input file for use with GRAPE is shown in Appendix F, Fig. F1. Figure 26 shows the channel passage C-grid.

The cascade C-grid was generated using a modification made to GRAPE which is outlined in Appendix E. The input file for GRAPE is shown in Appendix F, Fig. F2. The grid size was 169 x 40. The cascade feature was used to obtain the necessary flow periodicity in the developed grid. Figure 27 shows the complete cascade C-grid, while Fig. 28 shows an enlarged view of the leading edge region. Figures 29 and 30 show the details near the leading and trailing edges respectively. Figure 31 shows two cascade C-grids plotted simultaneously with one grid at an offset equal to the blade spacing. This figure demonstrates the periodicity of the grid and the accuracy of the geometric specifications such as the solidity. Figure 32 shows a detailed view of the boundary between the two grids.

C. COMPUTED RESULTS

The Mach number contours for the Euler solution obtained for the flow over the single blade in a channel using the channel passage C-grid are shown in Fig. 33. The solution shown in Fig. 33 is not a steady state condition but rather a "snapshot" of the flow during a transient in which the pressure side shock was propagating towards the leading edge.

The Mach number contours for the Euler solution for the flow through the cascade C-grid are shown in Fig. 34. The angle of incidence of the flow to the suction surface was 0° and $p_2/p_1 = 2.28$. The contours show a pressure side leading edge oblique shock and a reflection from the suction surface, followed by a strong, near-normal passage shock. Figure 35 shows the pressure contours. On both sets of contours, the leading

edge disturbance does not continue to propagate smoothly across grid boundaries because of a discontinuity encountered there in the grid spacing (see Fig. 32). The calculated blade surface C_p distribution is shown in Fig. 36. This figure also demonstrates the effectiveness of flux-limiters in suppressing the oscillations that develop around the discontinuities.

IV. DISCUSSION OF RESULTS

A. EXPERIMENTAL

The oblique shock patterns within the passage, shown in Figs. 24 and 25, were observed to be qualitatively similar to the computed shock pattern shown in Fig. 34. It is noted, however, that the flow incidence to the suction surface in the experiment was 1.15° whereas it was 0° in the computation. The shock should therefore have been stronger in the experiment than in the computation, and this certainly was the case.

In the present work, the difficulties with the back-pressure valve precluded obtaining a pressure ratio $p_2/p_1 = 2.28$. However, considerable experience was gained in the attempts which were made to achieve this ratio. First, it was found that the flow could be started through the test section with the ramp fully up. This means that the ramp can be fixed rigidly to the duct wall and need not be supported by a pneumatic actuator. The rigid positioning will allow the sides of the ramp to be sealed completely and will eliminate a potential source of unsteadiness in the valve throat area.

For the brief period during Run 006 that the back-pressure was held at a value approaching twice the inlet pressure, the flow was highly unsteady. Unfortunately, the inlet pressure was dropping as the supply pressure fell, and it was not possible to experiment further. It was noted on the schlieren screen that the lower passage unstarted while the upper passage remained started, raising the possibility that the achievement of similar flows in the two passages may not be automatic.

B. NUMERICAL

The Euler solution using the cascade C-grid gave useful qualitative information on the structure of the flow field, which was supported by the experimental data. It is expected that at the same pressure ratio, the viscous solution should move the shock in the passage due to losses and the displacement effects of the boundary layer. The flow structure might still not correspond to what is expected to occur in the fan, wherein the normal shock sits at the leading edge in an "unstarted" structure. It is also possible that the computed structure is the result of the initial conditions imposed on the unsteady solution. What is found is a solution that requires a "starting" process that is not present physically in the fan application. What would be required to obtain the "unstarted" solution would be to first increase the pressure ratio to expel the shock, and then decrease the pressure ratio to the design value. It is interesting to note that this is exactly the procedure which must be followed in the experiment, which is why the back pressure control valve is such a critical component in the test apparatus.

Grid refinement is also necessary for the intended application with a viscous flow solver. The boundary layer will need to be resolved adequately with an appropriate number of grid points. Also, the orthogonality between the upper and lower boundaries of the cascade will have to be enforced more rigidly (Fig. 32). Lastly, the grid spacing will need to be more uniform to ensure continuity across boundaries (Fig. 32). Continuity in grid spacing is expected to yield more accurate propagation of shock discontinuities.

It is noted, however, that the validity of the turbulence model chosen has been demonstrated (Appendix D, Fig. D1), and a solution for an airfoil has been obtained using the viscous solver (Appendix D, Fig. D2).

V. CONCLUSIONS AND RECOMMENDATIONS

In the present study, both experimental and numerical simulations of the flow on a stream surface through a transonic fan passage were attempted with a view to providing a baseline geometry in which the effectiveness of upstream vortex generating devices in alleviating effects of shock-boundary layer interaction could be examined. From the experiment, the following were concluded:

- The design of the test section geometry was successful. No structural problems were encountered in six test runs. Boundary layer diversion slots appeared to start by natural aspiration to the atmosphere. Schlieren photographs were obtained successfully through thick Plexiglas windows.

- The upstream pressure control valve was fully satisfactory, and the transonic cascade wind tunnel was made operative in its new location.

- The downstream pressure control valve was found not to be satisfactory as originally installed and was shown to be critical to the eventual success of the experiment. It was shown that the test section flow would establish with the valve ramp fully up, so that the ramp could be made both rigid and sealed. The eccentric aluminum cylinder component did not provide adequate control because of internal leakage.

- No problem other than the back-pressure control valve was found which would prevent a successful experiment.

From the initial steps taken toward a numerical simulation, the following were concluded:

- A suitable grid for computing the cascade flow using an Euler solver was generated using GRAPE code as modified by R. Chima (Appendix E). A suitable grid for viscous calculations near this blade surface can be obtained using this code. Discontinuities in grid spacing across periodic boundaries given by the code can possibly be removed using the DSOBI parameter (Appendix E).

- The solution obtained for the experimental cascade at the design pressure ratio using an Euler solver showed a normal shock wave well inside the passage. Since the inclusion of viscous displacement effects should move the shock downstream, this solution may be the result of the assumed initial conditions.

- The oblique shock structure predicted within the passage was qualitatively similar to that observed in the schlieren photographs obtained from the experiment at lower pressure ratios.

The following are recommended to advance the experiment:

- Perfect the back pressure control valve by sealing and rigidly attaching the ramp and replacing or redesigning the eccentric drum.

- Install pressure taps in the lower blade (as designed) and connect to a high-speed scanning data system.

- Manufacture additional windows, or provide aluminum blanks for tests not requiring optical access.

- Provide a tight shut-off valve in series with the present tunnel control valve.

- Provide a safety rupture diaphragm upstream of the back pressure control valve.

The following are recommended to advance the numerical simulation:

- Ensure grid spacing continuity, orthogonality along the boundary of the grid and improved resolution in the boundary layer region for use with the viscous solver.

- Investigate the "starting" process.

- Run the Euler solver with the flow incidence at 1.15° to the suction surface.

TABLE IA. Run 001 Pressure Data, p_2/p_1 = 0.765

Port	Pressure (psia)
1	14.8
2	50.0
4	40.3
6	17.9
8	13.7

TABLE IB. Run 001 Pressure Data, p_2/p_1 = 1.39

Port	Pressure (psia)
1	14.8
2	50.2
4	22.4
6	14.3
8	19.8

TABLE IC. Run 006 Pressure Data, p_2/p_1 = 1.97

Port	Pressure
1	-
2	-
4	55.8
6	18.1
8	35.7

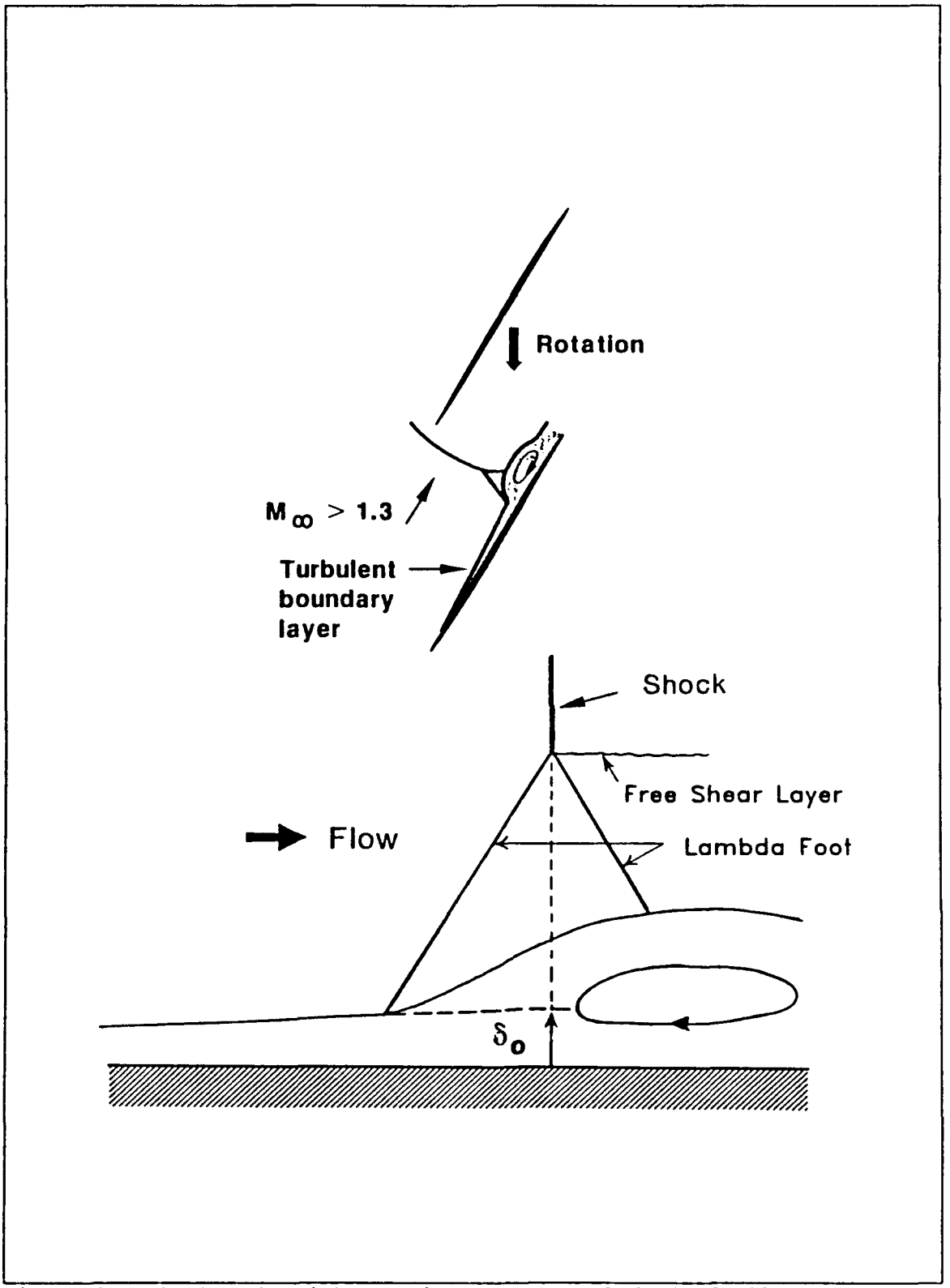

Figure 1. Shock-Induced Separation on a Fan Blade [Ref. 1]

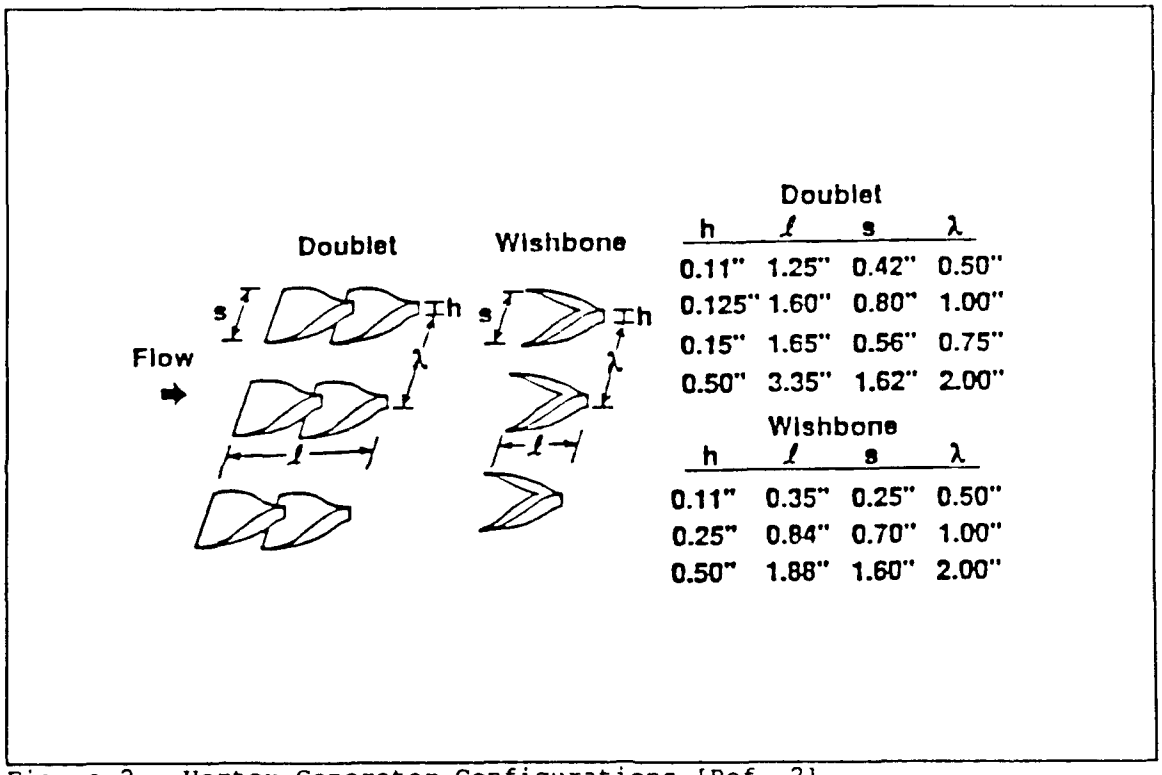

Doublet

h	l	s	λ
0.11"	1.25"	0.42"	0.50"
0.125"	1.60"	0.80"	1.00"
0.15"	1.65"	0.56"	0.75"
0.50"	3.35"	1.62"	2.00"

Wishbone

h	l	s	λ
0.11"	0.35"	0.25"	0.50"
0.25"	0.84"	0.70"	1.00"
0.50"	1.88"	1.60"	2.00"

Figure 2. Vortex Generator Configurations [Ref. 2]

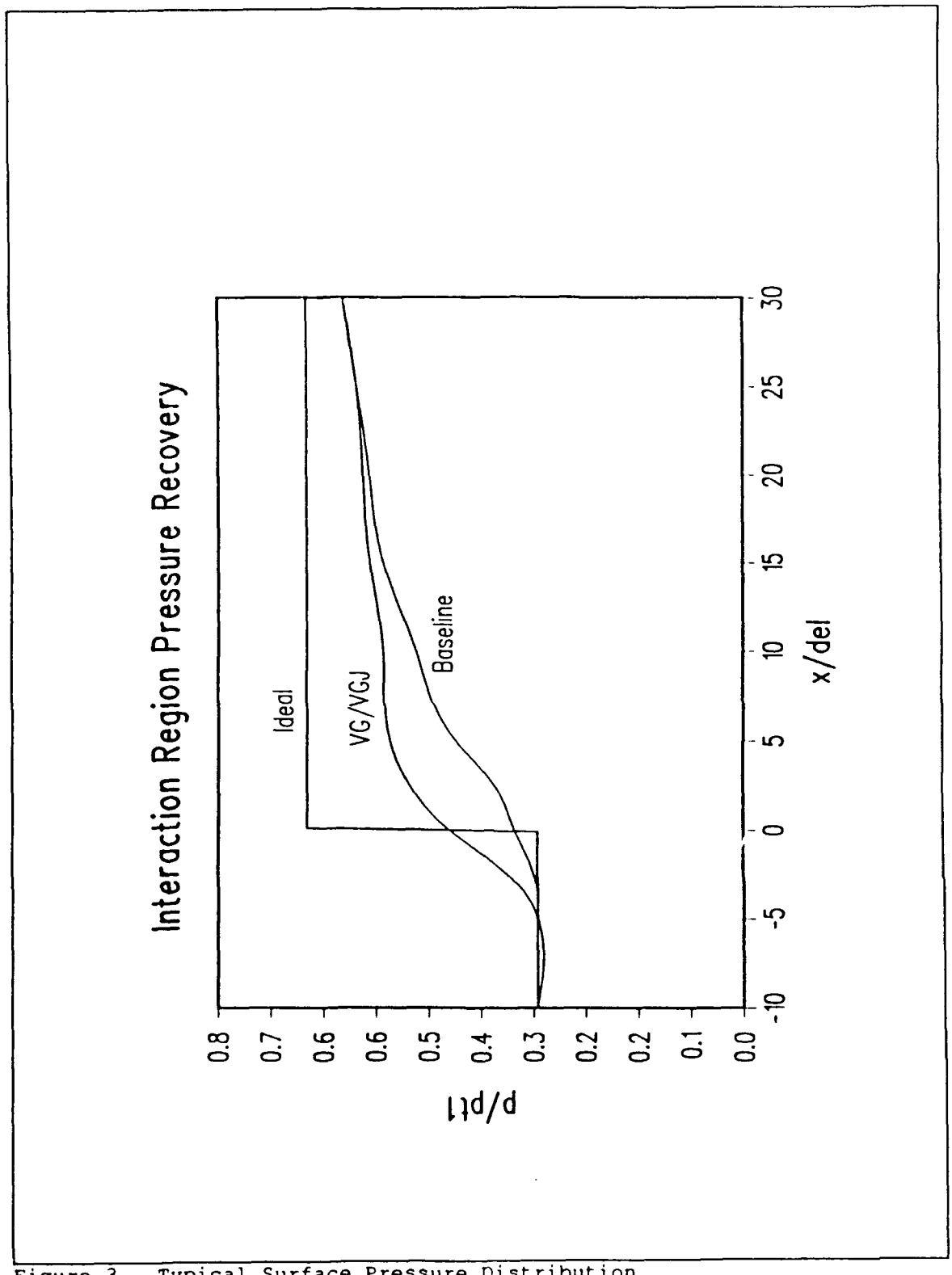

Figure 3. Typical Surface Pressure Distribution in the Interaction Region

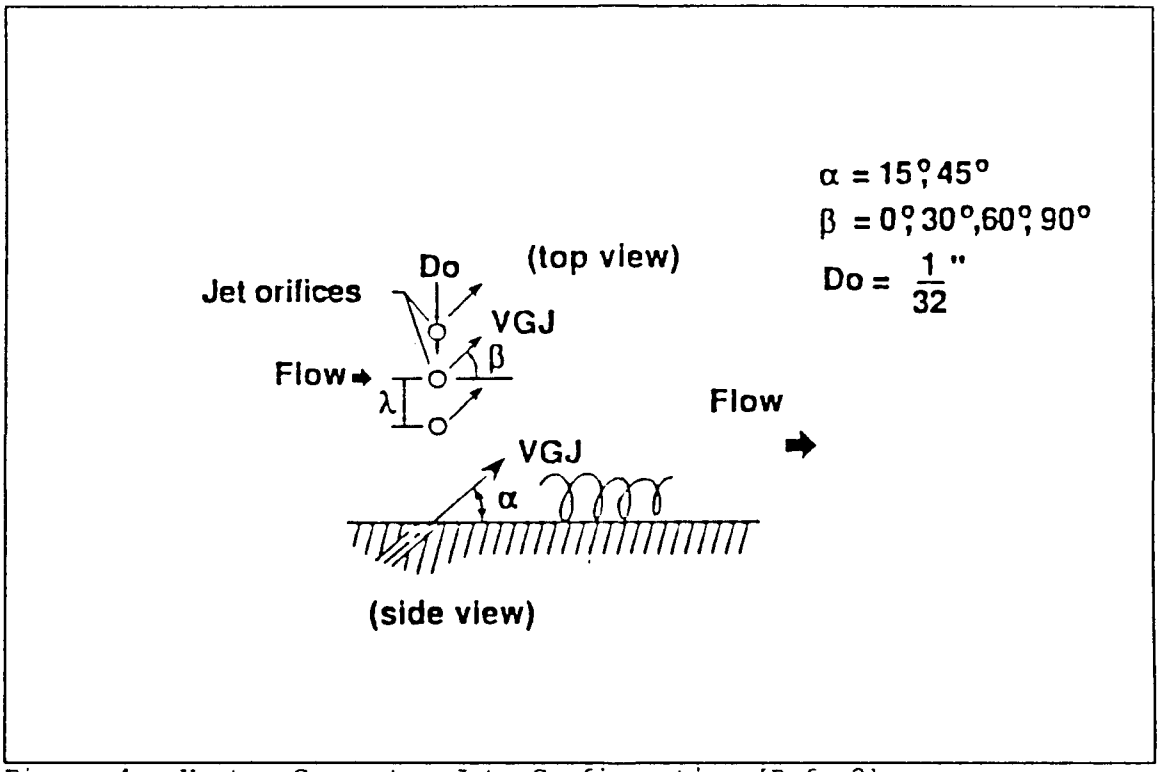

Figure 4. Vortex Generator Jets Configuration [Ref. 2]

Blade Geometry

L.E. Radius	= 0.015 in
T.E. Radius	= 0.015 in
Wedge Angle	= 3.5°
Wedge Length	= 2.85 in
Suction Surface Arc Radius	= 13.53 in

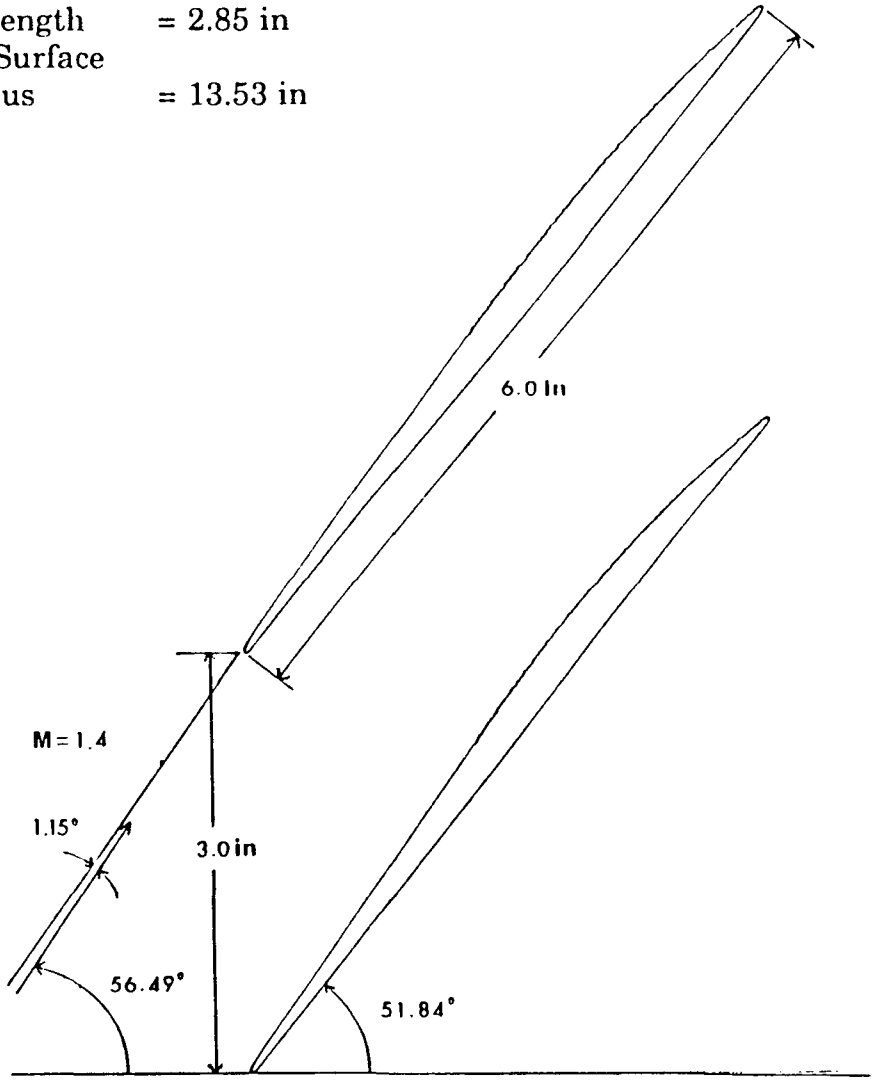

Figure 5. Cascade Geometry

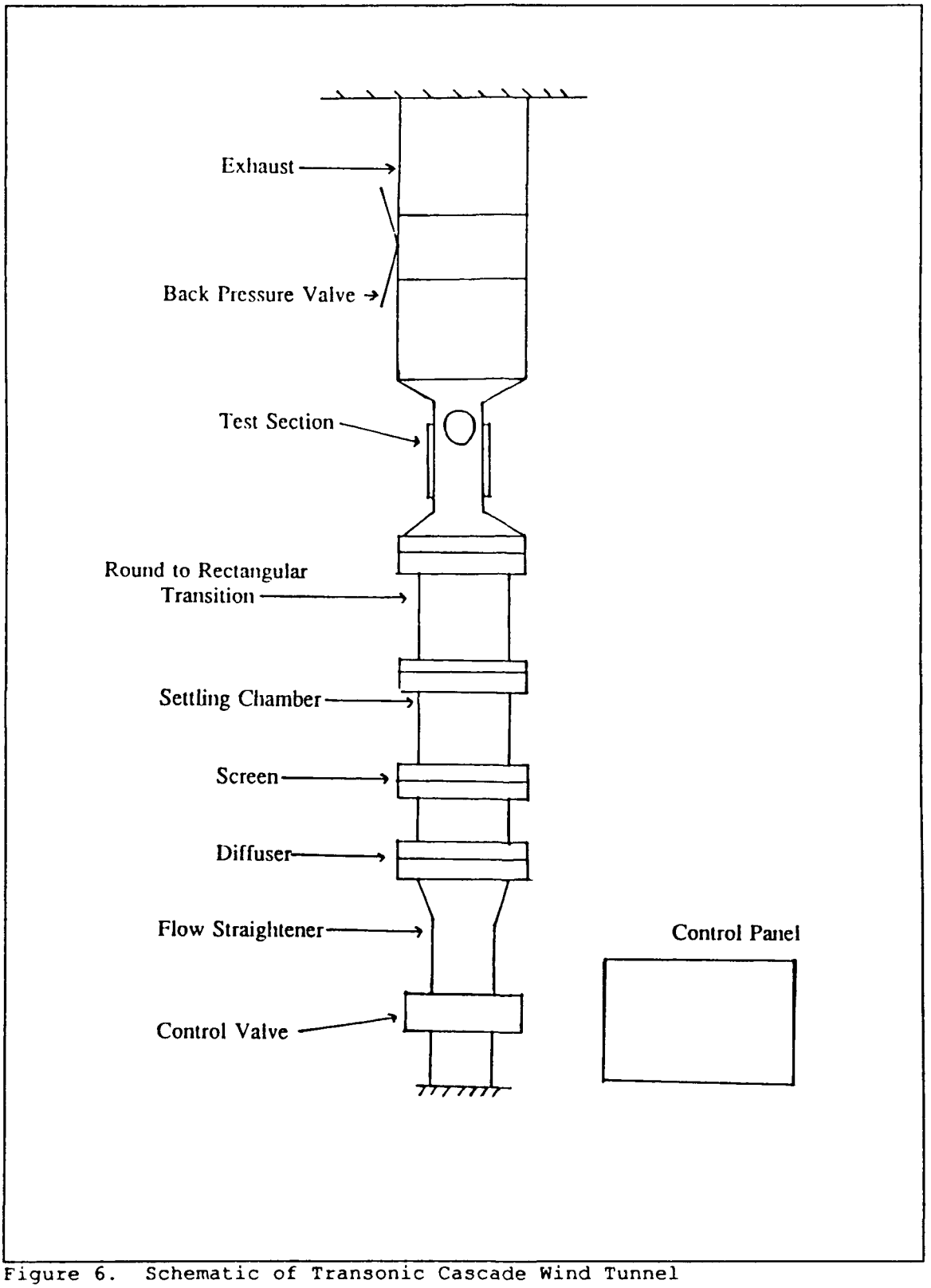

Figure 6. Schematic of Transonic Cascade Wind Tunnel

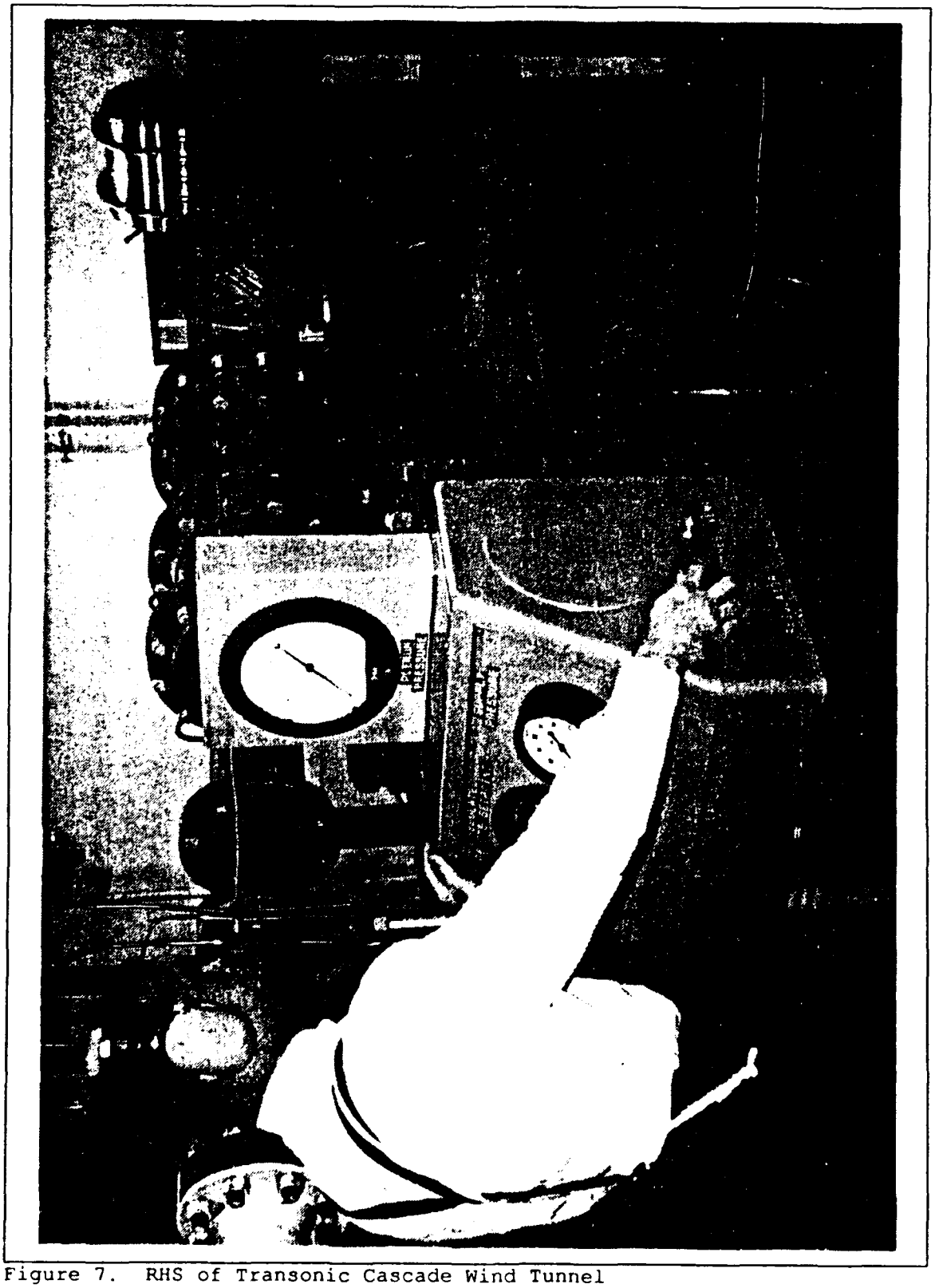

Figure 7. RHS of Transonic Cascade Wind Tunnel

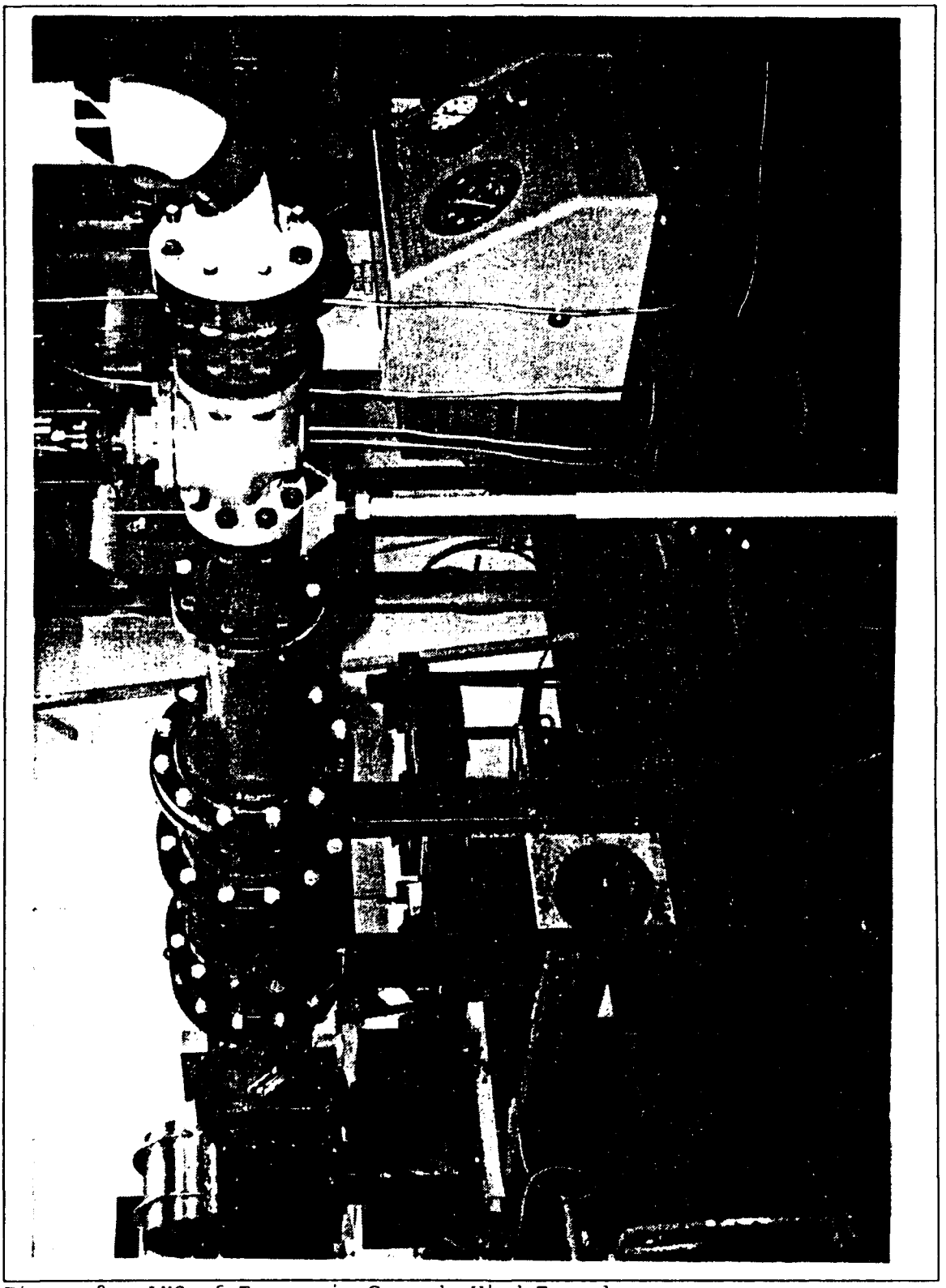

Figure 8. LHS of Transonic Cascade Wind Tunnel

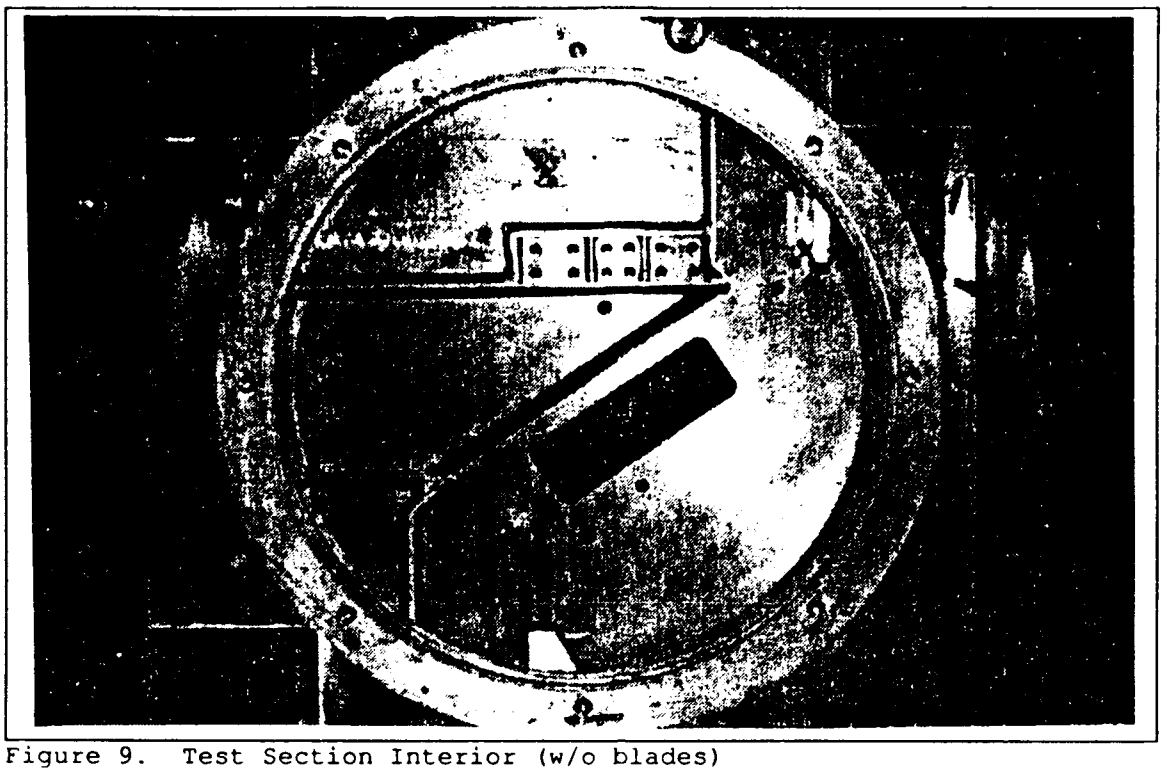

Figure 9. Test Section Interior (w/o blades)

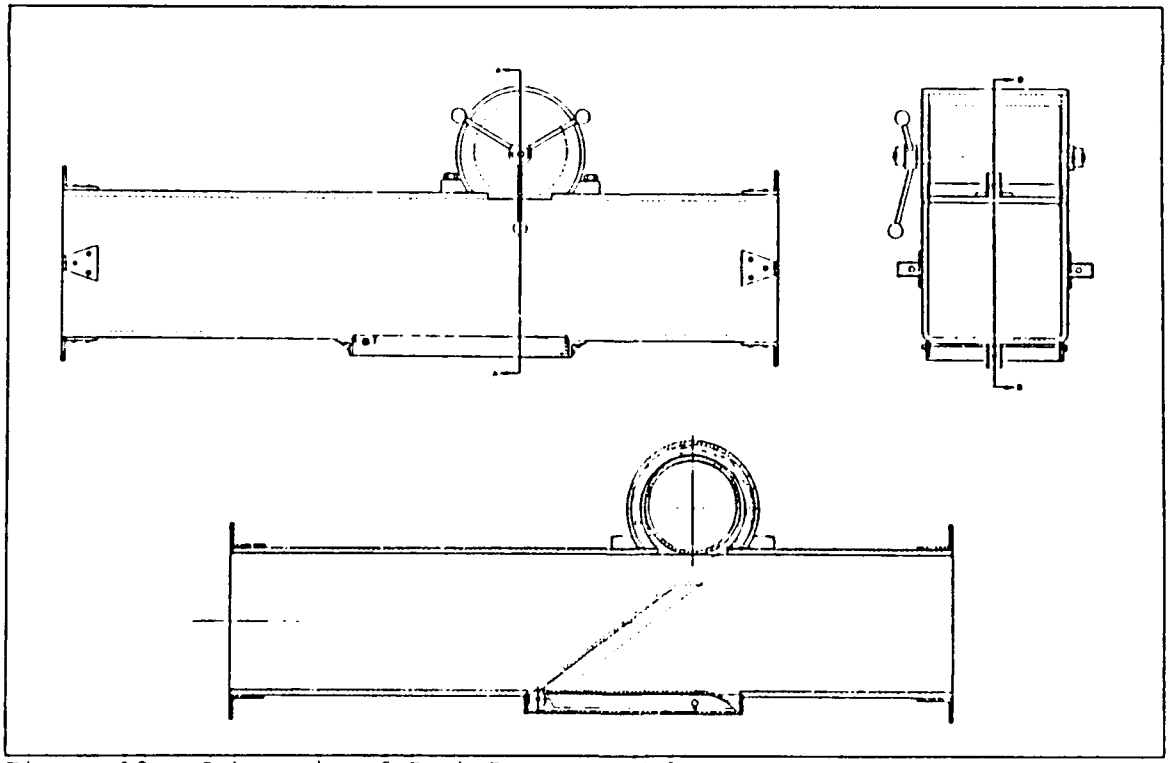

Figure 10. Schematic of Back Pressure Valve

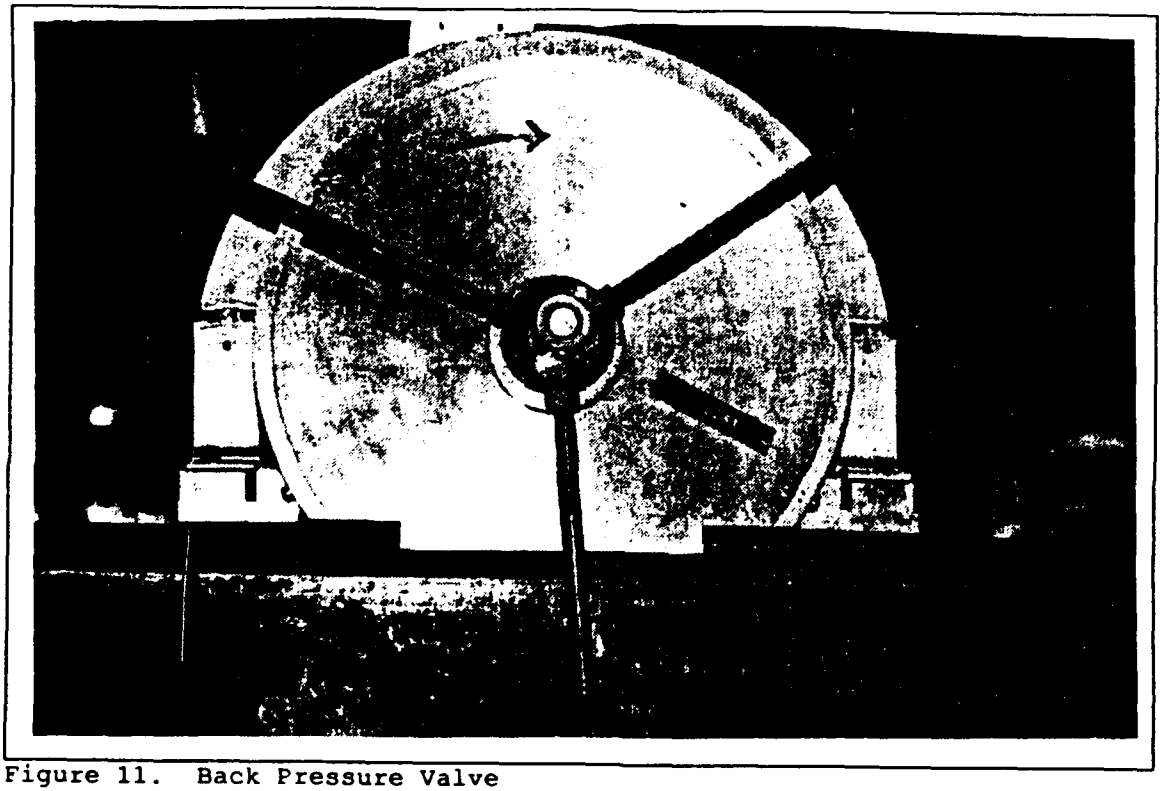

Figure 11. Back Pressure Valve

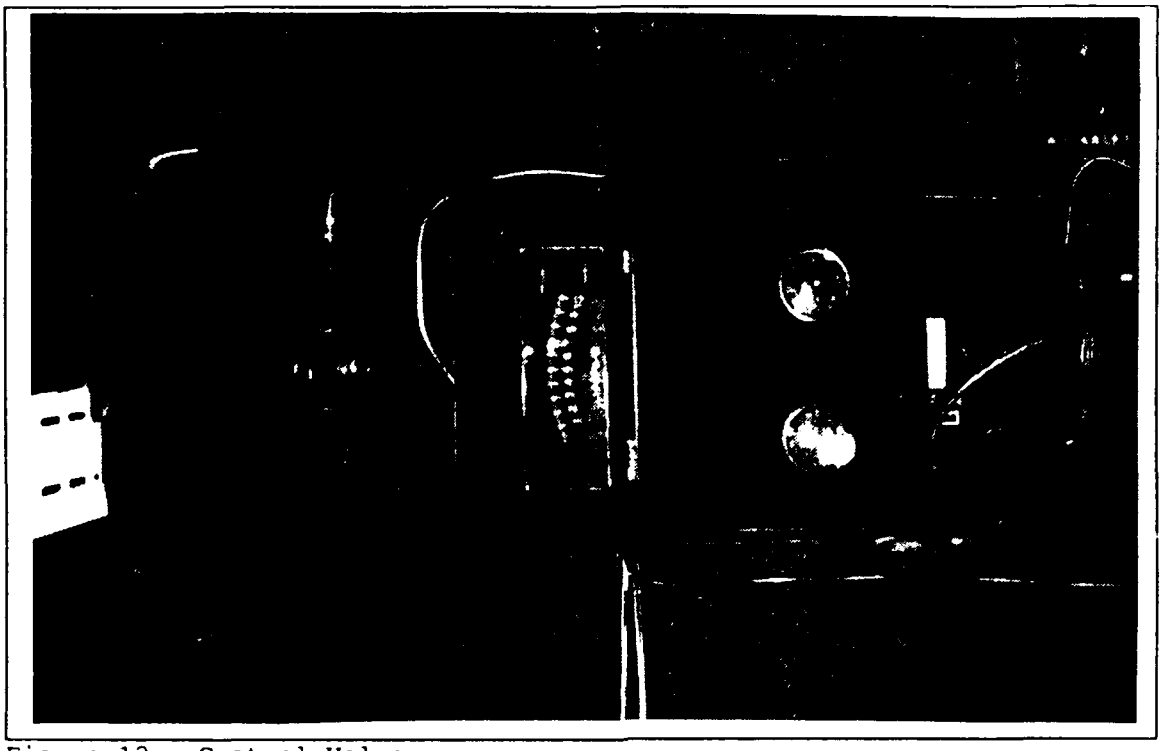

Figure 12. Control Valve

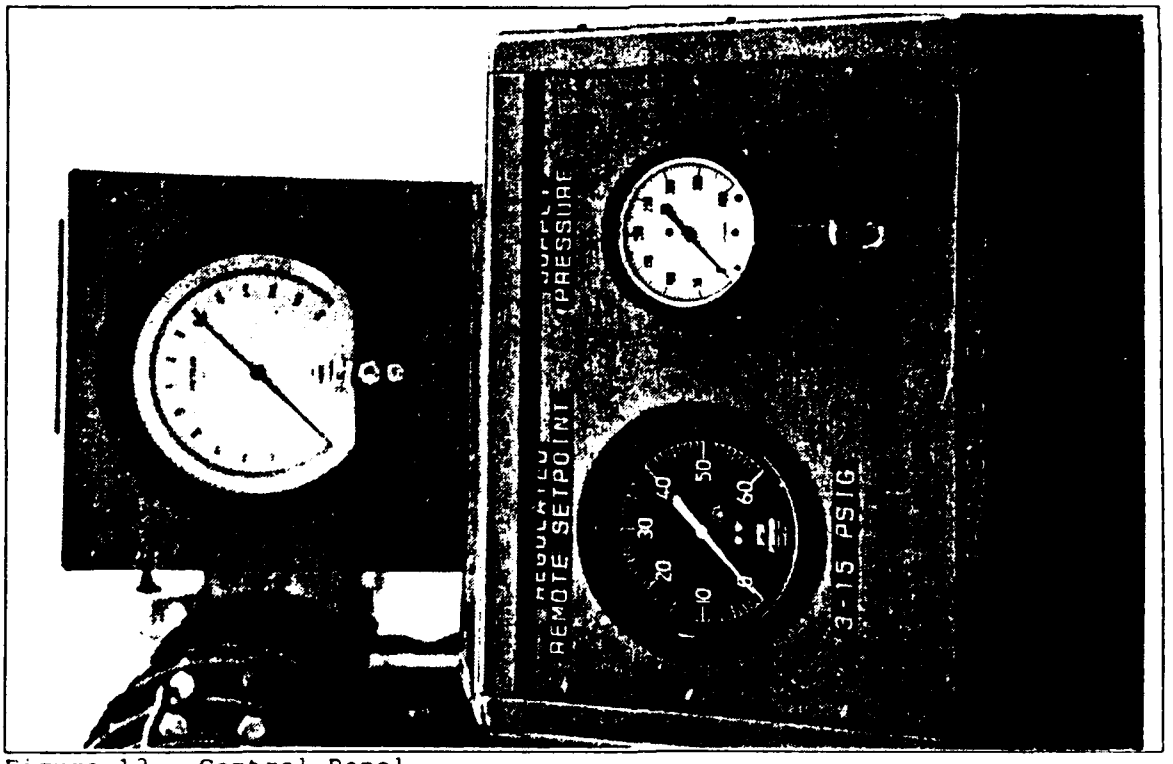

Figure 13. Control Panel

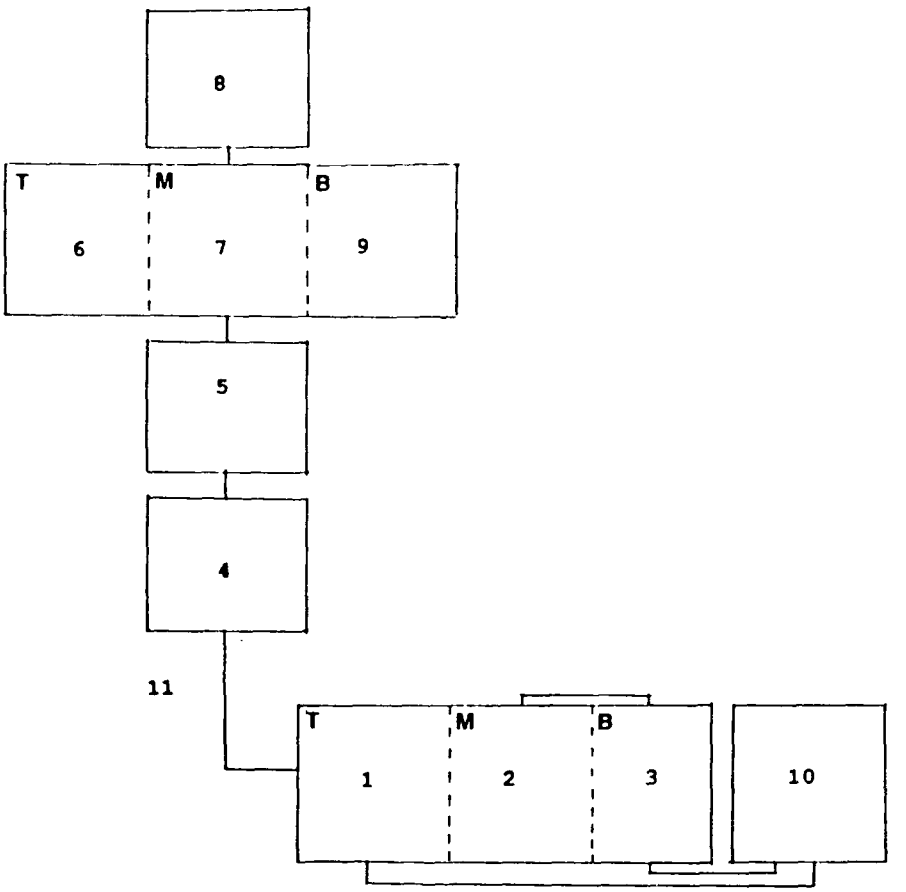

1. HG-78K Scanivalve Controller
2. HP 3455A Digital Voltmeter
3. HP 3495A Scanner
4. HP 9862A Calculator Plotter
5. HP 9830A Computer
6. HP 9868 I/O Expander
7. HP 11305A Controller
8. HP 9867B Mass Memory
9. HP 13215 Disc Power Supply
10. Pressure Transducer (48 Port Scanivalve)
11. HP-IB Interface Bus

Figure 14. Schematic of the Data Acquisition System

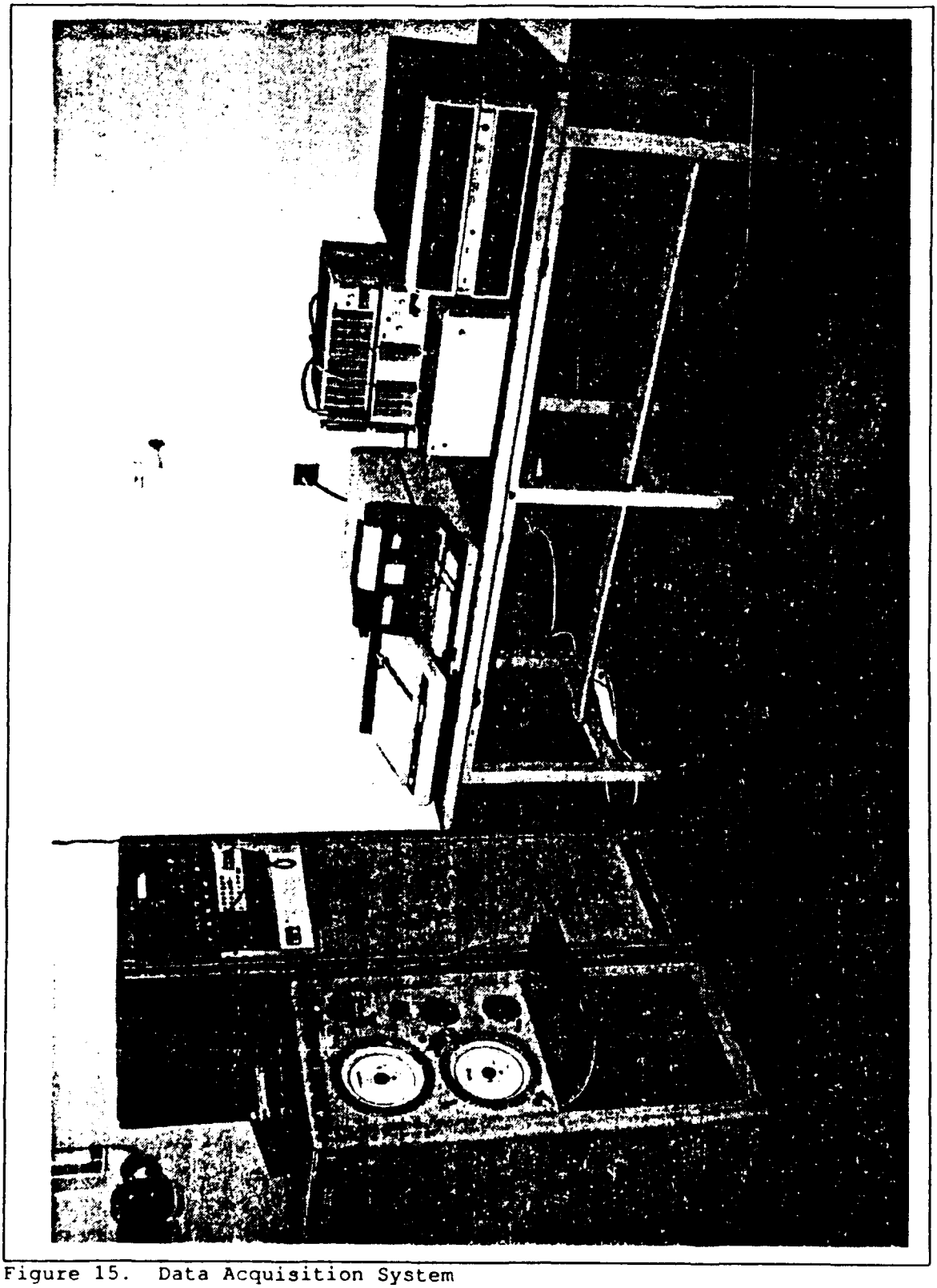

Figure 15. Data Acquisition System

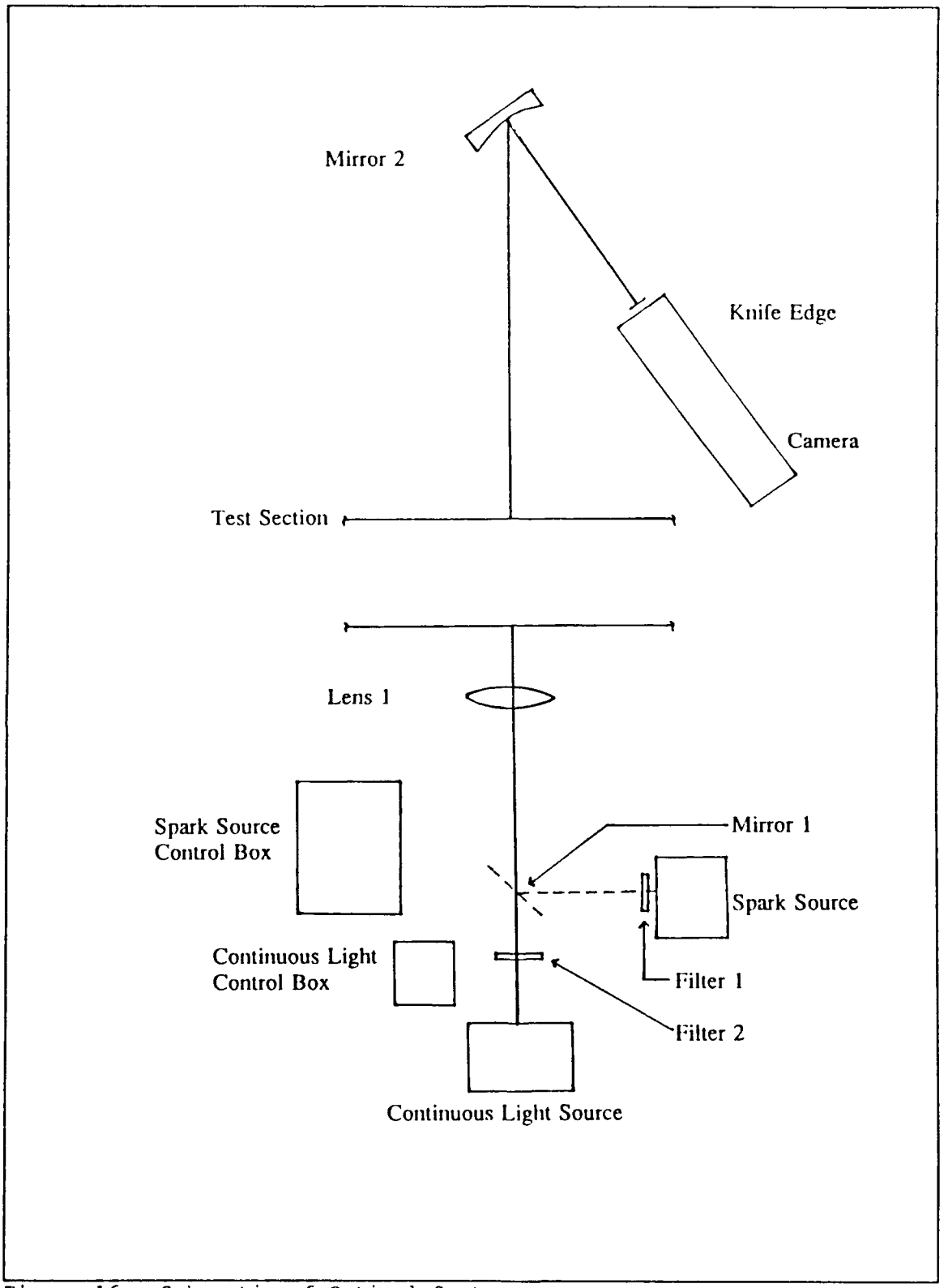

Figure 16. Schematic of Optical System

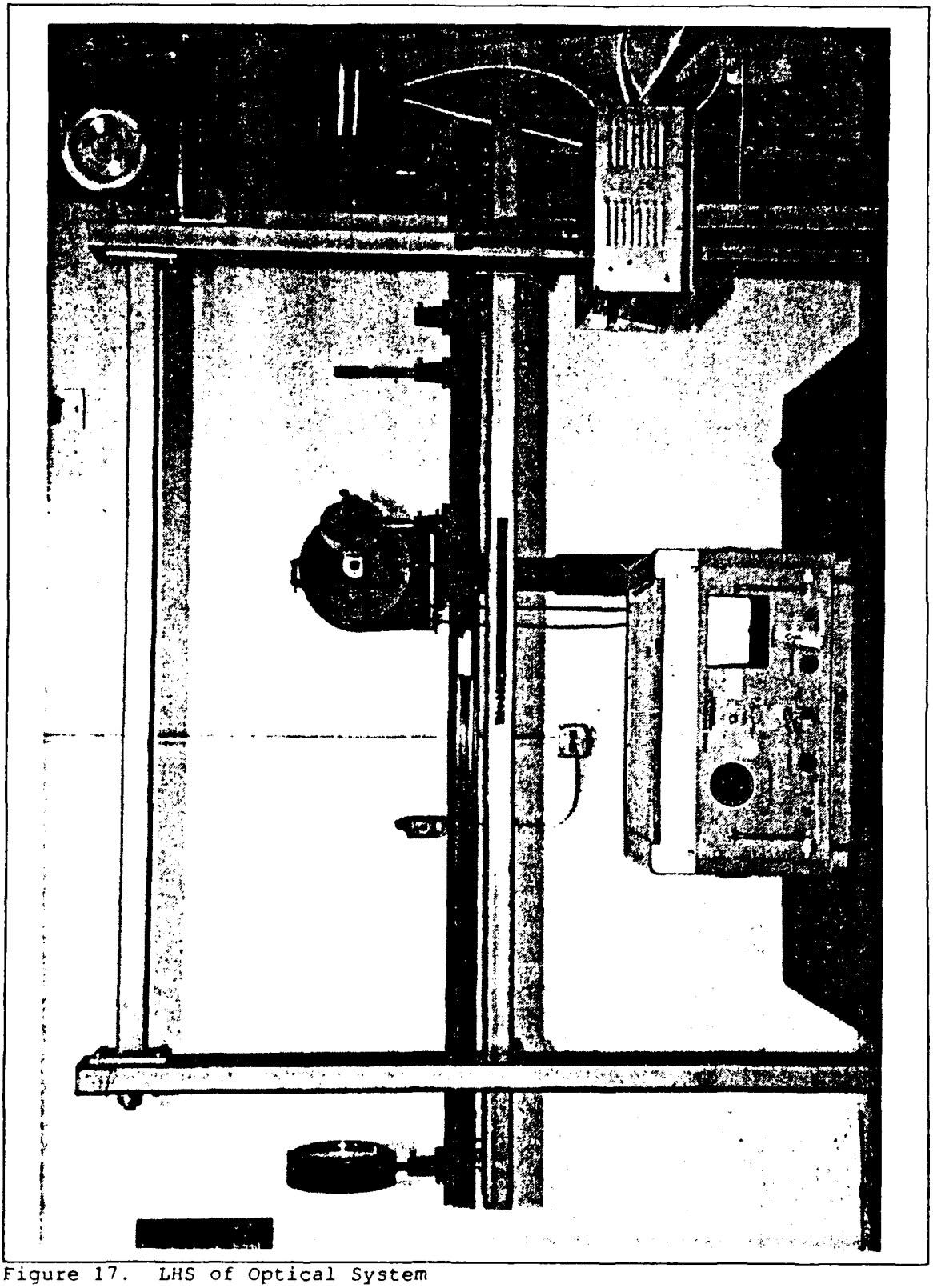

Figure 17. LHS of Optical System

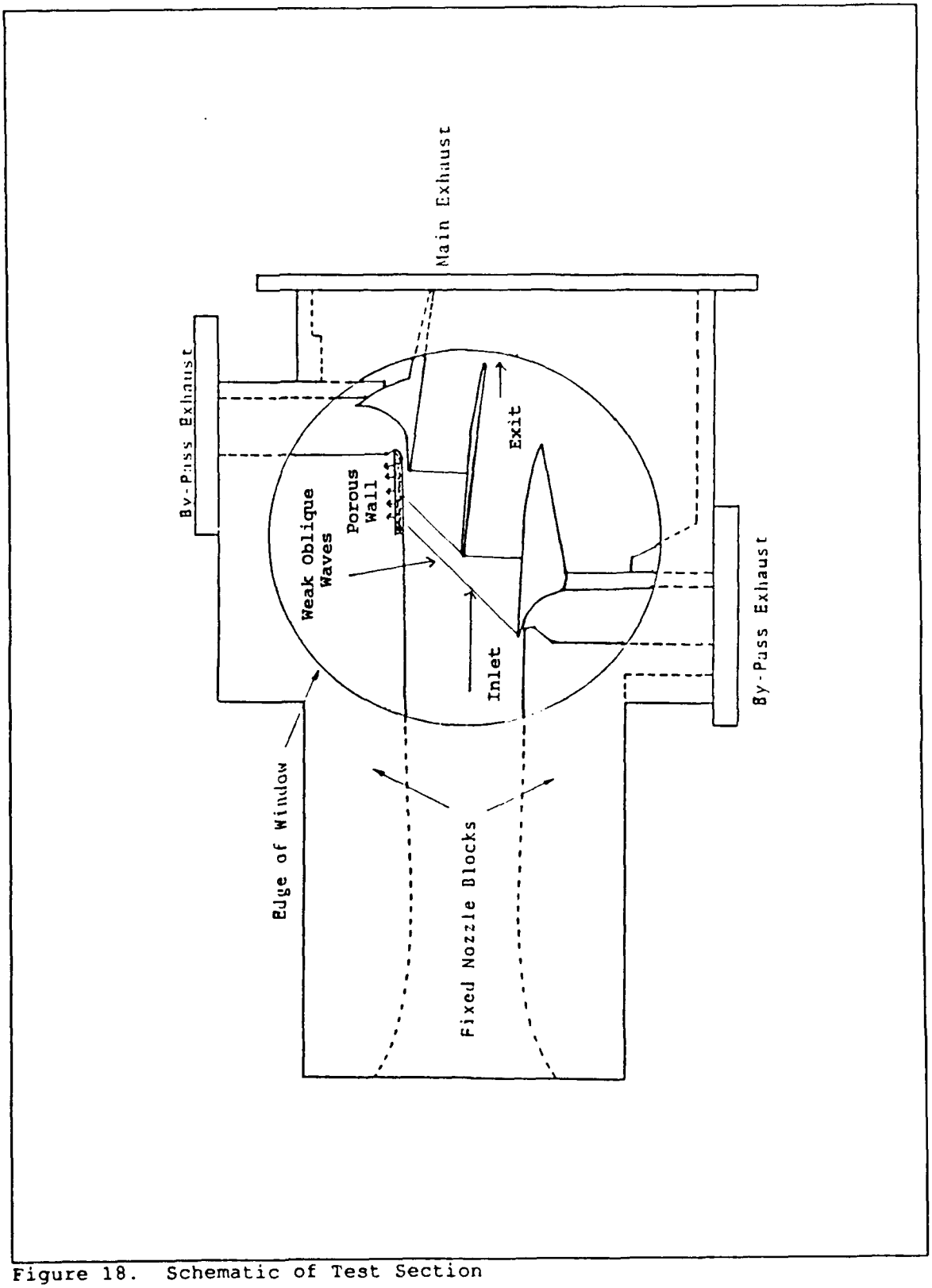

Figure 18. Schematic of Test Section

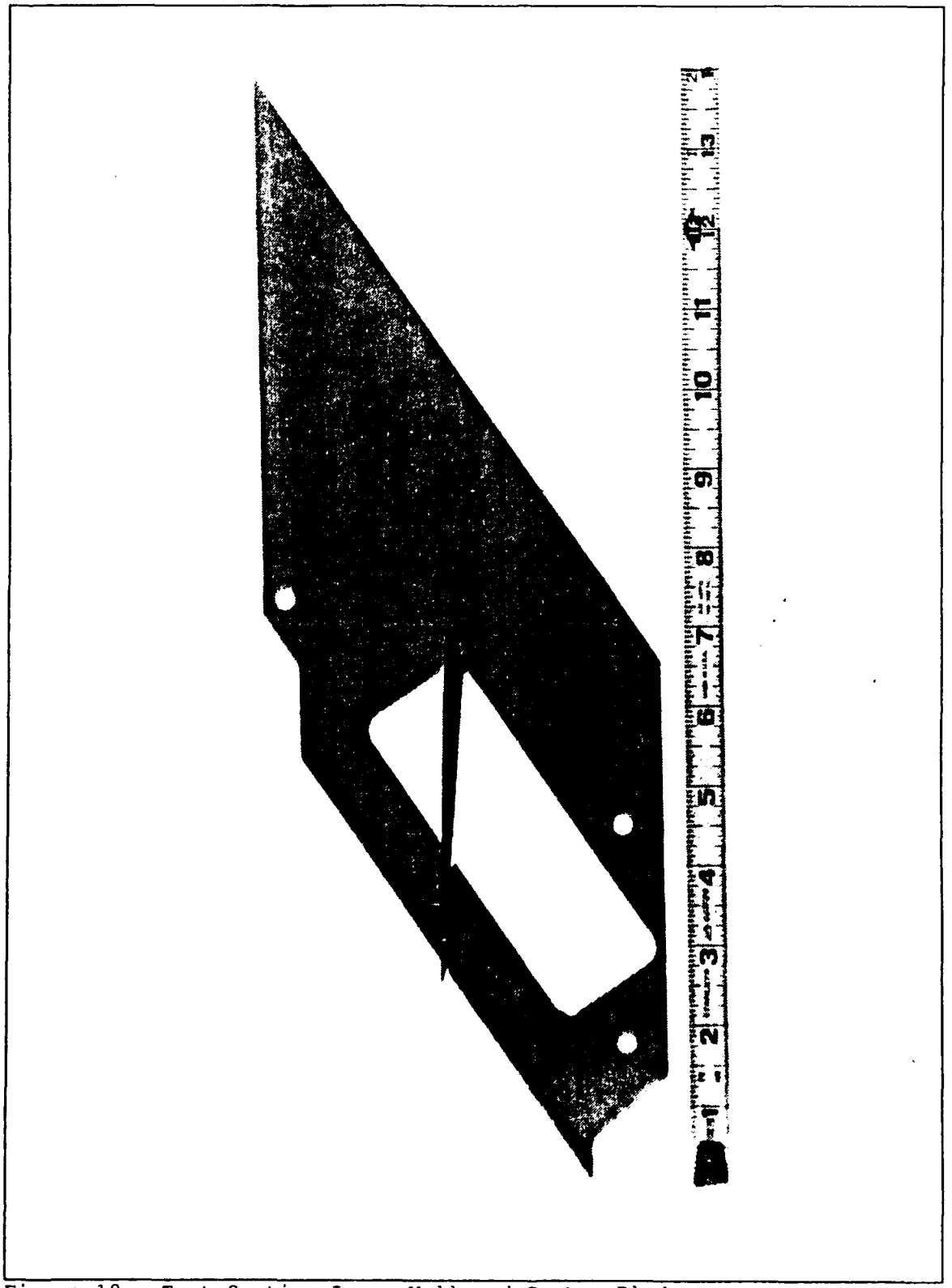

Figure 19. Test Section Inner Wall and Center Blade

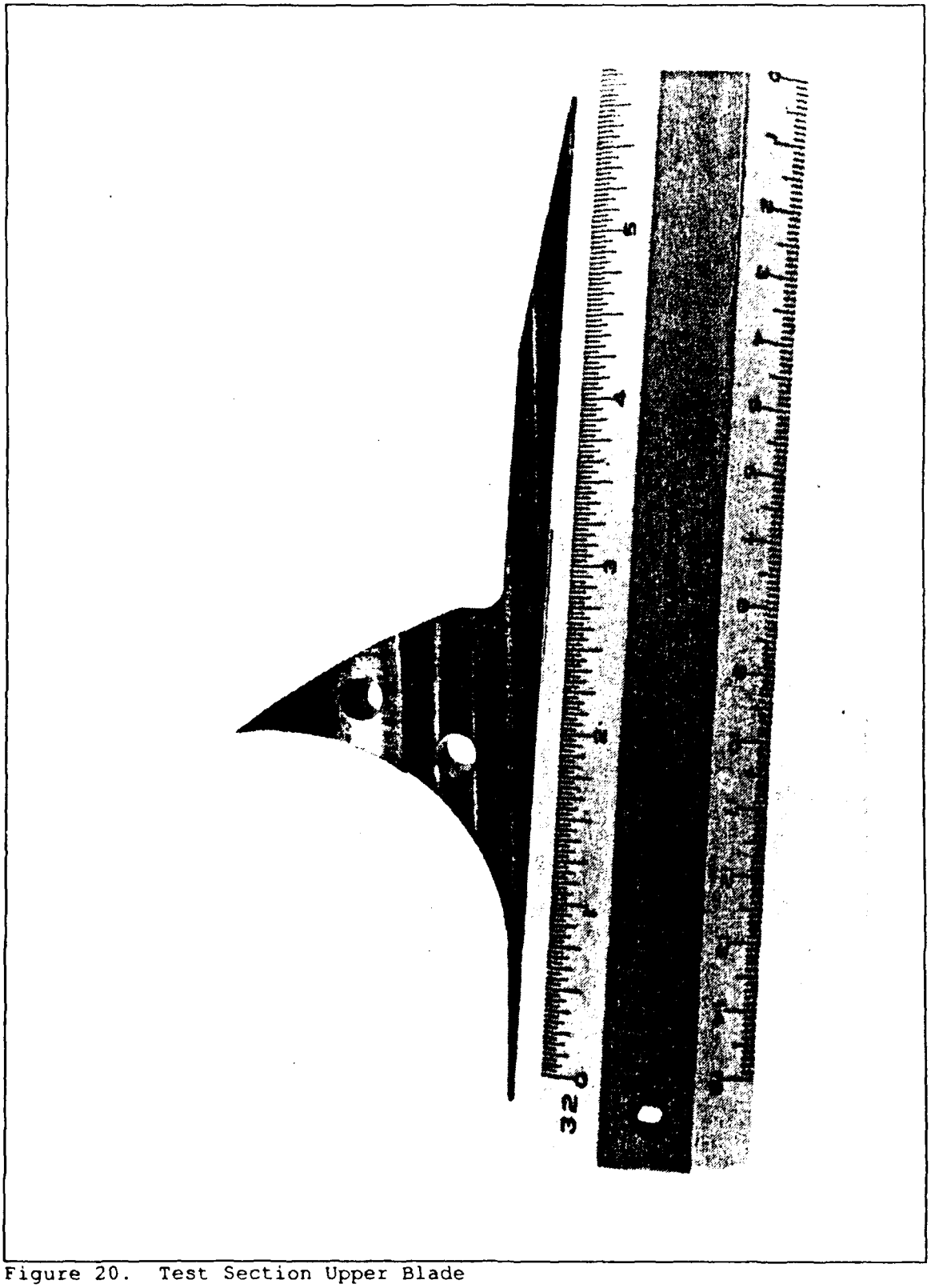

Figure 20. Test Section Upper Blade

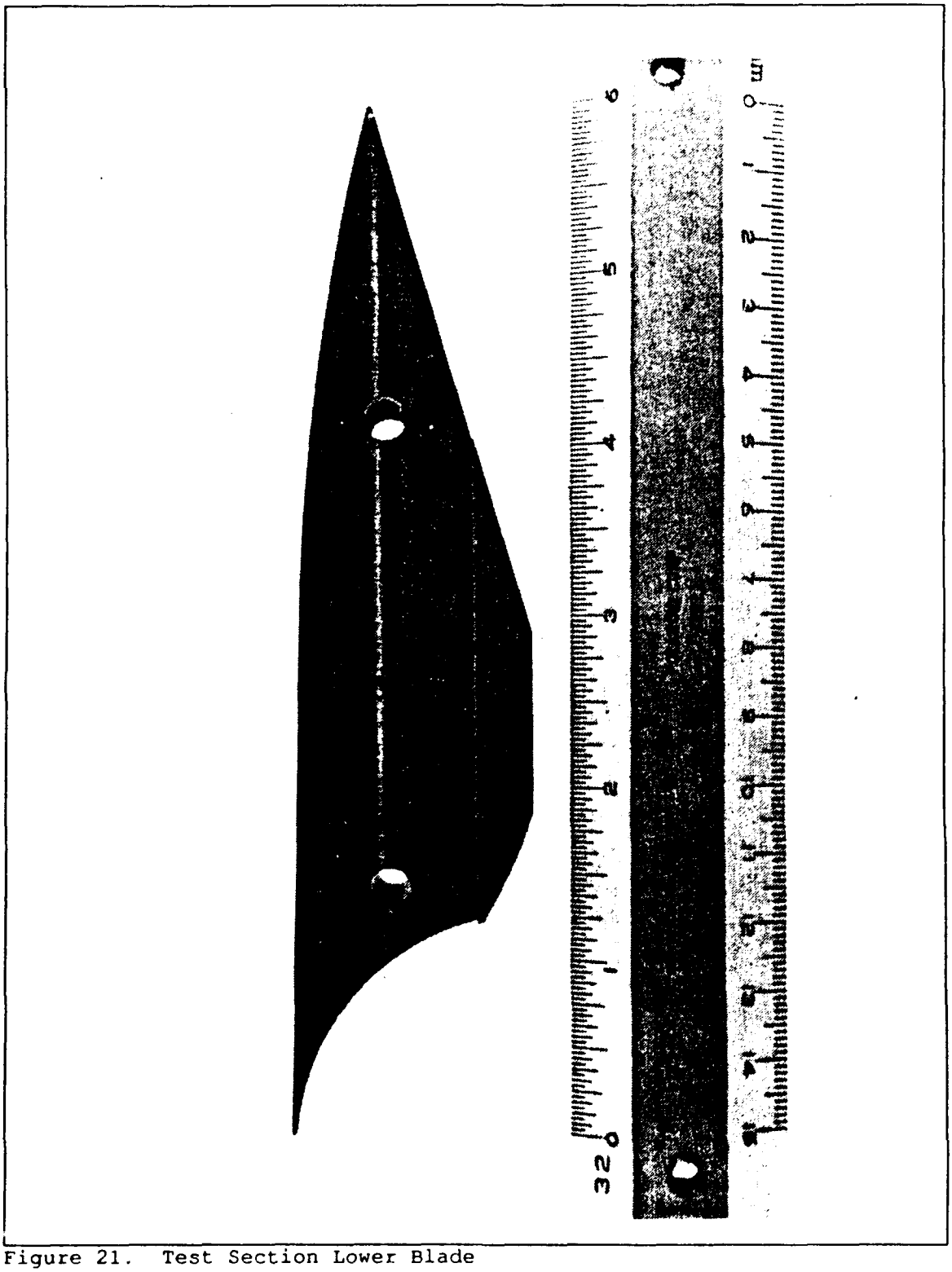

Figure 21. Test Section Lower Blade

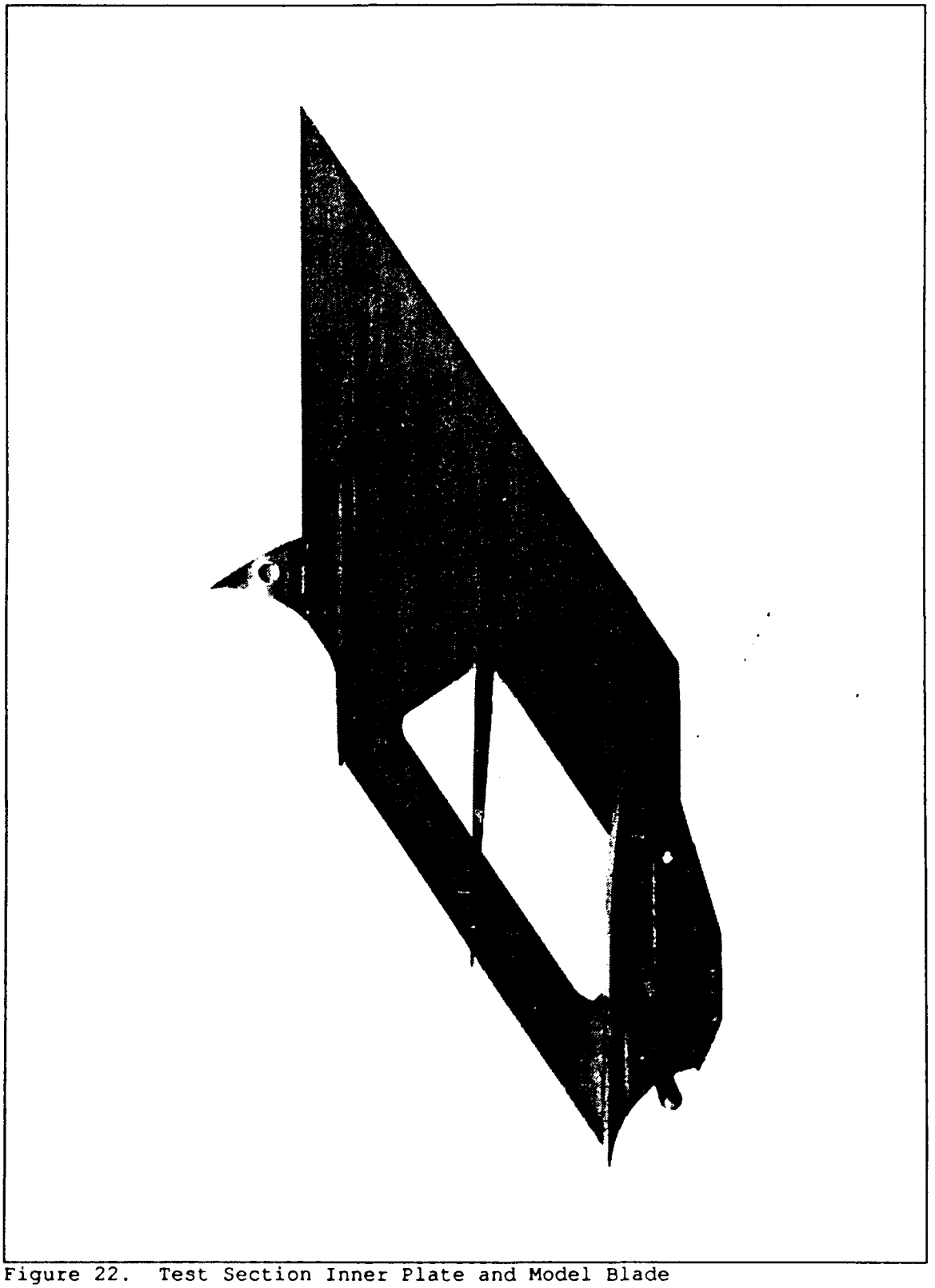

Figure 22. Test Section Inner Plate and Model Blade

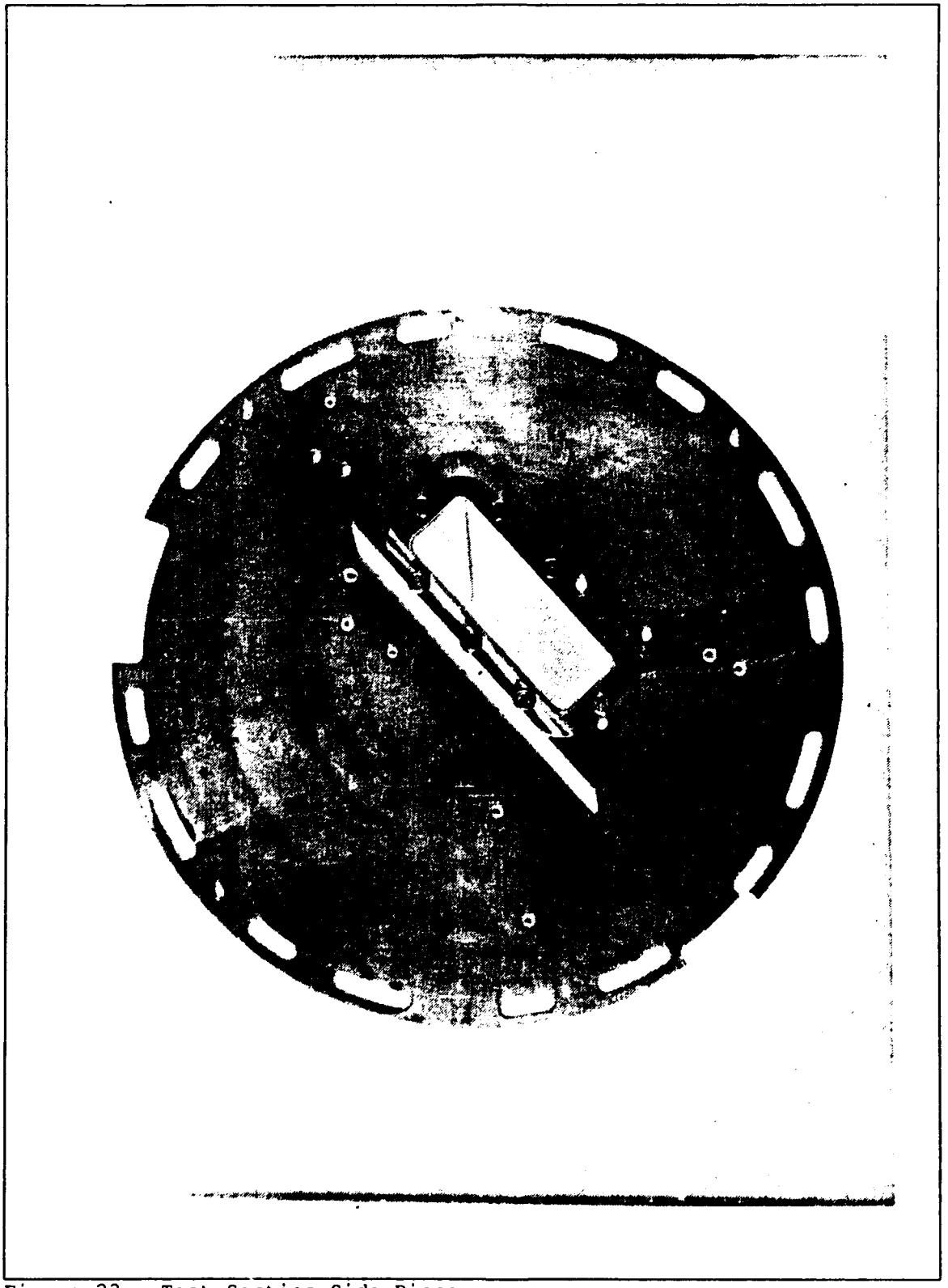

Figure 23. Test Section Side Piece

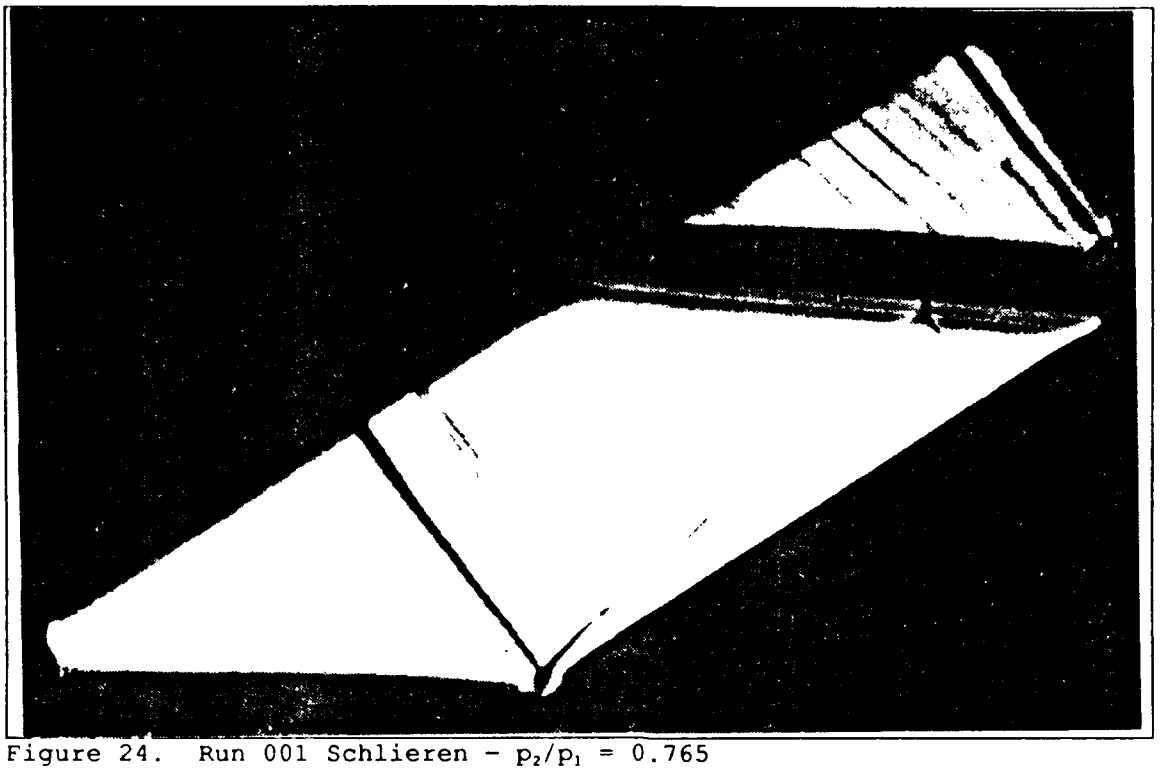

Figure 24. Run 001 Schlieren - p_2/p_1 = 0.765

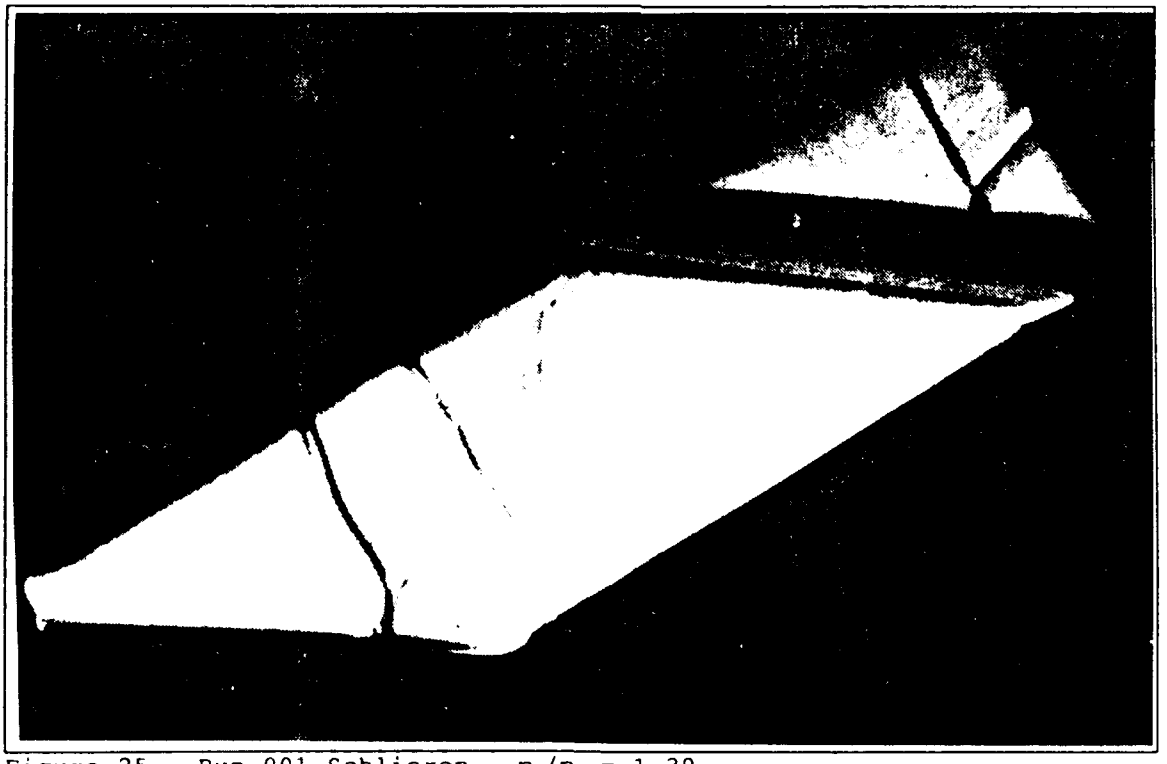

Figure 25. Run 001 Schlieren - p_2/p_1 = 1.39

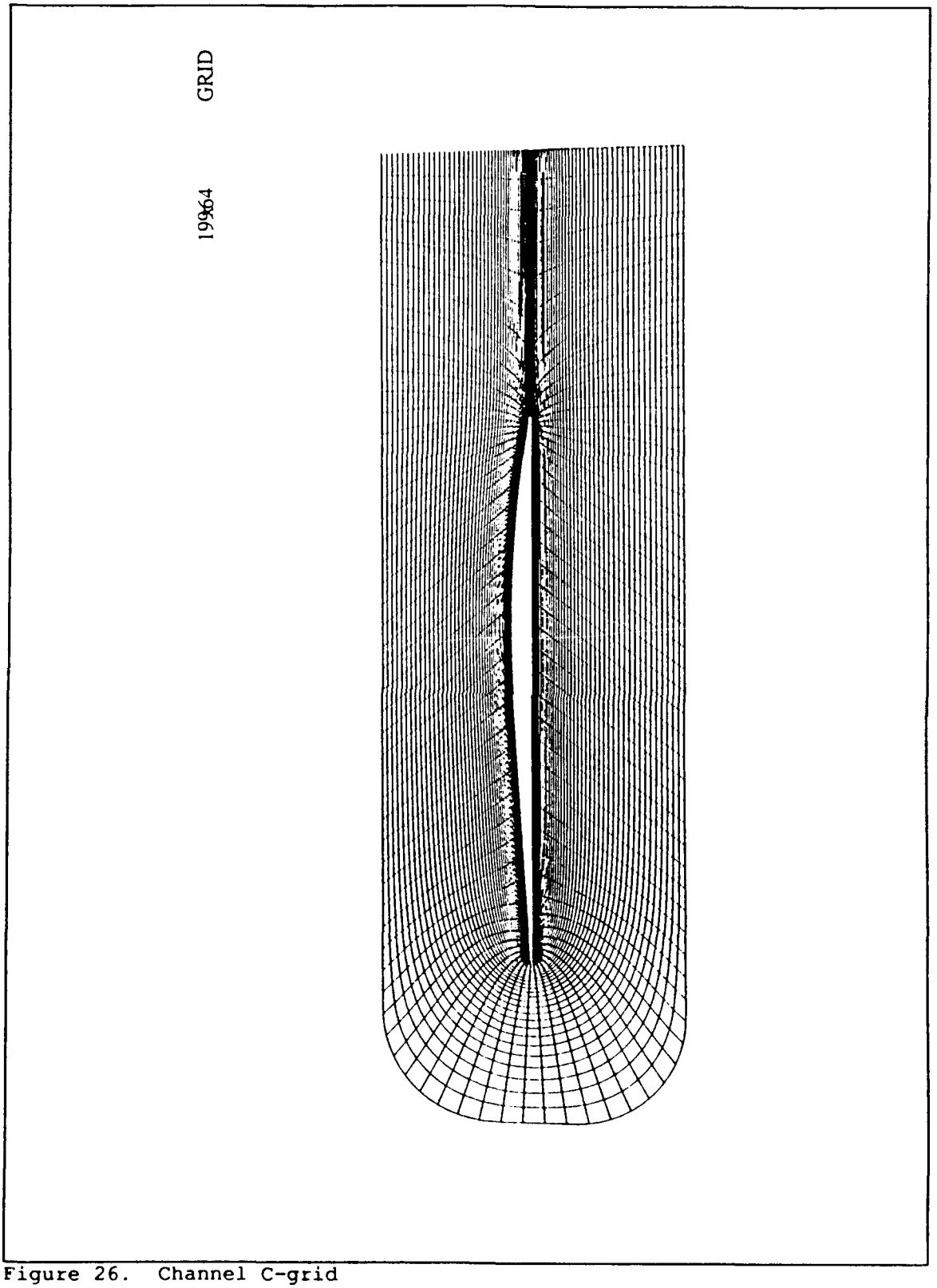

Figure 26. Channel C-grid

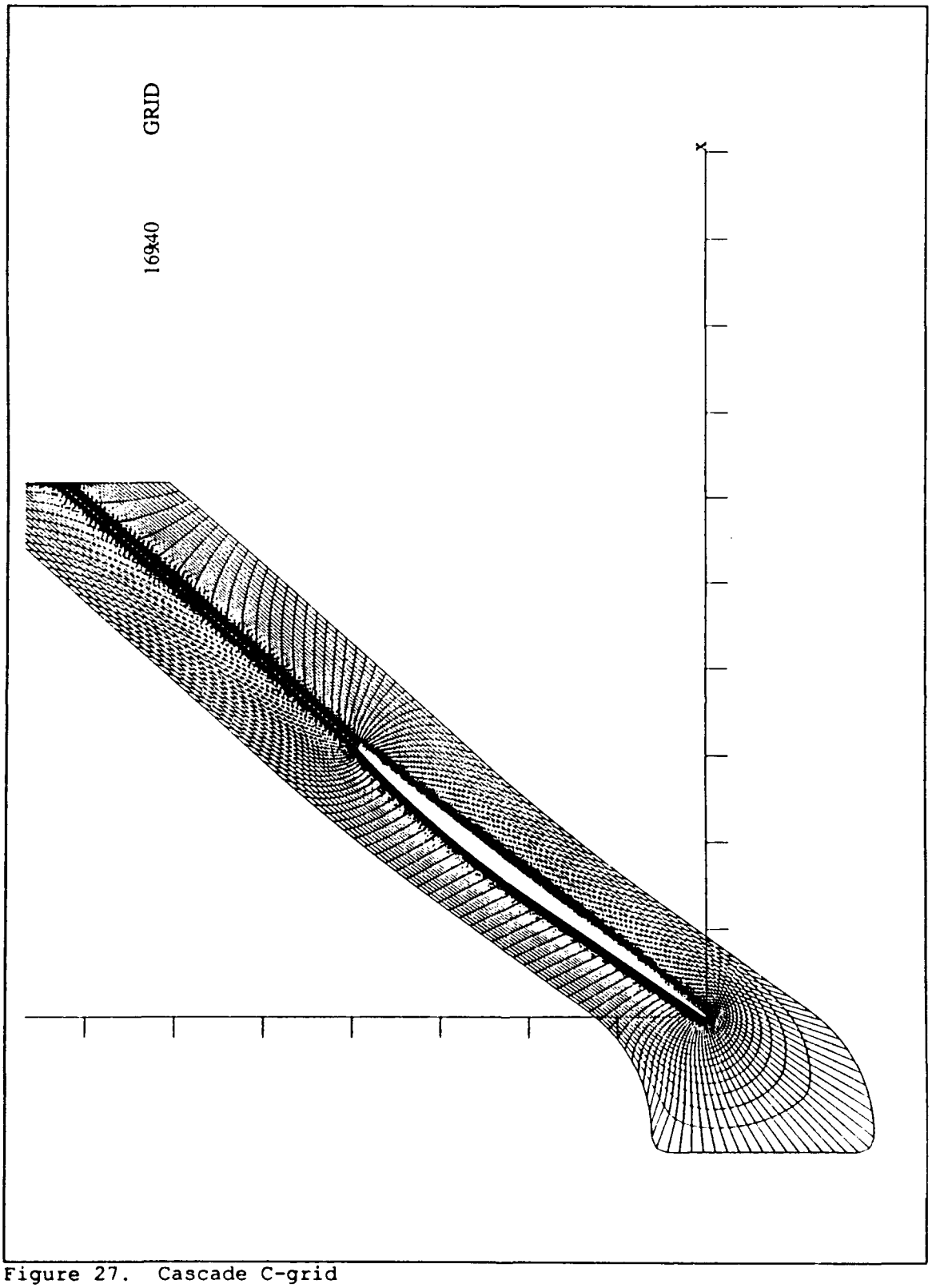

Figure 27. Cascade C-grid

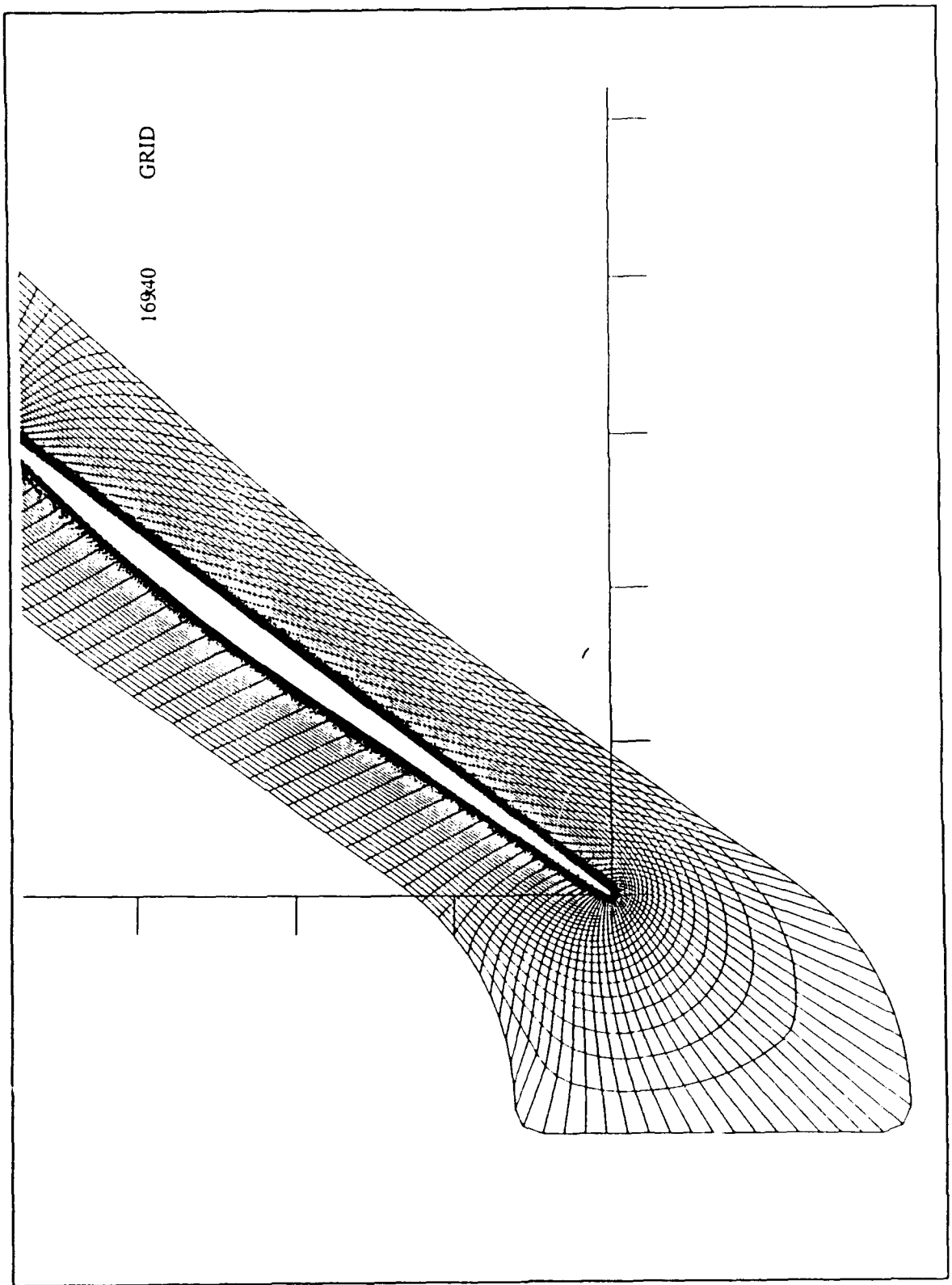

Figure 28. Detailed View of Cascade C-grid

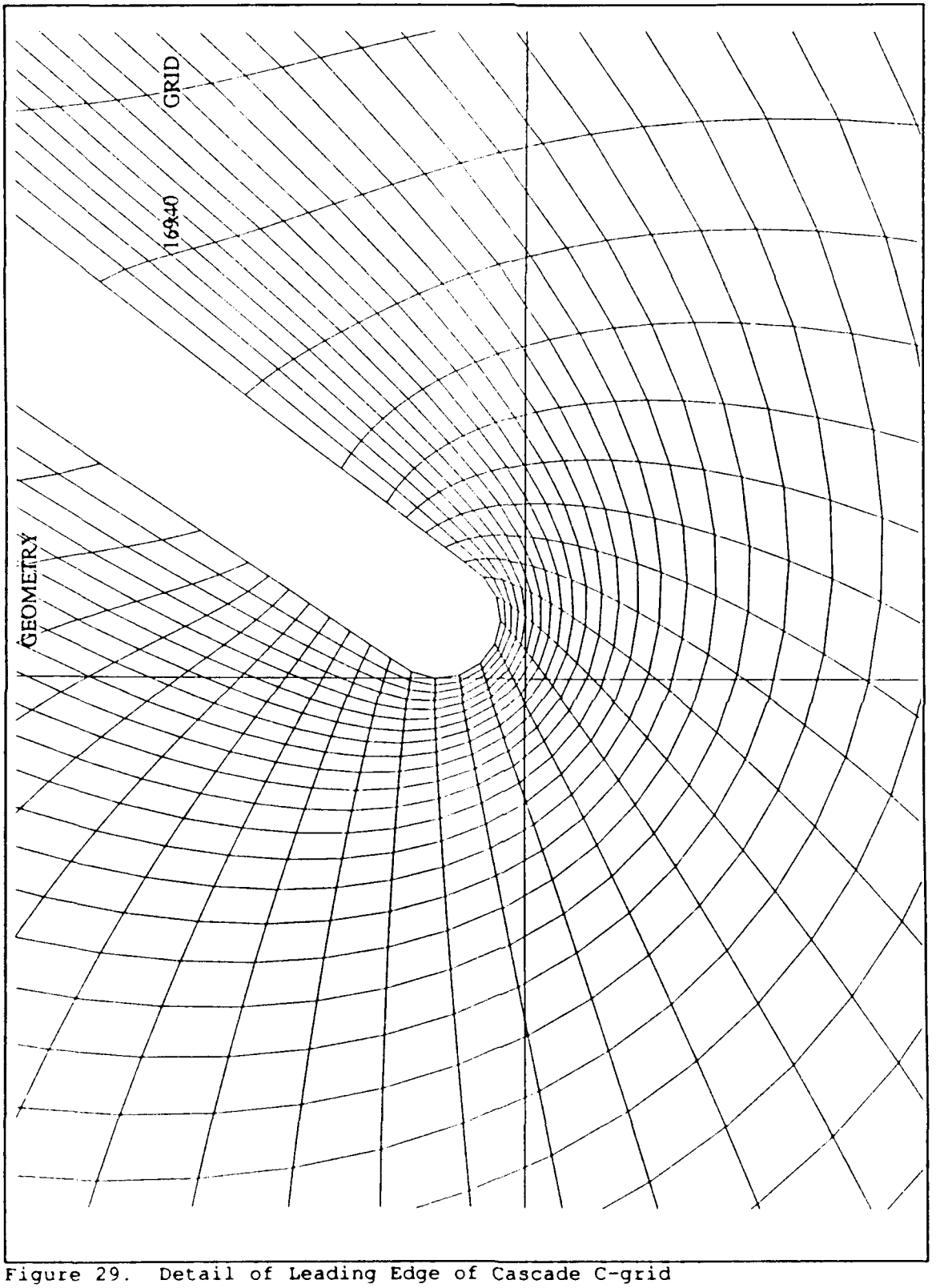

Figure 29. Detail of Leading Edge of Cascade C-grid

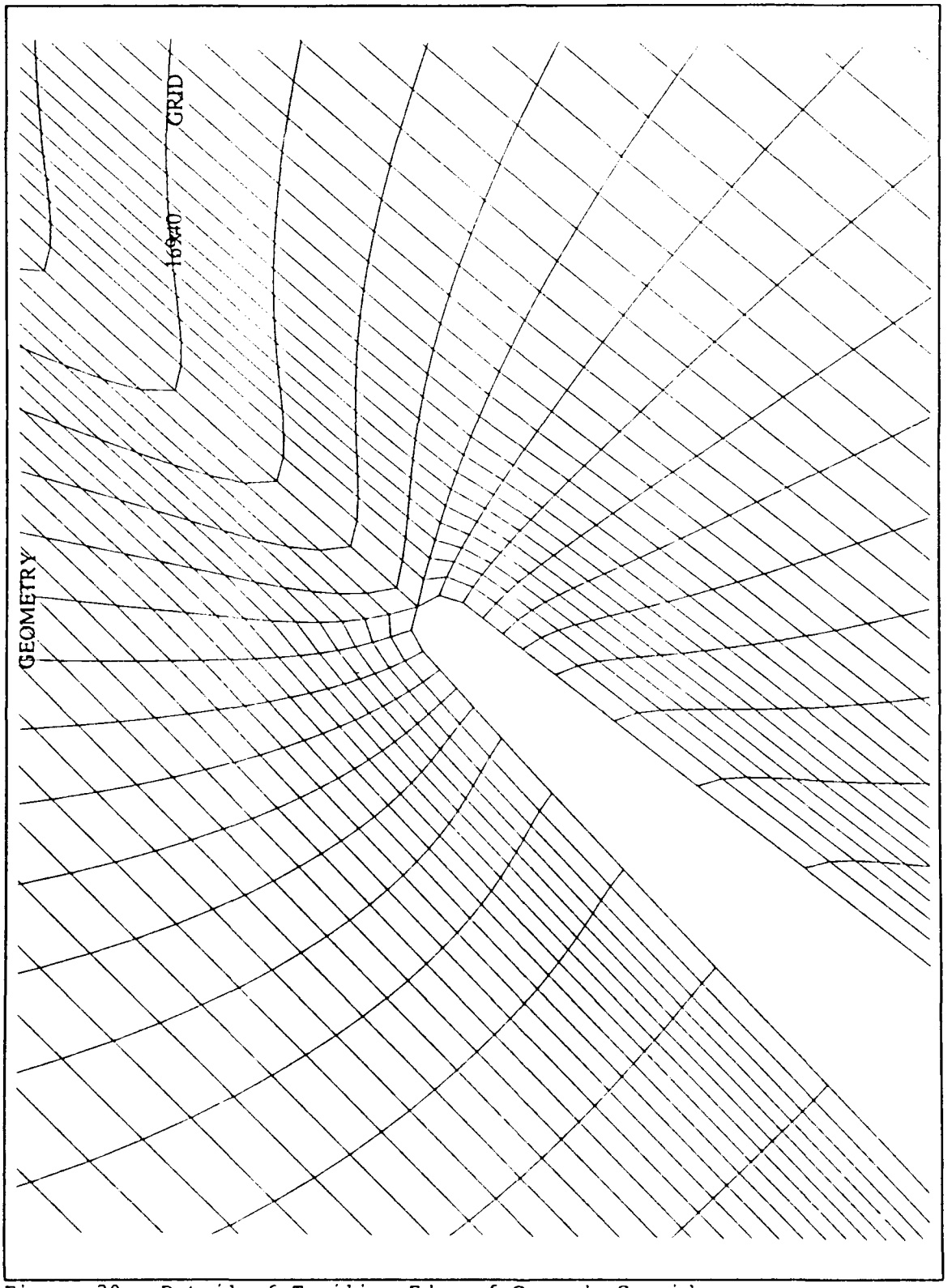

Figure 30. Detail of Trailing Edge of Cascade C-grid

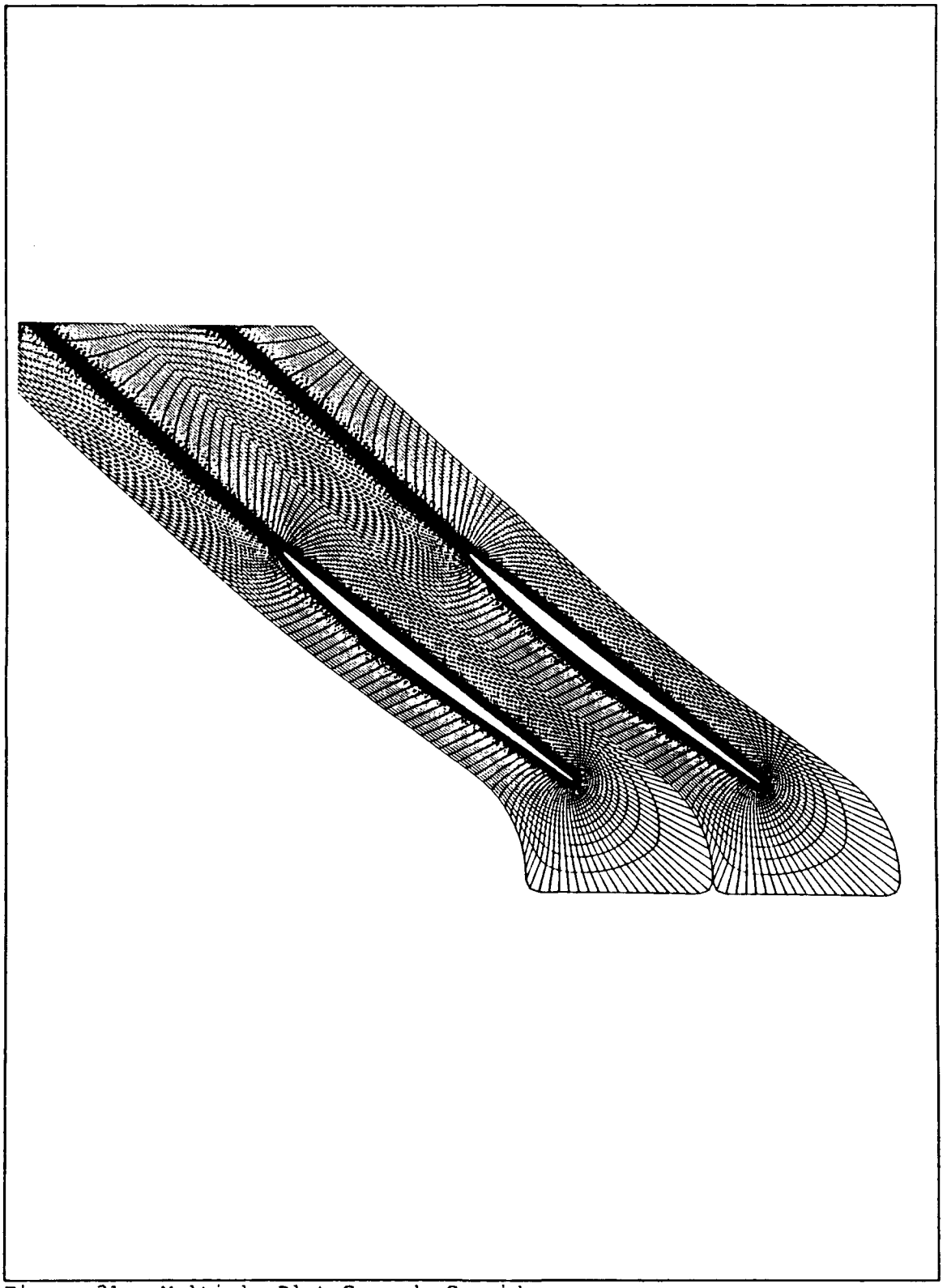

Figure 31. Multiple Plot Cascade C-grid

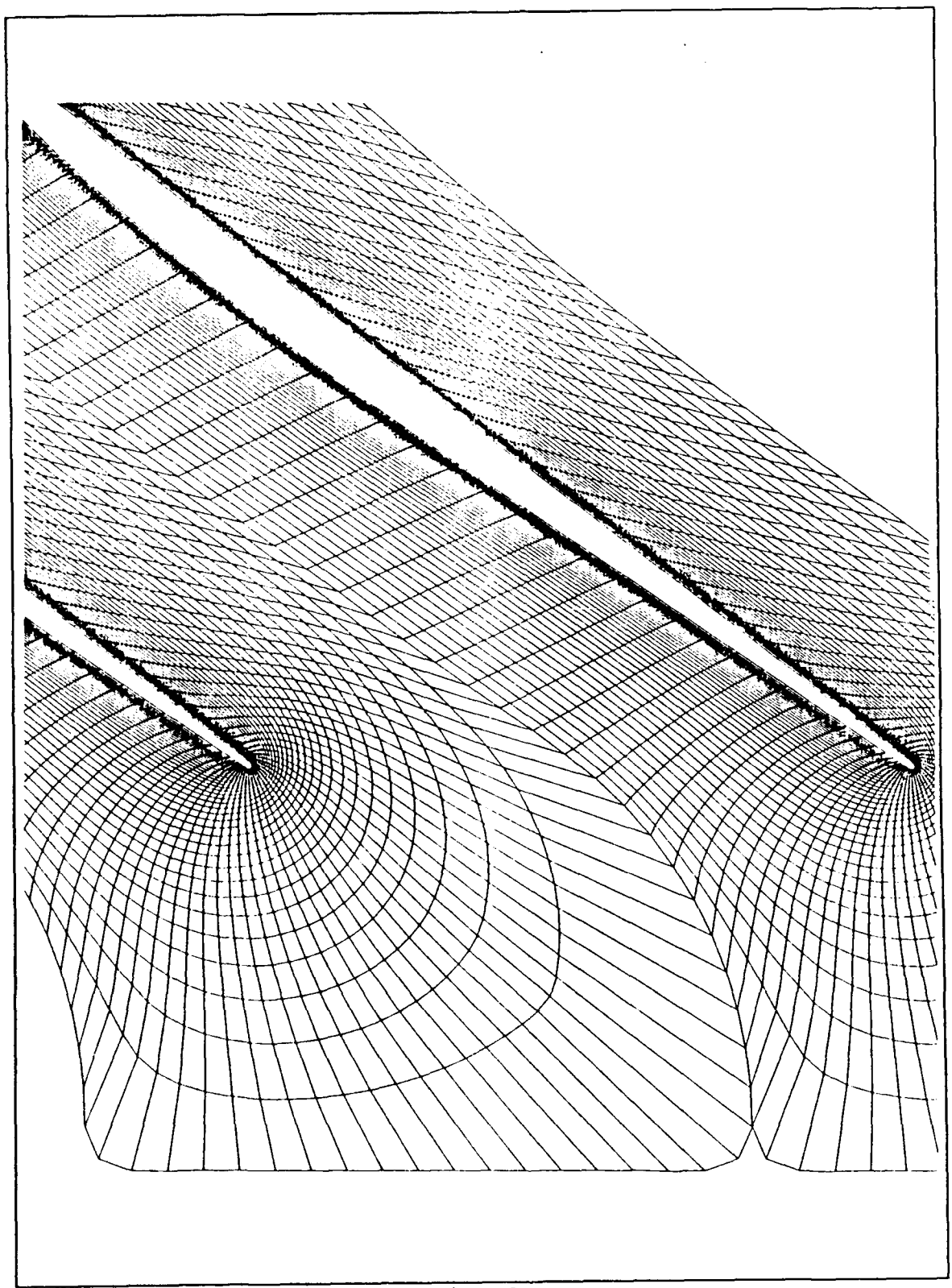

Figure 32. Detailed View of Boundary Area

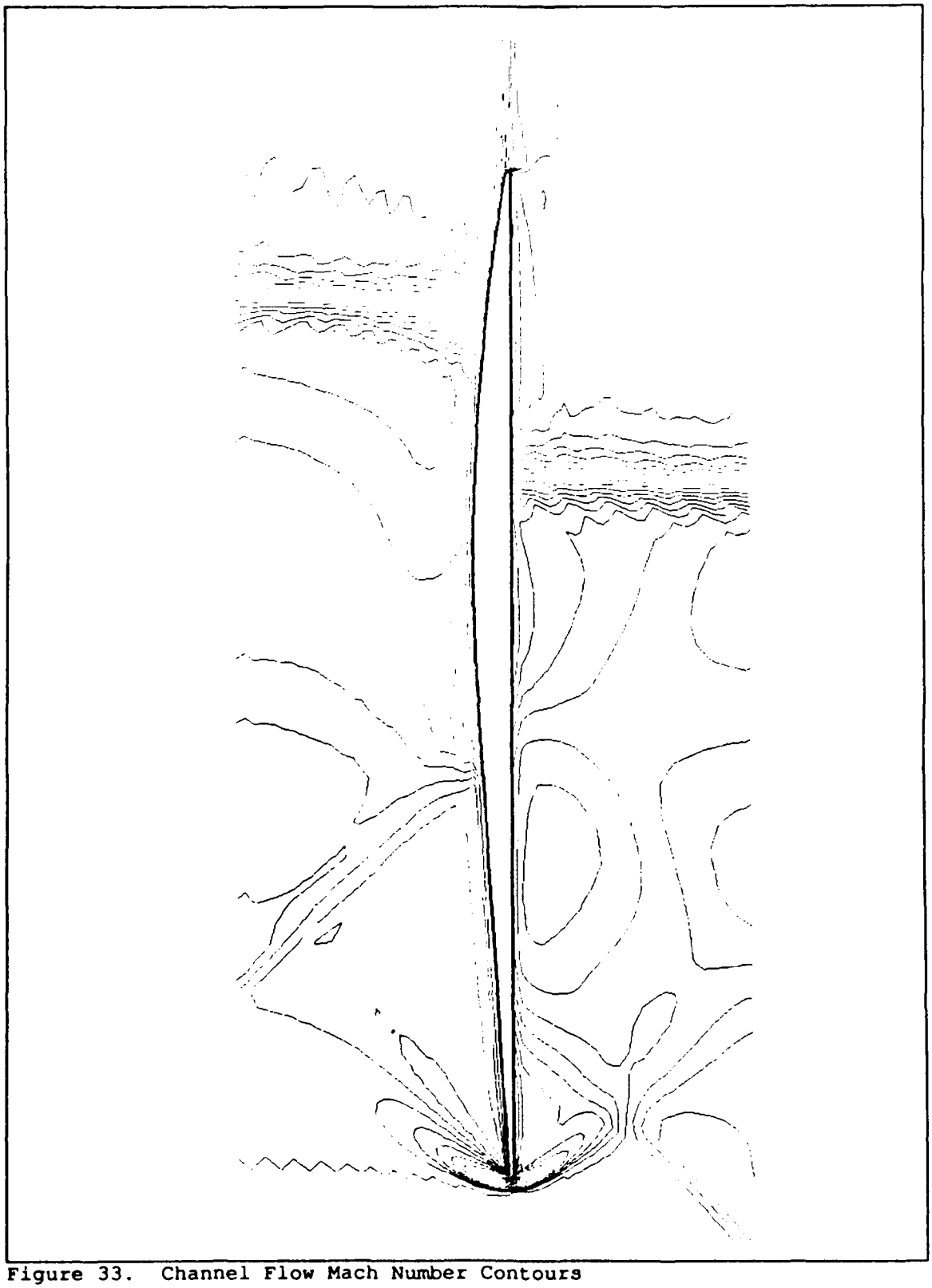

Figure 33. Channel Flow Mach Number Contours

Figure 34. Cascade Flow Mach Number Contours

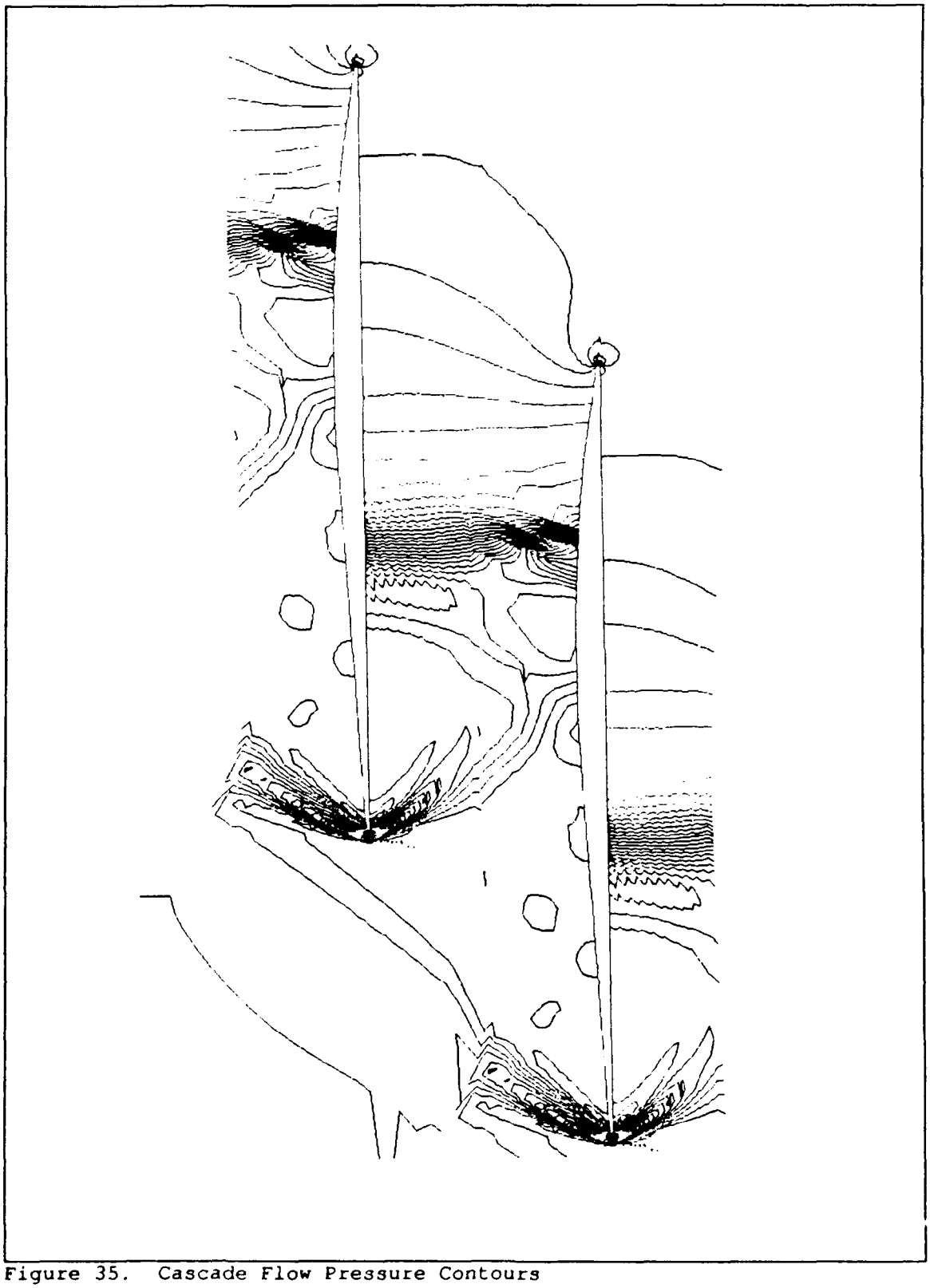

Figure 35. Cascade Flow Pressure Contours

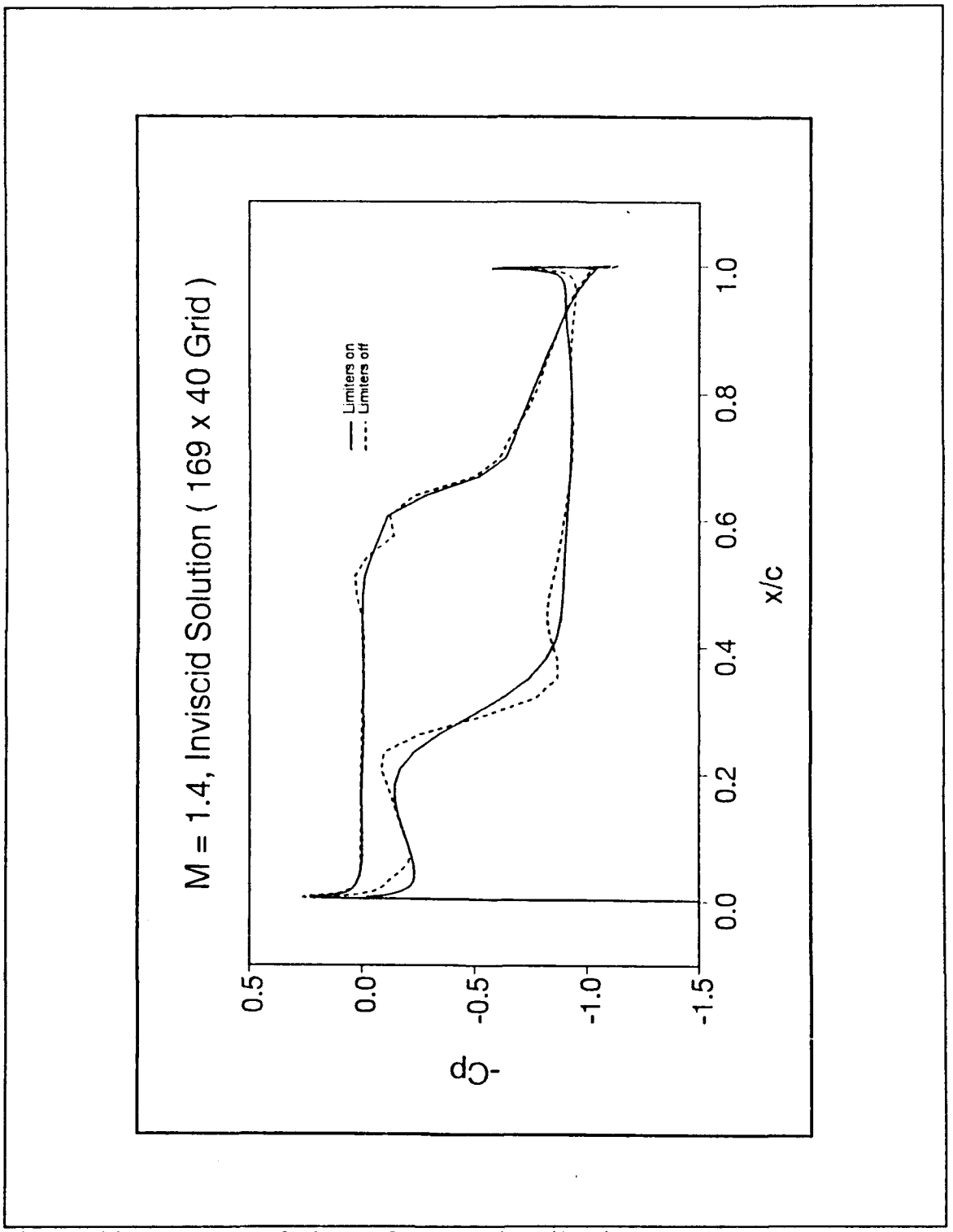

Figure 36. Cascade Blade Surface C_p Distribution

APPENDIX A

MACHINE DRAWINGS OF TEST SECTION COMPONENTS

Drawing No.	Title
T001	Test Section Side Piece
T002	Test Section Inner Frame
T003	Test Section Inner Frame and Blades
T004	Detailed View of Side Piece Slot
T005	Side Piece Window Retainer Frame
T006	Side Piece Window
T007	Sectioned View of Window Installation
T008	Detailed View of Window Slot
T009	Test Section Top Blade
T010	Test Section Middle Blade
T011	Test Section Lower Blade
T012	Pressure Tap Locations on Lower Blade

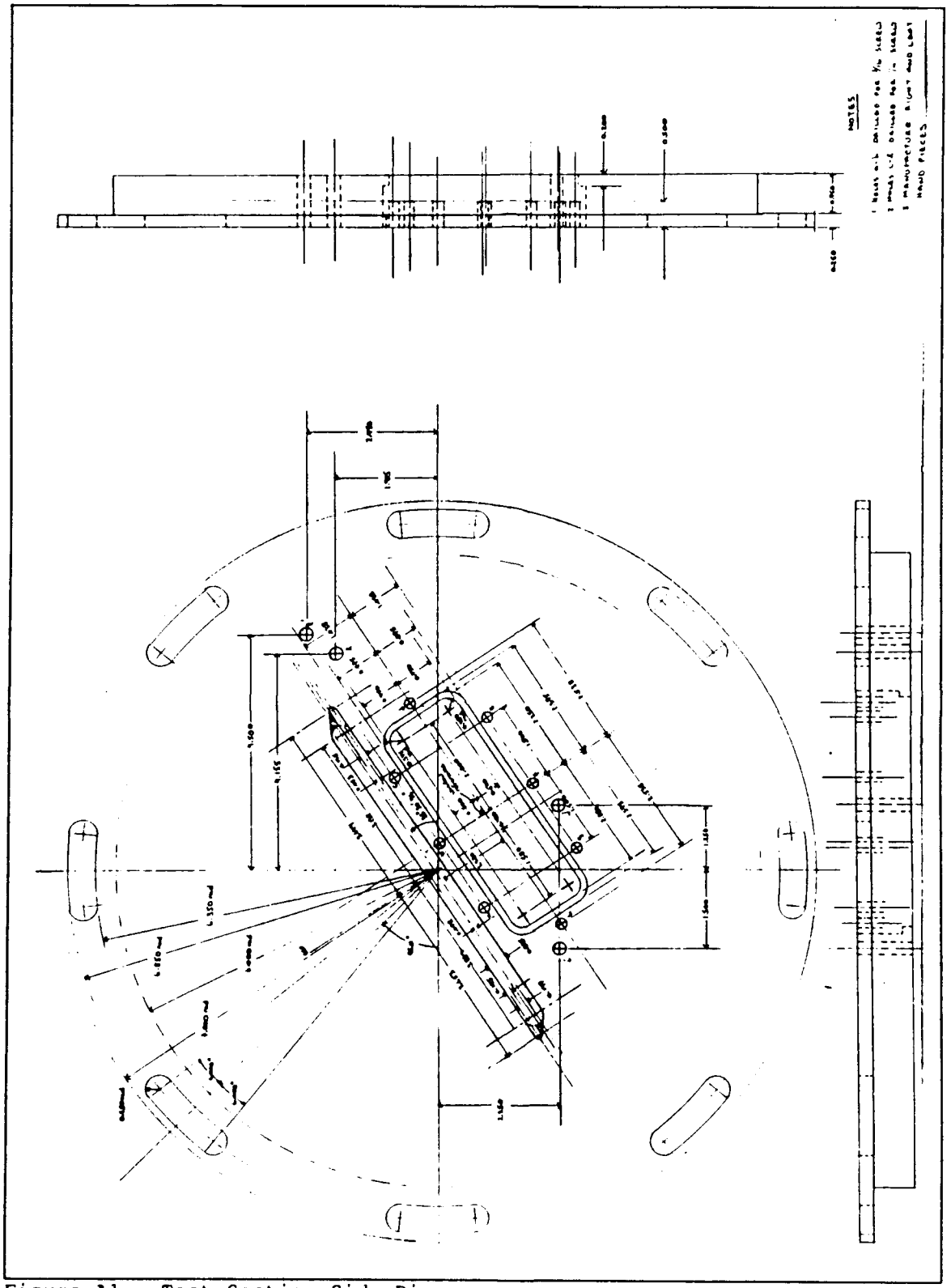

Figure A1. Test Section Side Piece

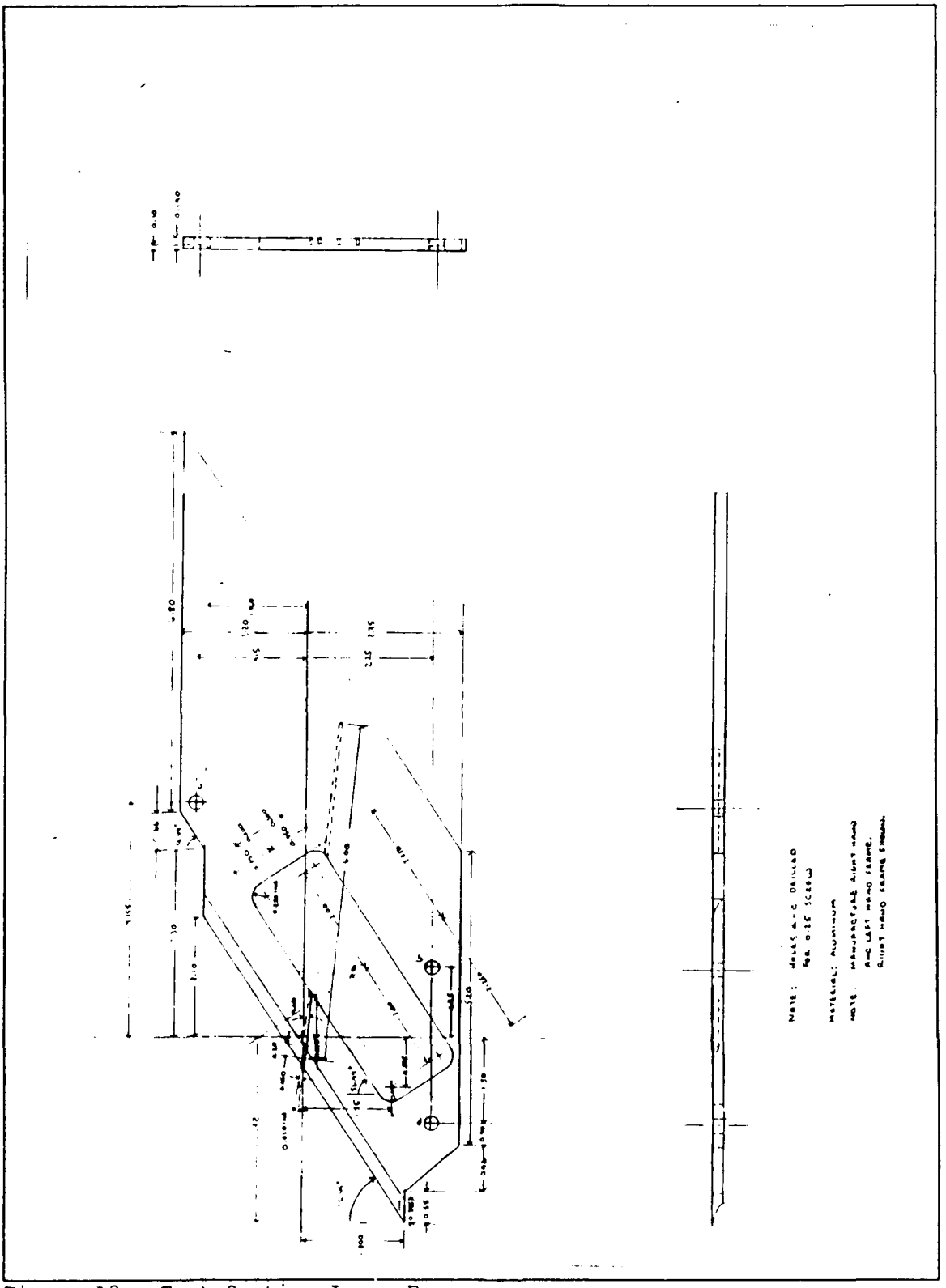

Figure A2. Test Section Inner Frame

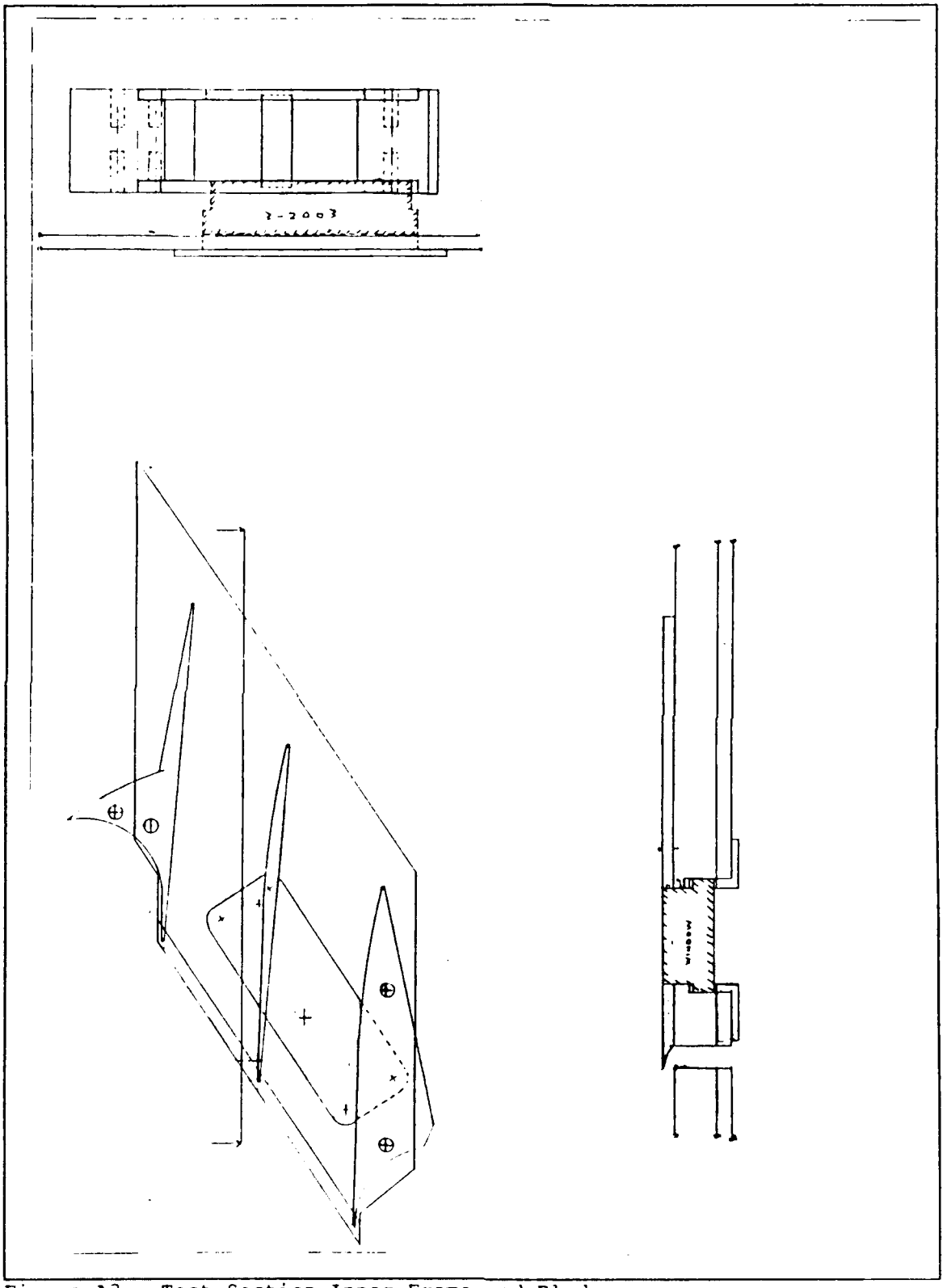

Figure A3. Test Section Inner Frame and Blades

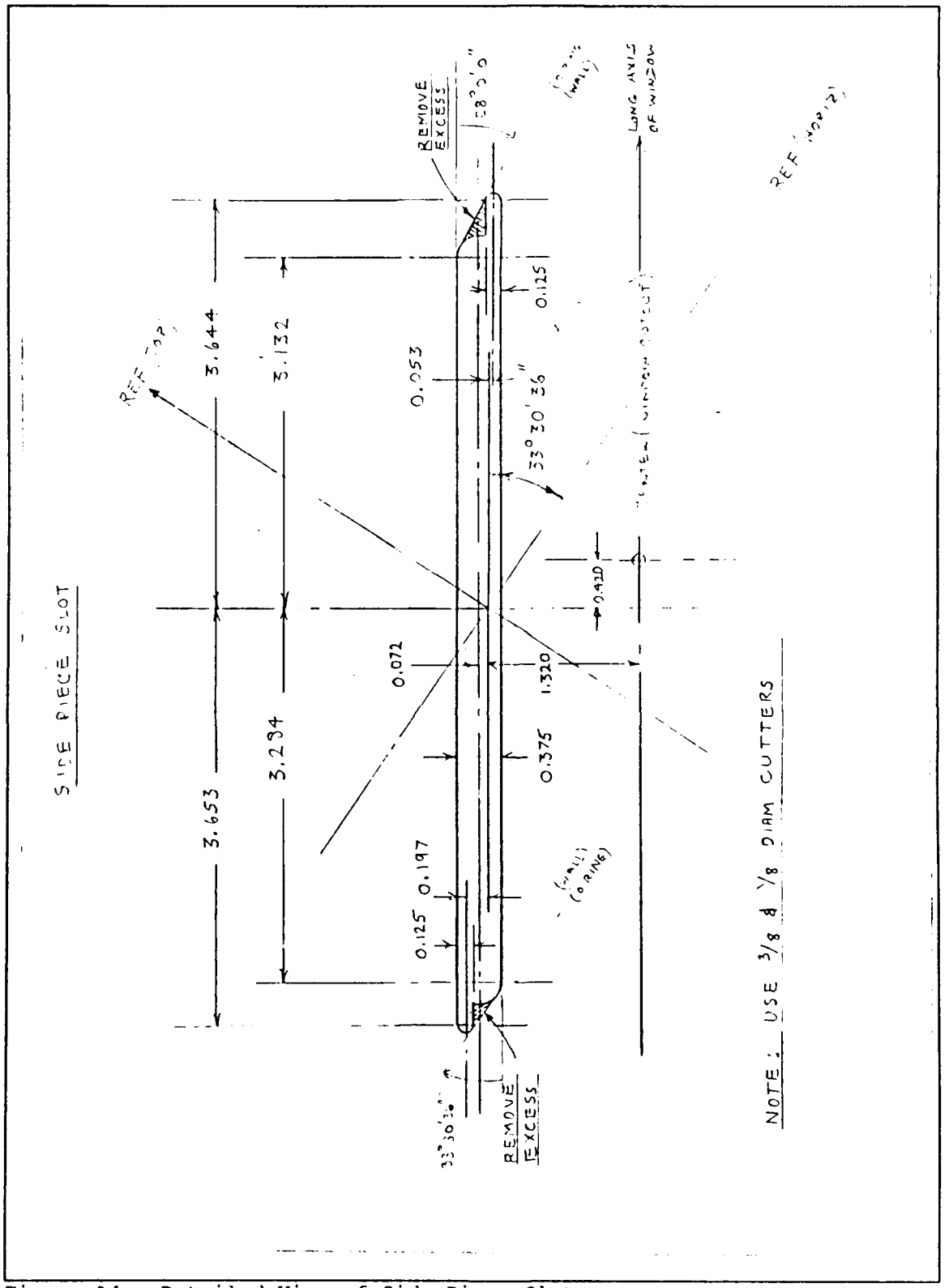

Figure A4. Detailed View of Side Piece Slot

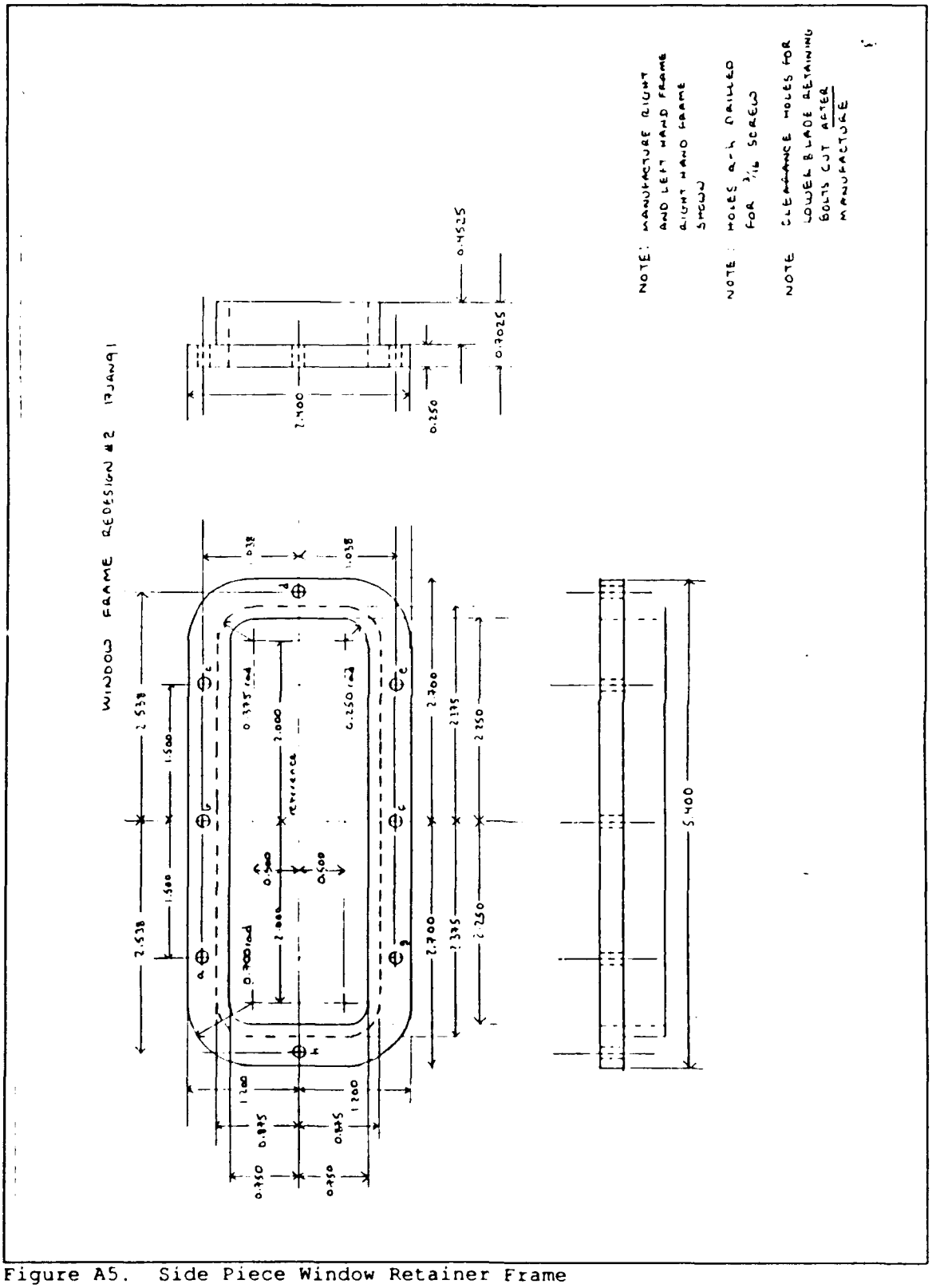

Figure A5. Side Piece Window Retainer Frame

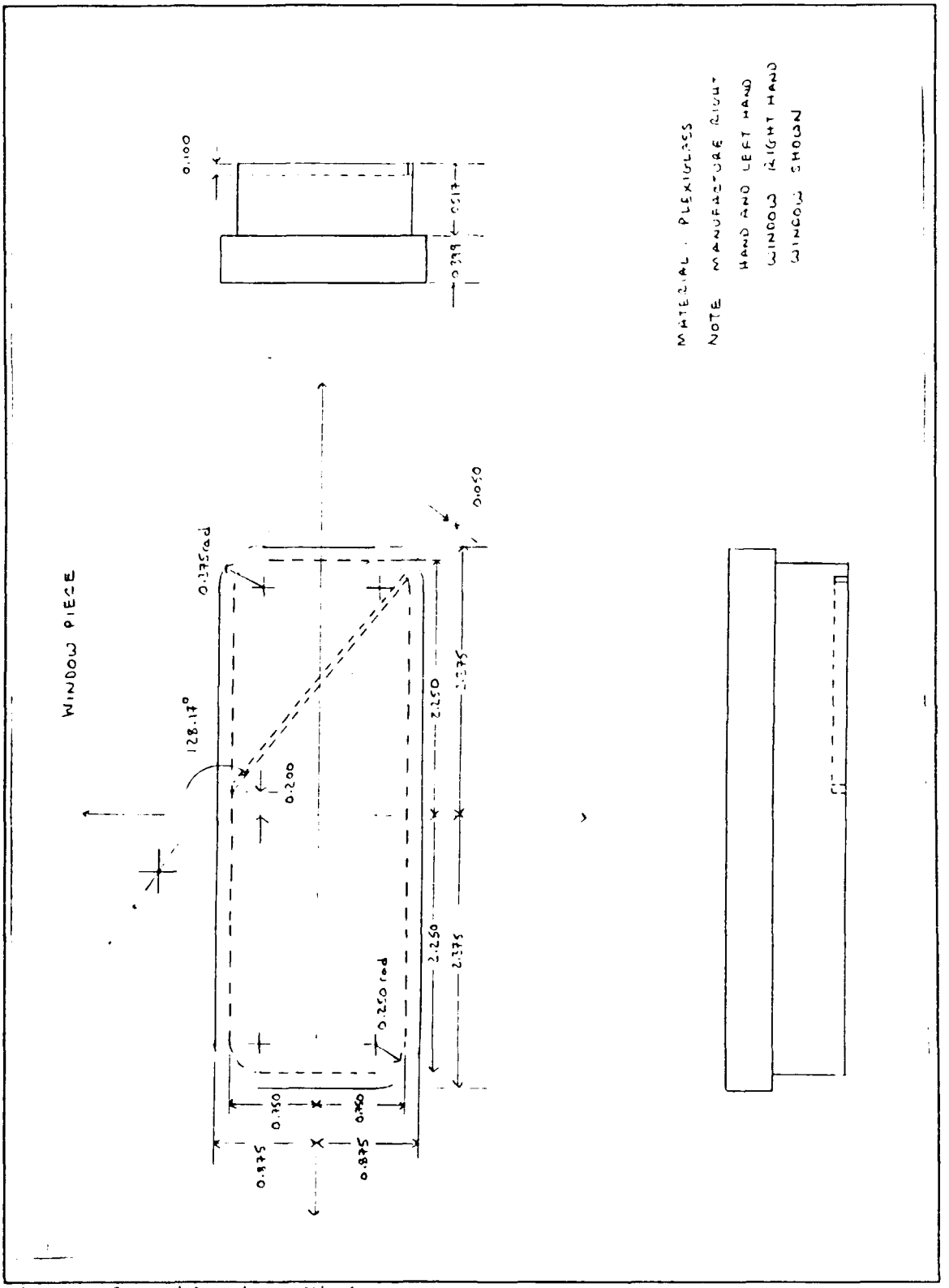

Figure A6. Side Piece Window

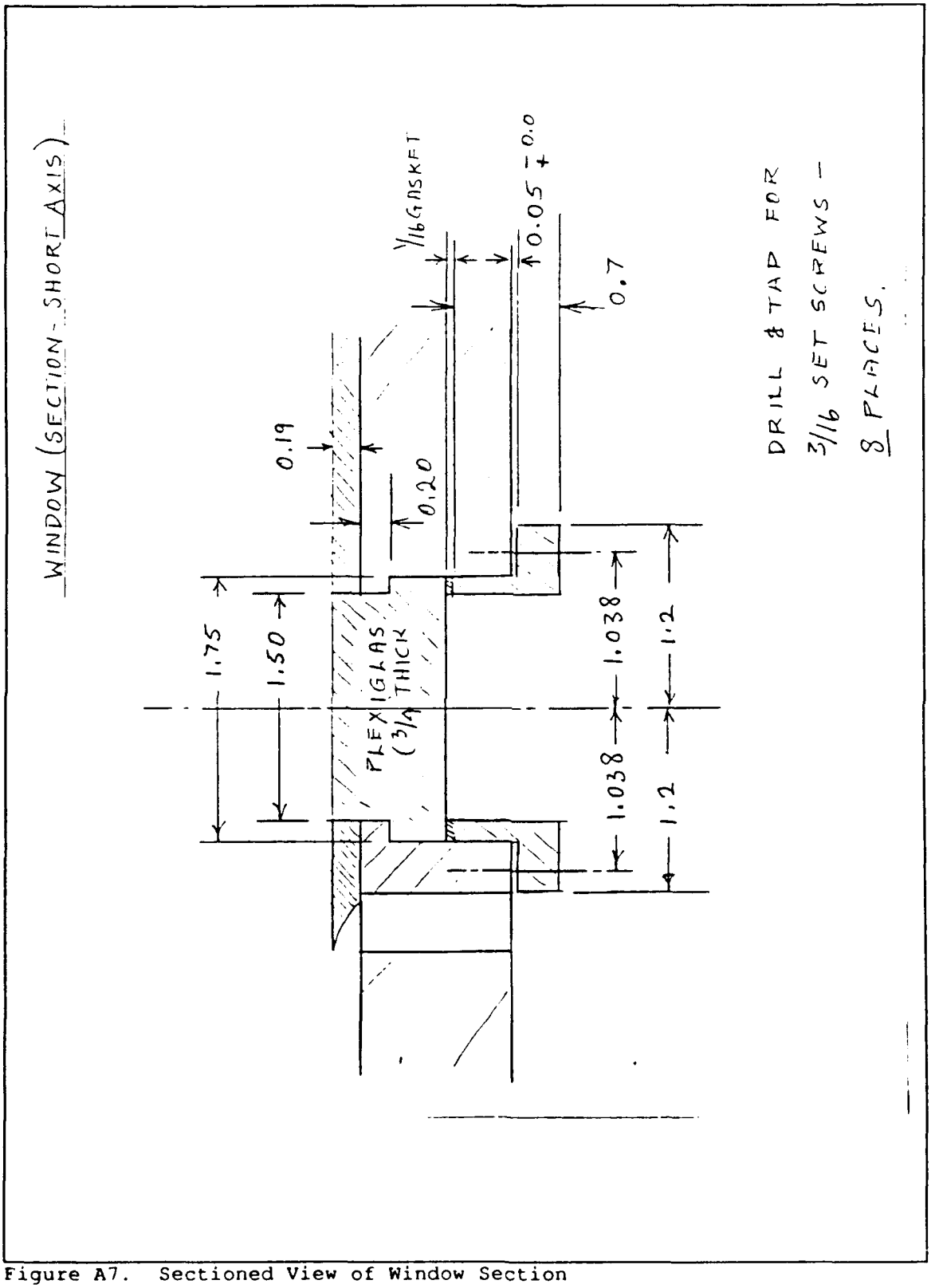

Figure A7. Sectioned View of Window Section

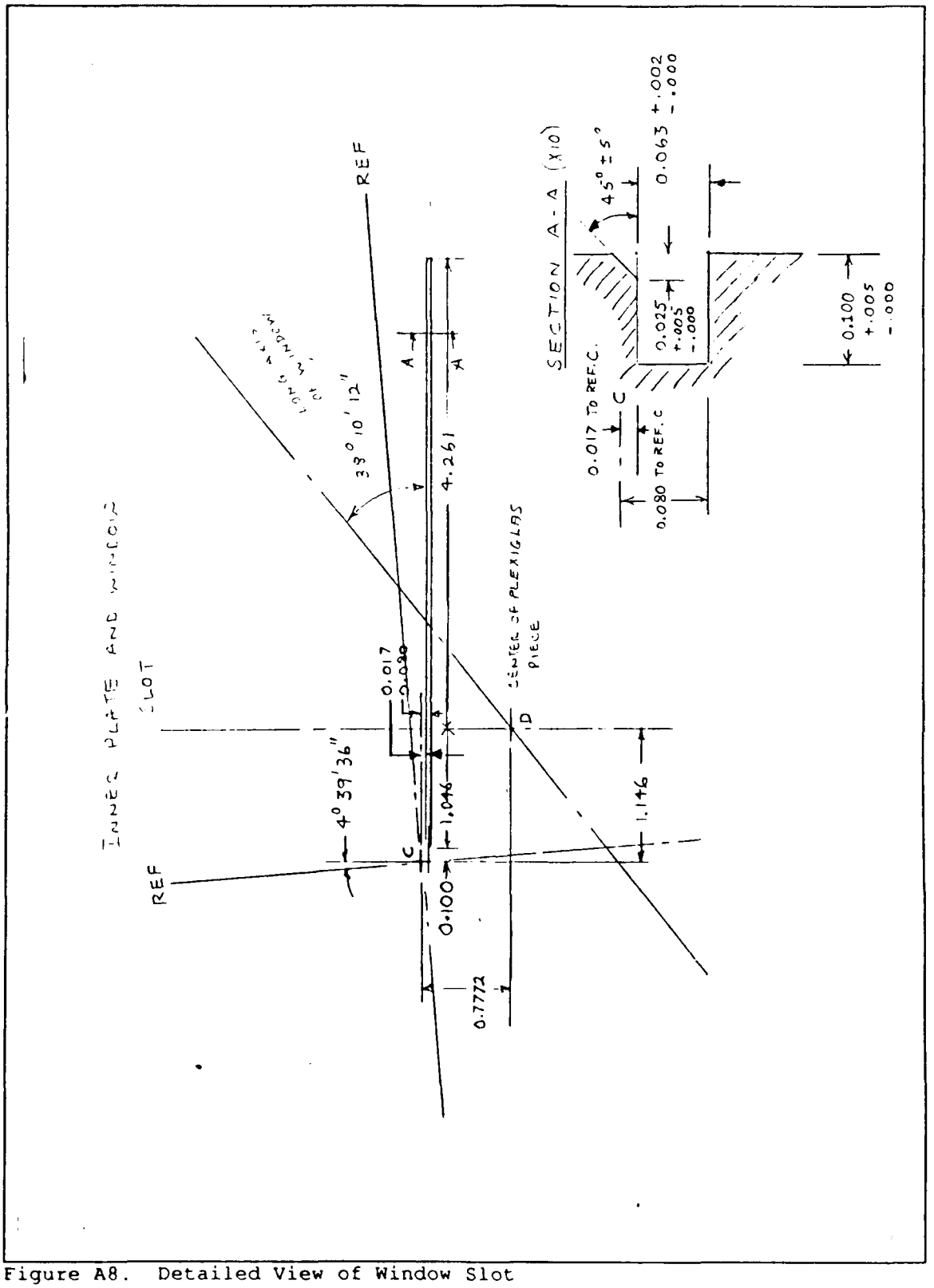

Figure A8. Detailed View of Window Slot

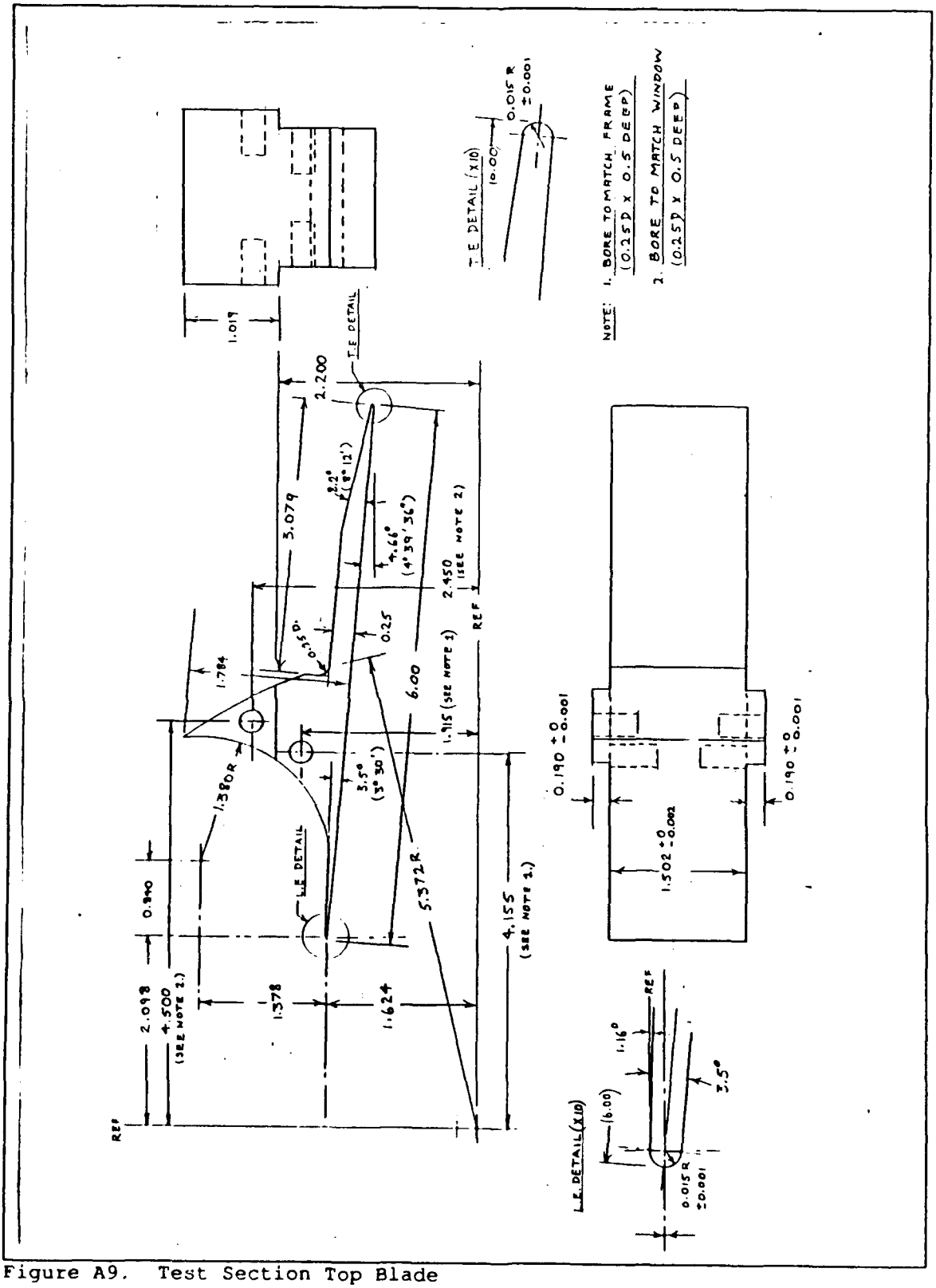

Figure A9. Test Section Top Blade

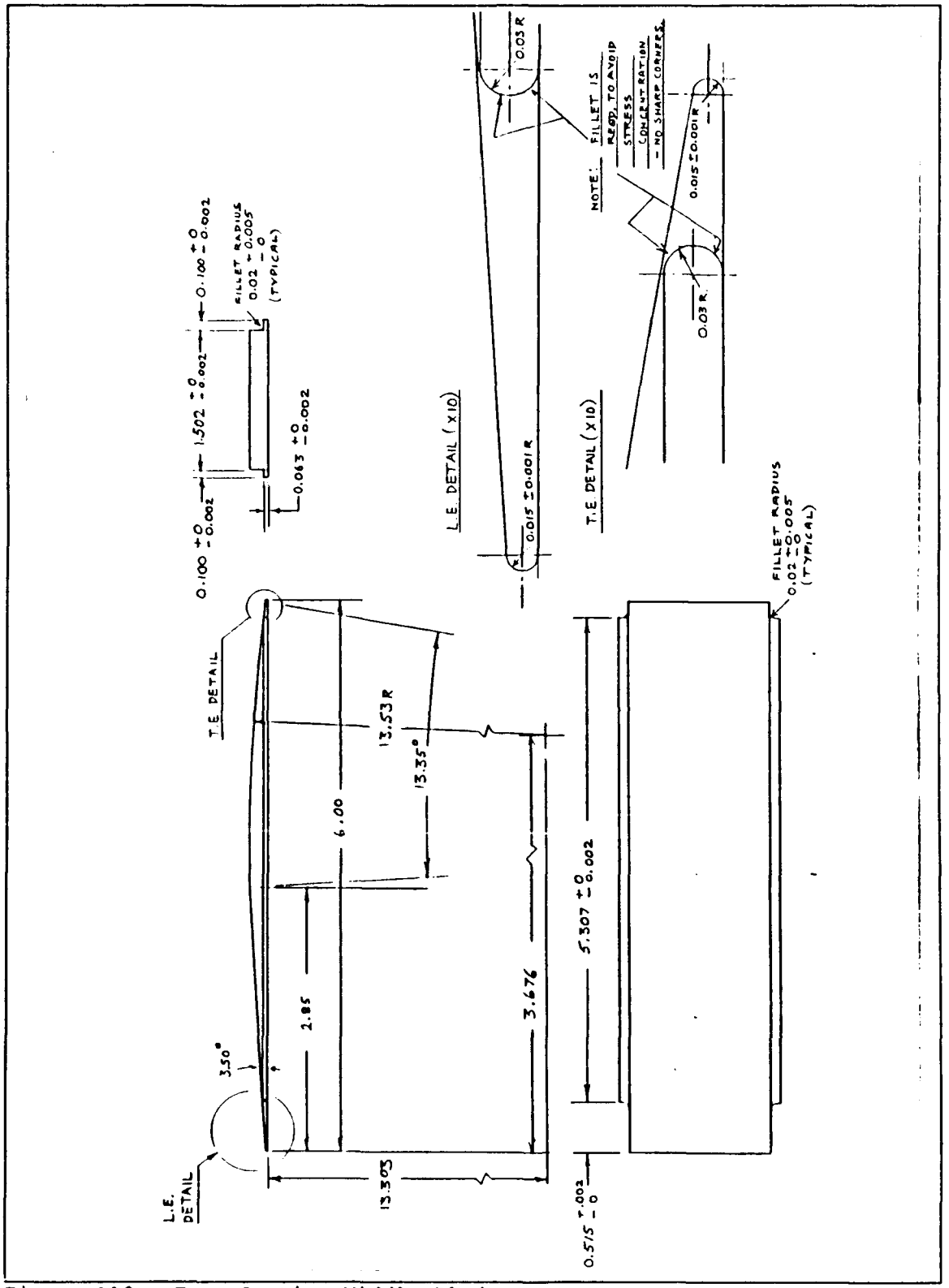

Figure A10. Test Section Middle Blade

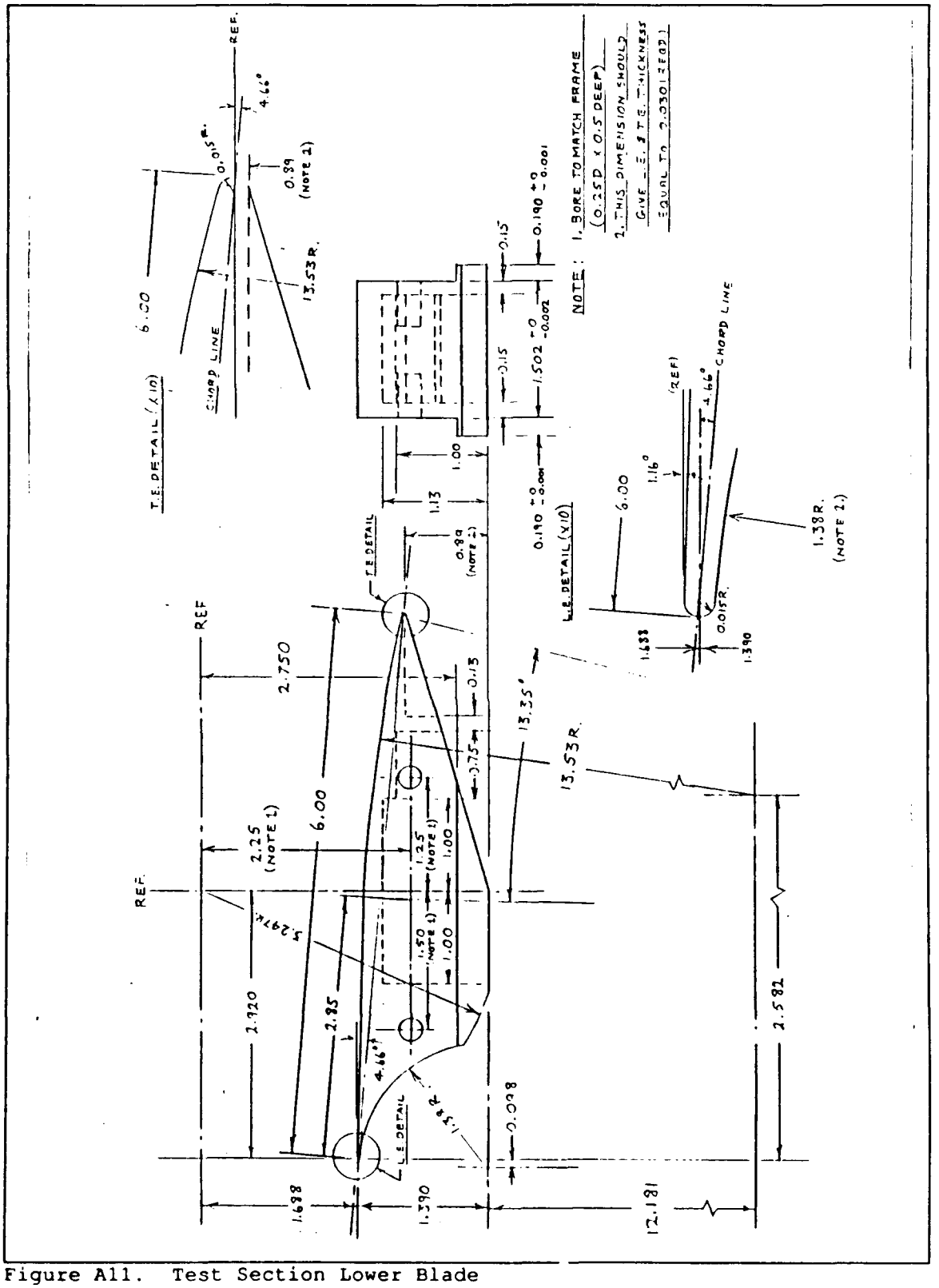

Figure A11. Test Section Lower Blade

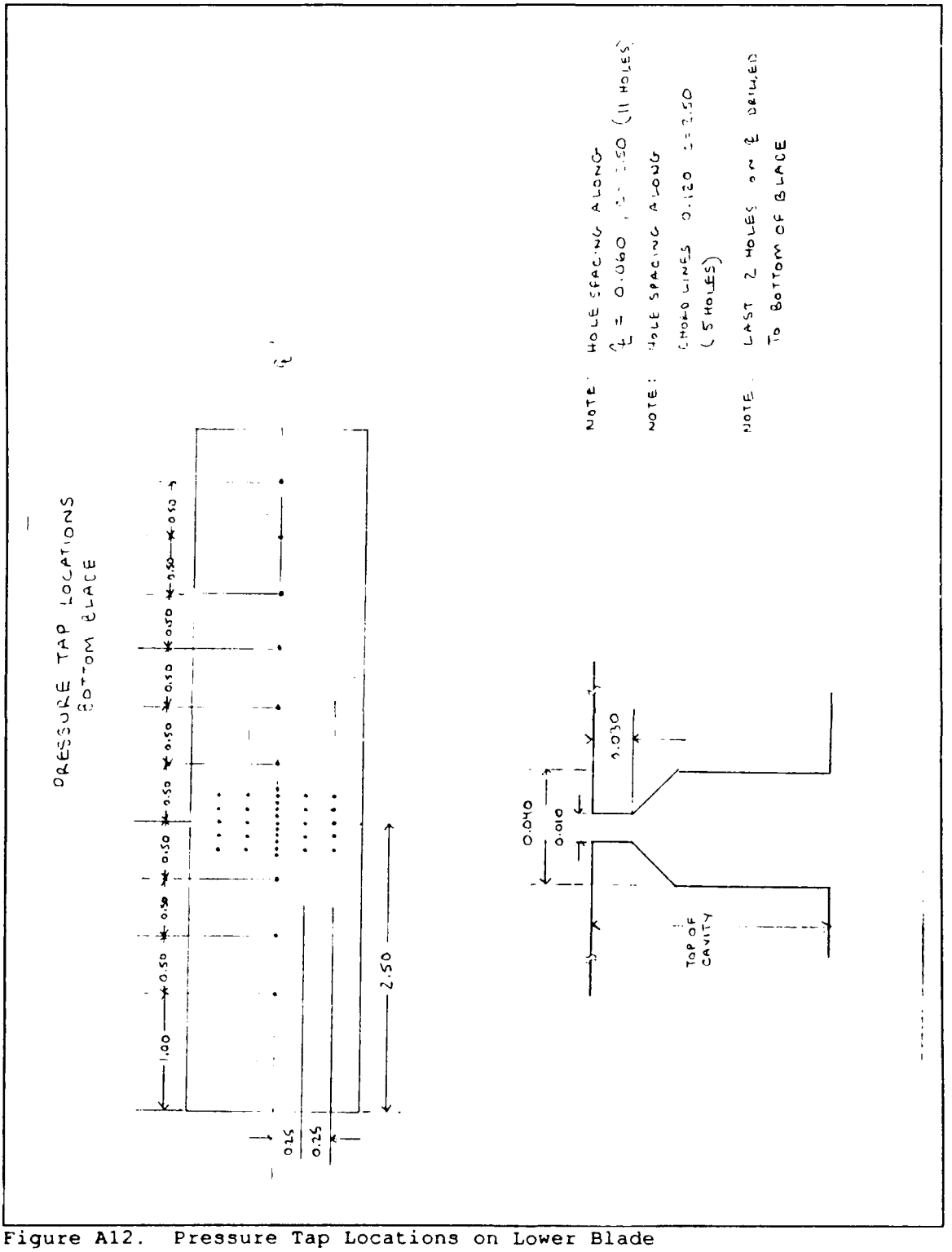

Figure A12. Pressure Tap Locations on Lower Blade

APPENDIX B

DATA ACQUISITION PROGRAM

```
10 REM ----------TXC001----------R.P.SHREEVE-----3 14 91
20 REM
30 REM  THIS PROGRAM IS FOR DATA ACQUISITION
40 REM  FROM A SCANIVALVE ON THE TRANSONIC CASCADE
50 REM
60 REM  VARIABLES:
70 REM
80 REM
90 REM
100 REM
110 REM
120 REM
130 REM
140 REM
150 REM
160 REM
170 REM  DATE:  MAR 14, 1990
180 REM
190 DIM A[5,10],D[5,10],F[10],C$[30],A$[5]
200 MAT A=ZER
210 MAT D=ZER
220 MAT F=ZER
230 F[1]=1
231 F[2]=2
232 F[3]=3
234 F[4]=4
235 F[5]=5
237 F[6]=6
238 F[7]=7
239 F[8]=8
240 DISP "ENTER ATMOSPHERIC PRESS (IN HG)";
250 INPUT P8
260 DISP "ENTER NO. POINTS TO TAKE (MAX=5)";
270 INPUT S1
275 DISP "PRESS (CONT) WHEN READY";
276 STOP
280 FORMAT B
290 FORMAT 2B
300 FORMAT 4B
310 FORMAT F3.0
320 REM
330 REM  INITIALIZE BUS AND ASSIGN DATA ELEMENTS
340 REM
350 WRITE (13,300)256,20,768,512;
360 CMD "?D#","F1R7M3A0H0T3"
370 REM
380 REM
390 REM
400 V=1
410 C1=0
420 S=1
430 REM
440 REM BEGIN DATA SAMPLING
450 REM
460 FOR I=1 TO S1
470 FOR J=1 TO 8
```

Figure B1. Data Acquisition Program TXC001

```
470 CMD "DV"
475 WRITE @13,200;V
480 A=F[J]
490 GOSUB 1450
500 I1=0
510 REM
520 REM PRESSURE PATH
530 REM
540 CMD "?D"
550 WRITE @13,200;V
560 FOR L=1 TO 5
570 CMD "?D!"
580 WRITE @13,210;V+2
590 CMD "?D#","T3"
600 CMD "?L#"
610 ENTER @13,+;D1
620 I1=I1+D1
630 NEXT L
640 A1=I1/5
650 D[J,J]=A1
651 D[J,10]=P8
660 NEXT J
670 GOTO 770
680 REM---READ AIMOS TEMPERATURE ON SCANNER CHANNEL 0
690 REM
700 CMD "?D<","C"
710 OUTPUT @13,210;1
720 CMD "?D#","T3"
730 CMD "?C#"
740 ENTER @13,+;D[1,7]
750 CMD "?D<","C"
760 REM
770 REM
780 PRINT
790 PRINT "DATA SAMPLES FOR POINT"
800 PRINT
810 FOR I=1 TO 10
820 WRITE @15,830;I,D[J,I]
830 FORMAT F3.0,5X,F13.6
840 NEXT I
850 DISP "IS DATA VALID? 1=YES 0=RETRIE ";
860 INPUT A2
870 IF A2=1 THEN 890
880 GOTO 470
890 NEXT K
900 REM
910 REM DEFINITION OF DATA ARRAY
930 REM
930 REM*************************************
940 REM D(*,1) = OPEN (AIMOS PRESS.)
950 REM D(*,2) = CALIBRATION PRESS.(SWITCHED)
960 REM D(*,3) = OPEN
970 REM D(*,4) = PLENUM PRESSURE
980 REM D(*,5) = OPEN
990 REM D(*,6) = UPSTREAM STATIC PRESSURE
1000 REM D(*,7) = OPEN
1010 REM D(*,8) = DOWNSTREAM STATIC PRESSURE
1020 REM D(*,9) = OPEN
1030 REM D(*,10) = ATMOSPHERIC PRESSURE
1040 REM*************************************
1050 REM
1060 REM DATA CONVERSION & STORAGE
1070 REM
1080 FOR I=1 TO 51
1090 A(I,1)=D[I,1]*100000
1100 A(I,2)=D[I,2]*100000
1110 A(I,3)=D[I,3]*100000
1120 A(I,4)=D[I,4]*100000
```

Figure B1 (cont). Data Acquisition Program TXC001

```
1130 A(I,5)=D(I,5)+100000
1140 A(I,6)=D(I,6)+100000
1150 A(I,7)=D(I,7)+1000*34.7279+32.6149
1160 A(I,8)=D(I,8)
1170 A(I,9)=D(I,9)
1180 A(I,10)=D(I,10)
1190 NEXT I
1195 DISP "OPEN DATA FILE AND CONT.130ms":
1196 STOP
1200 DISP "ENTER DATA FILE NAME":
1210 INPUT A$
1220 FILES *
1230 ASSIGN A$,1,L,P
1240 WAIT PRINT # 1;D
1250 PRINT "DATA STORED IN FILE ";A$
1260 PRINT
1270 REM
1435 PRINT
1436 PRINT "ATMOSPHERIC PRESSURE = "P0
1440 END
1450 REM*****************************************
1460 REM  SUBROUTINE "POSIT"
1470 GOSUB 1650
1480 D=A-F
1490 CMD "^D"
1500 IF D 0 THEN 1580
1510 IF D 0 THEN 1580
1520 RETURN
1530 REM    HOME S V
1540 WRITE (13,310)V+4
1550 WRITE (13,*)"C"
1560 WAIT 400
1570 GOTO 1470
1580 REM     ADVANCE S V
1600 WRITE (13,310)V-1
1610 WRITE (13,*)"C"
1620 WAIT 50
1640 GOTO 1470
1650 REM     READ S V ADDRESS
1660 CMD "^G$"
1670 P0=PEEKBYTE13
1680 L=BIAND(P0,15)
1690 T=ROT(P0,4)
1700 M=BIAND(T,7)
1710 P=10*M+L
1720 WRITE (13,280)256,95:
1730 RETURN
```

Figure B1 (cont). Data Acquisition Program TXC001

APPENDIX C

PROGRAM TO DRAW A WEDGE-ARC CASCADE

```
10 REM----------SSCB03----------P.P.SHREEVE ----------10 19 90
20 REM-----PROGRAM TO CALC. & DRAW A WEDGE-ARC CASCADE BLADE
30 REM-----INTO A CASCADE
35 DEG
40 DATA 6,0.015,3.5,2.85,-51.84,2.90
50 READ C0,R0,A1,W1,G0,S0,G9
54 A0=-G0
55 D1=P0*(1-COSA0-SINA0)
56 D2=P0*(1-COSA0+SINA0)
57 S1=C0*SINA0 S0
58 S2=C0 S0
60 REM-----CALC. BLADE GEOM.
70 X0=P0
80 Y0=R0
100 X1=X0-P0*SINA1
110 Y1=P0+R0*COSA1
120 X2=R0
130 Y2=0
140 E0=(P0 TAN(A1/2))-X2
150 A8=C0-P0-W1
160 A9=A8*A8
170 B8=P0-(W1+E0)*TANA1
180 B9=B8*B8
190 R1=(A9+B9-R0*R0)/(2*(A8*SINA1-B8*COSA1-P0))
200 X3=W1
210 Y3=(W1+E0)*TANA1
220 X4=X3+R1*SINA1
230 Y4=Y3-R1*COSA1
240 X7=C0-P0
250 Y7=P0
260 P1=ATN((X7-X4)/(Y7-Y4))
270 X5=X7+P0*SINP1
280 Y5=Y7+P0*COSP1
290 X6=X7
300 Y6=0
310 REM-------PRINT RESULTS
320 PRINT
330 PRINT
340 PRINT "WEDGE-ARC CACADE BLADE "
350 PRINT
360 PRINT "CHORD="C0,"WEDGE LENGTH="W1
370 PRINT "WEDGE ANGLE="A1"DEG","L.E.RADIUS="P0
380 PRINT "SURFACE RADIUS="R1,"PHI="P1"DEG."
390 PRINT "X0="X0
400 PRINT "X1="X1,"Y1="Y1
410 PRINT "X2="X2,"Y2="Y2
```

Figure C1. Cascade Geometry Program SSCB03

```
420 PRINT "X3="X3,"Y3="Y3
430 PRINT "X4="X4,"Y4="Y4
440 PRINT "X5="X5,"Y5="Y5
450 PRINT "X6="X6,"Y6="Y6
460 PRINT "X7="X7,"Y7="Y7
470 PRINT
471 PRINT "CASCADE GEOMETRY:"
472 PRINT "SETTING ANGLE="A0"DEG.","BLADE SPACE(N)="S1
473 PRINT "FOR SOLIDITY="S0,"BLADE SPACING="S2
480 PRINT
490 STOP
1000 REM-------UPHUPLANE
1010 SCALE -1.14,-.3,.8
1020 LABEL (".1.5,.3,0,10 15)
1030 FOR T=-90 TO 90-A1 STEP (180-A1) 30
1040 X9=R0*(1-COST)
1041 Y9=R0*(1+SINT)
1042 GOSUB 5000
1050 NEXT T
1060 X9=X3
1061 Y9=Y3
1062 GOSUB 5000
1070 FOR T=-A1 TO P1 STEP (A1+P1).250
1080 X9=X4+R1*SINT
1081 Y9=Y4+R1*COST
1082 GOSUB 5000
1090 NEXT T
1100 FOR T=-90+P1 TO 90 STEP (180-P1) 30
1110 X9=X7+R0*COST
1111 Y9=Y7-R0*SINT
1112 GOSUB 5000
1130 NEXT T
1130 X9=R0
1131 Y9=0
1132 GOSUB 5000
1140 PEN
1150 DISP "INPUT 2 FOR BLADE 2, 3 FOR 3 ":
1151 INPUT Z0
1153 D1=(Z0-1)*S2*COSG9
1154 D2=(Z0-1)*S2*SING9
1155 OFFSET D1,D2
1156 GOTO 1030
1160 END
5000 REM-----SUBROUTINE TO TRANSLATE AND ROTATE AXES
5010 X=(X9-D1)*COSG0+(Y9-D2)*SING0
5020 Y=(Y9-D2)*COSG0-(X9-D1)*SING0
5025 PLOT X,Y
5030 RETURN
```

Figure C1 (cont). Cascade Geometry Program SSCB03

APPENDIX D

DESCRIPTION OF THE NUMERICAL METHOD

A. REYNOLDS-AVERAGED NAVIER-STOKES EQUATIONS

The Reynold's-averaged Navier-Stokes equations are presented first. The unsteady, compressible Navier-Stokes equations are developed in Ref. 9. A complete derivation of the Reynold's averaging process can be found in Ref. 10, which is the source of the following description.

The time-dependent, compressible Navier-Stokes equations in tensor notation are as follows:

$$\rho_t + (\rho u_j)_j = 0$$

$$(\rho u_i)_t + (\rho u_i u_j + \sigma_{ij})_j = 0 \qquad i = 1,2,3 \tag{1}$$

$$(\rho E)_t + (\rho E u_j + u_i \sigma_{ij} + q_j)_j = 0$$

where subscript notation has been used to denote partial derivatives, eg. $\rho_t = \frac{\partial \rho}{\partial t}$, and the summation convention has been used for repeated indices. The stress tensor for a Newtonian fluid is given as

$$\sigma_{ij} = \delta_{ij} p - \mu \left(u_{i,j} + u_{j,i} - \frac{2}{3} \delta_{ij} u_{k,k} \right) \tag{2}$$

Here the Stokes hypothesis $3\lambda + 2 = 0$ has been used. The heat flux vector is obtained from the Fourier law of heat conduction as

$$q_j = -\kappa T_j = -\frac{\mu}{P_r} h_j \tag{3}$$

To derive the Reynold's-averaged Navier-Stokes equations, the averaging operation is defined as follows:

$$\overline{\rho}(x_j, t) = \frac{1}{2T} \int_{t-T}^{t+T} \rho(x_j, s)\, ds \tag{4}$$

where 2T is the time averaging interval, which is assumed to be large enough compared to the energy containing turbulent time scales but small when compared to the time scale of the average motion. It is assumed that there is a range of values of T where the mean density is independent of T.

The fluctuating density is defined as the difference between the density and its mean value.

$$\rho' = \rho - \overline{\rho} \tag{5}$$

The averages and fluctuating values for the other variables are defined similarly. It is assumed that the average of the fluctuations equals zero and the average of the average still is the average.

The time-averaged Navier-Stokes equations are obtained by averaging Eq. (1). The resulting equations involve terms similar to the following:

$$\overline{\rho u_i u_j} = \bar{\rho}\,\bar{u}_i\,\bar{u}_j + \bar{\rho}\,\overline{u'_i u'_j} + \bar{u}_i\,\overline{\rho' u'_j} + \bar{u}_j\,\overline{\rho' u'_i} + \overline{\rho' u'_i u'_j} \qquad (6)$$

For incompressible flows, where the average of the density fluctuation equals zero, the last three terms of Eq. (5) are dropped. The compressible equations contain additional terms, such as $\overline{u_i'' \rho' u_j''}$, therefore, an alternative method for averaging velocity and energy terms is followed. This method is called mass-averaging (Favre-averaging) with the following definitions:

$$\tilde{u}_i = \overline{\rho u_i}/\bar{\rho} \qquad \tilde{h} = \overline{\rho h}/\bar{\rho} \qquad (7)$$

$$u''_i = u_i - \tilde{u}_i \qquad h'' = h - \tilde{h} \qquad (8)$$

It is important to note that the averages of the fluctuating quantities for Favre-averaging is not zero.

$$\overline{u''_i} = -\overline{\rho' u'_i}/\bar{\rho} \qquad \overline{h''} = -\overline{\rho' h'}/\bar{\rho} \qquad (9)$$

However, the mass-weighted variables are zero.

$$\overline{\rho u''_i} = 0 \qquad \overline{\rho h''} = 0 \qquad (10)$$

By introducing the mean and fluctuating quantities into Eq. (1) and averaging, the Reynold's-averaged Navier-Stokes equations are obtained.

$$\overline{\rho}_t + (\bar{\rho}\tilde{u}_j)_j = 0$$

$$(\bar{\rho}\tilde{u}_i)_t + (\bar{\rho}\,\overline{u_i u_j} + \sigma_{ij})_j = 0 \qquad (11)$$

$$(\bar{\rho}E)_t + (\bar{\rho}E\tilde{u}_j + \tilde{u}_j\sigma_{ij} + q_j)_j = 0 \qquad i=1,2,3$$

$$\sigma_{ij} = \sigma_{ij}^M + \sigma_{ij}^T, \qquad q_j = q_j^M + q_j^T$$

The following are identified by name:

$$\textit{Reynold's Stress Tensor:} \quad \sigma_{ij}^T = \overline{\rho u_i'' u_j''}$$

$$\textit{Viscous Stress Tensor:} \quad \sigma_{ij}^M = -\bar{p}\delta_{ij} - \mu(\tilde{u}_{i,j} + \tilde{u}_{j,i} - \frac{2}{3}\delta_{ij}\tilde{u}_{k,k})$$

$$\textit{Reynold's Heat Flux Vector:} \quad q_j^T = \overline{\rho h'' u_j''} \qquad (12)$$

$$\textit{Molecular Heat Flux Vector:} \quad q_j^M = -\frac{\mu}{Pr}\tilde{h}_j$$

$$\textit{Total Energy:} \quad E = e + k + \tilde{u}_k\tilde{u}_k/2$$

$$\textit{Turbulent KE:} \quad k = \overline{\rho u_k'' u_k''}/2\bar{\rho}$$

It is assumed that μ is independent of time, but depends on temperature variations.

The Reynold's stresses are related to the mean flow quantities through turbulence modeling. The turbulence models used in the present work are discussed in the next section. When the Reynold's stresses and heat fluxes are related algebraically to the mean flow quantities, the resulting models are called algebraic turbulence models. The algebraic turbulence models are either mixing length-type models or eddy viscosity-type models. In the present study the widely used Baldwin-Lomax algebraic eddy-viscosity model was used.

The eddy viscosity models are zero-equation models, and the eddy viscosity is modeled algebraically. More complex models exist that take into account the transport of certain turbulence quantities such as kinetic energy or shear stress. These models are derived from simplified forms of the Navier-Stokes equations for mean and fluctuating quantities [Ref. 11].

A simple one-equation model that is specially designed to predict shock-boundary layer separated flows, the Johnson-King model [Ref. 12] was used in the present investigation. This model was considered to be most suitable for the computation of the nonequilibrium flow in the recovery region after the shock-induced separation, based on the experimental data given in Ref. 12. Figure D1 shows a comparison of predictions for the separated flow region after a transonic shock using four turbulence models. The Johnson-King and RNG models exhibit the best results. The Baldwin-Lomax model and the Johnson-King model are briefly described in the next section.

B. TURBULENCE MODELING

1. Baldwin-Lomax Model

The Baldwin-Lomax model is a two layer algebraic model which does not require the finding of the boundary layer quantities, as does the Cebeci-Smith model. Instead, the outer and inner eddy viscosities are scaled by the vorticity. A complete formulation of the model is given in Ref. 13.

2. Johnson-King Model

The shock-separated region is computed with the Johnson- King turbulence model. A detailed description of the development of the model is given in Ref 12. The basic formulation of the model necessary for the numerical implementation is presented briefly.

The Johnson-King turbulence model was developed for the purpose of improving the predictions of pressure driven separated flows and transonic shock-induced separated flows. The Cebeci-Smith model [Ref. 10] was proven fairly accurate, even though it was based on the invalid assumption that the turbulent shear stress depends only on the local properties of the mean flow. The Johnson-King model develops a closure for boundary-layer flows without attempting to predict the production, dissipation and diffusion of the turbulent kinetic energy and the dissipation rate, throughout the entire viscous layer, as in two-equation models.

To account for convection and diffusion effects on the Reynolds shear stress development, an ODE is developed to describe the maximum Reynolds shear stress development in the streamwise direction. The ODE describes the development of $\overline{u'v'} = \sqrt{\tau_t/\rho}$ along the path of maximum shear stress.

The eddy viscosity is given by

$$\nu_t = \nu_{t_o}\left[1 - \exp\left(-\frac{\nu_{t_i}}{\nu_{t_o}}\right)\right] \tag{13}$$

where ν_{ti} and ν_{to} describe the eddy viscosity variation in the inner and outer parts of the boundary layer. The inner eddy viscosity is computed as

$$\nu_{t_i} = D^2 \kappa z \sqrt{(-\overline{u'v'})_{max}} \tag{14}$$

$$D^2 = 1 - e^{(-z/A^+)}$$

where the constant $A^+ = 15$. The outer eddy viscosity is given by

$$\nu_{t_o} = \sigma(x) \cdot [0.0168 U_e \delta^* \gamma] \tag{15}$$

where γ is Klebanoff's intermittency function

$$\gamma = [1 + 5.5(\frac{z}{\delta})^6]^{-1} \tag{16}$$

and $\sigma(x)$ is the solution of the ODE mentioned earlier.

To complete the formulation, an equation is needed for $\overline{u'v'}_m$. This equation is developed from the turbulence kinetic energy equation. The result is the following ODE after a change of variables:

$$\frac{dg}{dx} = \frac{a_1}{2\overline{u}_m L_m}\left[(1 - \frac{g}{g_{eq}}) + \frac{C_{dif} L_m}{a_1 \delta [0.7 - (y/\delta)_m]} \left|1 - (\frac{\nu_{t_o}}{\nu_{t_{o,eq}}})^{\frac{1}{2}}\right|\right] \tag{17}$$

where C_{dif} and a_1 are modeling constants, $\overline{u}_m$ is the maximum average mean velocity, g and g_{eq} are given as

$$g = 1/\sqrt{(-\overline{u'v'})_m} \quad and \quad g_{eq} = 1/\sqrt{(-\overline{u'v'})_{m,eq}} \tag{18}$$

and L_m is the dissipation length evaluated as

$$L_m = 0.40z \qquad z_m/\delta \le 0.225 \tag{19}$$

$$L_m = 0.09\delta \qquad z_m/\delta \ge 0.225$$

The equilibrium shear stress, g_{eq}, is determined from the following equilibrium eddy

viscosity distribution

$$\nu_{t,eq} = \nu_{t_o,eq}[1 - \exp(-\frac{\nu_{t_i,eq}}{\nu_{t_o,eq}})]$$

$$\nu_{t_i,eq} = D^2 \kappa z \sqrt{(-\overline{u'v'})_{m,eq}} \tag{20}$$

$$\nu_{t_o,eq} = 0.0168 u_e \delta^* \gamma$$

An implicit Euler method is used for the numerical solution of Eq.(17), and the maximum shear stress at each iteration level is updated as follows:

$$\sigma(x)^{n+1} = \sigma(x)^n \frac{\nu_{t_o}^{n+1}}{\nu_{t_o}^n} \tag{21}$$

Solutions with the Johnson-King turbulence model were obtained as follows. First a convergent solution using the Baldwin-Lomax turbulence model for the entire flow field was obtained. Then the Johnson-King model was applied to the upper part of the airfoil. To initiate the solution $\sigma(x)$ in Eq.(15) is set equal to one, and it is allowed to change according to Eq.(21) until the final solution is obtained. Note that the Johnson-King model reduces to the Cebeci-Smith model when $\sigma(x)$ is identically equal to one.

C. COMPUTATIONAL METHOD

The following section was developed using notes from J. Ekaterinaris.

1. Discontinuous Solutions and Entropy Method

The numerical solution of the initial value problem for hyperbolic systems of conservation laws consists of the solution of

$$u_t + f_x(u) = 0 \qquad (22)$$

$$u(x,0) = u_0(x)$$

where u(x,t) is the vector of m unknowns and f(u) is the flux, a vector valued function of m components. The matrix form of Eq.(22) is

$$u_t + Au_x = 0$$

Because the system is assumed hyperbolic, all the eigenvalues of the Jacobian matrix are real and positive.

To allow for discontinuous solutions we admit weak solutions which satisfy Eq.(22) in the sense of distribution theory as shown below

$$\int_{z=0}^{\infty}\int_{x=-\infty}^{\infty} \{\phi_t u + \phi_x f(u)\}\, dxdt + \int_{-\infty}^{\infty} \phi(x,0)\, u_0(x)\, dx = 0 \qquad (23)$$

where ϕ are C^{∞} test functions that vanish for $|x| + t$ large. The hyperbolic system is satisfied in a pointwise sense by a piecewise smooth solution in each smooth region, while across each discontinuity the Rankine-Hugoniot relation

$$f(u_R) - f(u_L) = C(u_R - u_L) \qquad (24)$$

holds where C is the speed of propagation of the discontinuity, and the left and right states are designated u_L and u_R, respectively.

The conservation law Eq.(22) is considered to possess an entropy function E(u) defined as

- E is a convex function of u, $E_{uu} \geq 0$ convexity
- E satisfies $E_u f_u = F_u$ compatability

where F is the entropy flux function.

The convexity condition forces irreversible processes to run in the correct direction and produce entropy. A consequence of the compatability condition is that the reversible processes do not produce entropy. Note that the mathematical entropy E, and physical entropy $S = \log(p/\rho^\gamma)$, statements are compatable, and if one is true then the other is true.

Every smooth solution of Eq.(22) then satisfies

$$E_u(t) + F_x(u) = 0 \tag{25}$$

If u is piecewise smooth with discontinuities, then Eq.(25) holds pointwise in the smooth regions; and across a discontinuity

$$F(u_R) - F(u_L) \leq C[E(u_R) - E(u_L)] \tag{26}$$

Consider for simplicity that the numerical approximation to weak solutions of Eq.(22) are obtained by the following explicit scheme

$$u_i^{n+1} = u_i^n - \frac{\Delta t}{\Delta x}(f_{i+1/2}^n - f_{i-1/2}^n) \tag{27}$$

where $f_{i+1/2}^n$ is a numerical flux defined as

$$f_{i+1/2}^n = f(u_i^n, u_{i+1}^n)$$

It is required that the numerical flux is consistent with the physical flux in the following sense

$$f(u,u) = f(u)$$

In addition, the differencing scheme is consistent with the entropy condition if the inequality of

$$E_i^{n+1} \leq E_i^n - \frac{\Delta t}{\Delta x}(F_{i+1/2}^n + F_{i-1/2}^n) \tag{28}$$

is satisfied where

$$E_i^{n+1} = E(u_i^{n+1})$$

and

$$F_{i+1/2}^n = F(u_i^n, u_{i+1}^n)$$

Assume that the difference scheme in Eq.(27) is consistent with the hyperbolic conservation law Eq.(22) and the entropy condition Eq.(26). Let u_i^n be a solution of Eq.(27) for initial values $u_i^0 = a(j\Delta)$. Suppose that for lim $\Delta x \rightarrow 0$ ($\Delta x = x/i_{max}$) and $\Delta t \rightarrow 0$ ($\Delta t = T/N$)

$$\lim_{\substack{\Delta x \to 0 \\ \Delta t \to 0}} u_i^n = u(x,t)$$

the limit exists in the sense of L_1 norm convergence. Then the limit satisfies the weak form of the conservation law Eq.(23) and the weak form of the entropy condition given by

$$-\int_0^{\infty}\int_{-\infty}^{\infty} (\phi_t E + \phi_x E)\, dxdt - \int_{-\infty}^{\infty} \phi(x,0)\, E(u_0(x))\, dx \le 0$$

where ϕ is a nonnegative smooth test function $\phi(x,t)$ possessing a compact support.

Assume that the initial data corresponds to some reference state u^* for large $|x|$

$$u_0(x) = u^* \qquad |x| > M$$

then

$$u_i^n = u^* \quad for \quad \Delta xi > M + n\Delta x$$

Without altering the convexity of the entropy function an inhomogeneous function can be added to obtain

$$E(u^*) = 0 \qquad E_{u_i}(u^*) = 0$$

By summing Eq.(28) with respect to i to obtain

$$\sum_i E_i^{n+1} \le \sum_i E_i^n$$

shows that entropy is a decreasing function of time, and

$$\sum_i E_i^n \le \sum_i E_i^0$$

indicates that the scheme is stable.

This condition is not strong enough to prove pointwise boundness of the solutions or the existence of convergent subsequences. Solutions of equations with compressible flow must ensure that the difference scheme used keeps the variables within their physical

range (density and pressure are always positive quantities). The above development is true for any number of space variables. In addition, they hold for multidimensional schemes consisting of one-dimensional factional steps provided that each individual one-dimensional step satisfies the entropy inequality.

2. Upwinding Schemes for Linear Hyperbolic PDE's

A linear constant coefficient hyperbolic PDE has the form

$$\frac{\partial u}{\partial t} + a\frac{\partial u}{\partial x} = 0 \tag{29}$$

The numerical approximation of the solution at $x = i\Delta x$, $t = n\Delta t$ is U_i^n where Δx is the spatial mesh size and Δt is the time step. A simple first-order accurate upwinding scheme that takes into account the direction of wave propogation, according to the characteristic theory of hyperbolic PDE's, which may be used for the solution of Eq.(29) is as follows

$$U_i^{n+1} = u_i^n - \lambda a \begin{cases} u_{i+1}^n - u_i^n & a < 0 \\ u_i^n - u_{i-1}^n & a > 0 \end{cases} \tag{30}$$

where $\lambda = \Delta t/\Delta x$. This numerical scheme can be written in the following single equation form

$$U_i^{n+1} = u_i^n - \frac{\lambda}{2} a [u_{i+1}^n - u_{i-1}^n] + \frac{\lambda}{2}|a|(u_{i+1}^n - 2u_i^n + u_{i-1}^n) \tag{31a}$$

or

$$u_i^{n+1} = u_i^n - \lambda [a^+(u_i^n - u_{i-1}^n) + a^-(u_{i+1}^n - u_i^n)] \tag{31b}$$

where $a^+ = 1/2\ (a + |a|)$, $a^- = 1/2\ (a - |a|)$.

Higher order upwind schemes may be obtained by increasing the order of accuracy of the stencils of Eq.(30) in the upwind direction.

The preceding ideas may be generalized for a system of hyperbolic equations with constant coefficients of the following form

$$\frac{\partial U}{\partial t} + A\frac{\partial U}{\partial x} = 0 \qquad (32)$$

where U is a vector of m unknowns and A is a m x m constant coefficient matrix having real eigenvalues. Let X be the eigenvalue transformation diagonalizing A as $X^{-1}AX = \Lambda$, where Λ is the diagonal eigenvalue matrix. Then Eq.(32) can be rearranged in diagonal form as

$$\frac{\partial W}{\partial t} + \Lambda\frac{\partial W}{\partial x} = 0 \qquad (33)$$

where $W = X^{-1}U$.

Application of the numerical schemes shown in Eq.(31) for the vector equation in Eq.(33) yields

$$W_i^{n+1} = W_i^n - \frac{\lambda}{2}\Lambda\{W_{i+1}^n - W_{i-1}^n\} + \frac{\lambda}{2}|\Lambda|\{W_{i+1}^n - 2W_i^n - W_{i-1}^n\} \qquad (34)$$

This scheme can be written in terms of the original variables as

$$U_i^{n+1} = U_i^n - \frac{\lambda}{2}A\{U_{i+1}^n - U_{i-1}^n\} + \frac{\lambda}{2}|A|\{U_{i+1}^n - 2U_i^n - U_{i-1}^n\} \qquad (35)$$

where $|A| = X\Lambda X^{-1}$. Similar to the one equation case the new variables A^+ and A^- may be defined as $A^+ = 1/2(A + |A|)$ and $A^- = 1/2(A - |A|)$. Equation (35) now takes the form

$$U_i^{n+1} = U_i^n - \lambda \{ \tilde{F}_{i+1/2} - \tilde{F}_{i-1/2} \} \qquad (36)$$

where

$$\tilde{F}_{i+1/2} = \tfrac{1}{2} [A(U_{i+1} + U_i) - |A|(U_{i+1} - U_i)]$$

$$\tilde{F}_{i-1/2} = \tfrac{1}{2} [A(U_i + U_{i-1}) - |A|(U_i - U_{i-1})]$$

The term $\tilde{F}$ is referred to as the numerical flux.

3. Conservative Schemes and Shock-Capturing Theory

The theory of modern shock-capturing numerical schemes for non-linear hyperbolic conservation laws such as the Euler equations relies on the basic first-order upwinding methods discussed in the previous section. High order shock-capturing methods suitable for gas dynamic hyperbolic equations and nonconstant coefficient cases use non-linear differencing schemes. This significantly affects the stability of these methods because the stability checking can only occur locally and for the linearized versions of the non-linear equations. This local, linearized stability is neither necessary nor sufficient for non-linear problems such as shock discontinuities. Traditional methods of removing non-linear instability involve the introduction of linear or non-linear numerical dissipation (artificial viscosity or smoothing) into the difference schemes. This approach alone does not guarantee convergence to a physically correct solution, and higher order accurate upwind schemes have been developed recently to overcome the deficiencies of the artificial dissipation approach.

The limit solution of any finite-difference scheme in a conservation form consistent with the conservation laws satisfies the jump conditions across a discontinuity automatically [Ref. 14]. Weak solutions (solutions with shocks and contact discontinuities) of hyperbolic laws are not uniquely determined by their initial values except if the entropy condition, given in the previous section, is satisfied in order to pick out the physically relevant solution. Finite-difference approximations, however, always converge to a physically relevant solution when the numerical scheme used is monotone. If the scheme is not monotone then it must be consistent with the entropy inequality to assure convergence. These monotone schemes possess many desirable qualities required for the calculation of discontinuous solutions.

a. Monotone Schemes

Consider the scalar hyperbolic conservation law

$$u_t + a u_x = 0 \tag{37}$$

where $a(u) = \frac{\partial f}{\partial u}$ is a characteristic speed. A three-point explicit scheme in conservation form for the numerical integration is

$$u_i^{n+1} = u_i^n - \lambda (h_{i+1/2}^n - h_{i-1/2}^n) \tag{38}$$

where $\lambda = \Delta x/\Delta t$ and the numerical flux function $h_{i+1/2}^n = h(u_i^n, u_{i+1}^n)$ is consistent with the conservation law in the sense that $h(u_i,u_i) = f(u_i)$.

The numerical scheme in Eq.(38) is of the following generalized functional form and it is monotone if g is a monotonically increasing function of each of its arguments.

$$u_i^{n+1} = g(u_{i-1}^n, u_i^n, u_{i+1}^n) \tag{39}$$

Monotone schemes have the attractive property of producing smooth transitions near discontinuities, but they are only first order accurate. Unfortunately, not all first-order upwind schemes are monotone. In addition, monotone, first-order upwind schemes cannot produce solutions for the flow field with the required accuracy using reasonable grid spacing. Still, higher-order shock-capturing schemes required for practical computations require some linear or non-linear numerical dissipation. Unfortunately, these higher order schemes suffer from the following deficiencies: they produce spurious oscillations when the solution is not smooth, they may develop instabilities at discontinuities and they may select nonphysical solutions.

Two classes of modern shock-capturing schemes, the TVD and the ENO schemes, are more appropriate for the computation of weak solutions, especially when these schemes are consistent with the entropy inequality and are second-order or higher in smooth regions. The main distinction between ENO and TVD schemes is that the first can retain higher than first-order terms at extrema while the TVD schemes reduce to spatially first-order in these regions. However, they are more efficient in terms or operations count. The next section lays out the development of TVD schemes.

b. TVD Schemes

Consider a family of five point difference schemes of the form

$$u_i^{n+1} + \lambda\theta\,(h_{i+1/2}^{n+1} - h_{i-1/2}^{n+1}) = u_i^n - \lambda\,(1 - \theta)\,(h_{i+1/2}^n - h_{i-1/2}^n) \qquad (40)$$

where

$$h_{i+1/2}^n = h(u_{n-1}^n, u_i^n, u_{i+1}^n, u_{i+2}^n)$$

and the scheme can be explicit or implicit depending on the value of the parameter θ. If $\theta = 0$, the scheme is explicit; if $\theta = 1/2$, the scheme represents the trapezoid rule; and if $\theta = 1$, the scheme is a backward Euler method.

Defining

$$\overline{h}_{i+1/2} = (1 - \theta)\,h_{i+1/2}^n + \theta h_{i+1/2}^{n+1} \qquad (41)$$

Eq.(40) becomes

$$u_i^{n+1} = u_i^n - \lambda\,(\overline{h}_{i+1/2} - \overline{h}_{i-1/2}) \qquad (42)$$

which is of the form

$$L_1 u^{n+1} = L_2 u^n$$

with L_1 and L_2 defined as the following difference operators

$$L_1 u = u_i + \lambda\theta\,(h_{i+1/2} - h_{i-1/2})$$

$$L_2 u = u_i + \lambda\,(1 - \theta)\,(h_{i+1/2} - h_{i-1/2})$$

The total variation of the mesh u^n is defined as

$$TV(u^n) = \Sigma |u^n_{i+1} - u^n_i| = \Sigma |\Delta_{i+1/2} u^n| \qquad (43)$$

The numerical scheme is TVD if the following inequality holds

$$TV(u^{n+1}) \leq TV(u^n)$$

There are four design principles used in the construction of high-resolution TVD schemes:

- The flux-corrected transport of Boris and Book [Ref. 15]. This is a two step hybrid scheme consisting of a combined first and second-order scheme. It computes an update form of a first-order scheme and then filters the second-order corrections by the use of flux emitters to prevent occurence of new extrema.

- A second-order extension of Gudunov's scheme by van Leer [Ref. 16] and Colella and Woodward [Ref. 17]. This scheme is based on the observation that one can obtain second-order accuracy in Gudunov's scheme by replacing the piecewise-constant initial data of the Reimann problem with piecewise-linear or parabolic initial data. The slope of the initial data is chosen so that no spurious oscillations can occur.

- The modified-flux TVD scheme of Harden [Ref. 18]. This is a technique to design a second-order accurate TVD scheme by starting with a first-order TVD scheme and applying it to a modified flux. The modified flux is chosen so that the scheme is second-order in smooth regions and first-order at extrema.

- The numerical fluctuation approach of Roe [Ref. 19] depending on an average function. The average function is constructed in such a way that spurious oscillations will not occur by the use of flux limiters.

Most of the above methods can be viewed as three-point central-difference schemes with an appropriate numerical dissipation term which automatically controls the amount of numerical dissipation. This control of the dissipation is automatic unlike the control of the numerical dissipation used by central-differencing techniques used in linear theory. The basic idea of the above design principles is to construct a higher-order scheme which

has properties similar to a first-order TVD scheme so that spurious oscillations cannot be generated. In order to achieve that limiting procedure, a flux limiter is used, which imposes constraints on the gradients of the dependent variables or the flux function.

The derivation of the higher-order schemes with TVD properties can be achieved by either following the so-called MUSCL (Monotonic Upstream Scheme for Conservation Laws) approach of van Leer [Ref. 16], Harden [Ref. 18], Roe [Ref. 19] and Osher and Chakravarthy [Ref. 20]; and the non-MUSCL approaches of Roe [Ref. 21] and Yee [Ref.22].

4. Development of Flow Simulation Code

The numerical scheme used for the simulation was developed in Ref. 23. A summary of the numerical scheme is given next.

The general form of the conservation law form for an inertial reference frame is

$$\frac{d}{dt}\int_V \vec{Q}dV + \oint_S \vec{n}\cdot\vec{F}dS = \int_V \nabla\cdot\vec{S}V \qquad (44)$$

The main motivation of the conservation law form is to capture flow discontinuities. Finite volume discetization is obtained by replacing the surface integrals by sums over the faces of a cell. The differential form is obtained by applying Eq.(44) to a cell in physical space. In order to facilitate the numerical computation for complex geometries, the physical space cell (x,z) is the image of the computational domain cell (ξ,ζ) resulting from the generalized coordinate transformation

$$x = x(\xi,\zeta,t) \quad , \quad z = z(\xi,\zeta,t) \qquad (45)$$

The transformed coordinate system (ξ,ζ) is an evenly spaced rectangular domain (orthogonal) having area of unity. This allows all numerical differentiations to be performed with unweighted differencing formulas. In addition, the conservation law form represents the thin-layer approximation. Terms of order $1/Re^{1/2}$ and smaller are neglected, and the viscous terms containing derivatives in the streamwise direction are dropped. These viscous terms are smaller in magnitude than the viscous terms with derivatives normal to the body surface. The thin-layer approximation allows a reduction in computational time, since the streamwise viscous gradients are not usually resolved adequately anyway. Also, the thin-layer approximation allows computation of separated flows and flows with normal pressure gradients. The conventional boundary layer approximation does not allow these computations.

The differential form of the two-dimensional conservation law in generalized coordinates is as follows:

$$\partial_t \hat{Q} + \partial_\xi \hat{E} + \partial_\eta \hat{F} = Re^{-1} \partial_\eta \hat{S} \tag{46}$$

where the transformed vectors are

$$\hat{Q} = \frac{1}{J}\begin{pmatrix} \rho \\ \rho u \\ \rho w \\ e \end{pmatrix}, \quad \hat{E} = \frac{1}{J}\begin{pmatrix} \rho U \\ \rho uU + \xi_x p \\ \rho vU + \xi_z p \\ (e + p)U - \xi_t p \end{pmatrix}, \quad \hat{F} = \frac{1}{J}\begin{pmatrix} \rho W \\ \rho uW + \zeta_x p \\ \rho wW + \zeta_z p \\ (e + p) - \zeta_t p \end{pmatrix} \tag{47}$$

$$\hat{S} = \frac{1}{J}\begin{pmatrix} 0 \\ \mu m_1 u_\zeta + (\mu/3) m_2 \zeta_x \\ \mu m_1 v_\zeta + (\mu/3) m_2 \zeta_y \\ \mu m_1 m_3 + (\mu/3) m_2 + (\zeta_x u + \zeta_y v + \zeta_z w) \end{pmatrix}$$

Here

$$m_1 = \zeta_x^2 + \zeta_z^2$$

$$m_2 = \zeta_x u_\zeta + \zeta_z w_\zeta \tag{48}$$

$$m_3 = (u^2 + w^2)/2 + \kappa Pr^{-1}\left(\frac{\partial a^2}{\partial \zeta}\right)$$

and U and W are the contravariant velocity components given by

$$U = u\xi_x + w\xi_z + \xi_t \tag{49}$$

$$W = u\zeta_x + w\zeta_z + \zeta_t$$

In the above equations, all geometric dimensions are normalized with the chord length; ρ is the density normalized with the freestream density ρ_∞; u and w are the Cartesian velocity components normalized with the speed of sound; e is the total energy per unit volume normalized with $\rho_\infty a_\infty^2$; Pr is the Prandtl number; and κ is the thermal conductivity. The pressure is related to the density and total energy through the equation of state for an ideal gas, $p = (\gamma - 1)[e - \rho(u^2 + w^2)/2]$.

Spatial schemes for the numerical solution of the inviscid part of Eq. (46) are of the following semidiscrete form

$$\frac{dQ}{dt} = -\frac{H_{i,k+1/2} - H_{,i,k-1/2}}{\Delta\xi} - \frac{G_{i,k+1/2} - G_{i,k-1/2}}{\Delta\zeta} \qquad (50)$$

where H and G are the fluxes defined as

$$H_{i+1/2,k} = \frac{1}{2}\left[(E_{i,k} - E_{i+1,k}) - \Delta|E|_{i+1/2,k}\right]$$

with

$$\Delta|E|_{i+1/2,k} = |A|(Q_{i+1,k} - Q_{i,k})$$

$$|A|_{i+1/2,k} = A(\bar{Q}) \,,\, \bar{Q} = \bar{Q}(Q_{i+1,k} - Q_{i,k})$$

Flux difference splitting can be accomplished by enforcing interaction of neighboring states using Roe's approximate Reimann solver, where the interaction is enforced through neighboring cell interfaces. The local time linearization of the difference vectors $\Delta E^{\pm}$ for left and right states Q_L and Q_R, respectively, using Roe's method is obtained as follows

$$\Delta E^{\pm} = A(\bar{Q})^{\pm}\Delta Q \quad , \quad A^{\pm} = R\Lambda^{\pm}R^{-1} \qquad (51)$$

where $\Delta Q = Q_R - Q_L$, $\tilde{A} = (\partial\tilde{E}/\partial\tilde{Q})$ are the flux Jacobian matrices, $\Lambda^{\pm}$ is the eigenvalue diagonal matrix and $\mathbf{R},\mathbf{R}^{-1}$ are the left and right eigenvector matrices. The intermediate state $\tilde{Q}$ is calculated using the Roe variables as

$$\overline{\rho} = \sqrt{\rho_L \rho_R}$$

$$\overline{u} = \frac{u_L\sqrt{\rho_L} + u_R\sqrt{\rho_R}}{\sqrt{\rho_L} + \sqrt{\rho_R}}$$

$$\overline{w} = \frac{w_L\sqrt{\rho_L} + w_R\sqrt{\rho_R}}{\sqrt{\rho_L} + \sqrt{\rho_R}} \qquad (52)$$

$$\overline{h} = \frac{h_L\sqrt{\rho_L} + h_R\sqrt{\rho_R}}{\sqrt{\rho_L} + \sqrt{\rho_R}}$$

The numerical integration scheme is performed using a fully-upwind, factored, implicit, third order accurate numerical scheme. The upwinding is perfomed with flux-difference splitting using Roe's scheme. For complex flow fields first order accurate schemes are too diffusive and they do not produce solutions with reasonable grid spacings. Here a higher order scheme is used. The numerical scheme is given below:

$$[I + h_\xi (\nabla_\xi^b \tilde{A}_{i,k}^+ + \Delta_\xi^f \tilde{A}_{i,k}^-)]^p \times \qquad (53)$$

$$[I + h_\zeta (\nabla_\zeta^b \tilde{C}_{i,k}^+ + \Delta_\zeta^f \tilde{C}_{i,k}^- - Re^{-1}\delta_\zeta \tilde{M}_{i,k})]^p \times (\tilde{Q}_{i,k}^{p+1} - \tilde{Q}_{i,k}^p) =$$

$$-[\tilde{Q}_{i,k}^p - \tilde{Q}_{i,k}^n + h_\xi (\hat{E}_{i+1/2,k} - \hat{E}_{i-1/2,k})^p + h_\zeta (\hat{F}_{i,k+1/2} - \hat{F}_{i,k-1/2})^p$$

$$-Re^{-1} h_\zeta (\hat{S}_{i,k+1/2} - \hat{S}_{i,k-1/2})^p]$$

$H_\xi = \Delta\tau/\Delta\xi$, and Δ, ∇ and δ are the forward, backward and the central difference operators, respectively. The quantities $\hat{E}_{i+1/2,k}$, $\hat{F}_{i,k+1/2}$, $\hat{S}_{i,k+1/2}$ are numerical fluxes.

The accuracy of the numerical solution is improved by subiterations to convergence within each time step iteration. The approximation to $\bar{Q}^{n+1}$ at each subiteration is $\bar{Q}^{p}$. When $p \geq 2$, during a given level of subiteration to convergence, $\bar{Q}^{p} = \bar{Q}^{n+1}$; but when $p = 1$ and no subiterations are performed, then $\bar{Q}^{p} = \bar{Q}^{n}$, and $\bar{Q}^{p+1} = \bar{Q}^{n+1}$. By subiterating to convergence, linearization and factorization errors can be eliminated during the iteration process, because the left hand side of Eq.(53) can be driven to zero. The inviscid fluxes $\bar{E}$ and $\bar{F}$ are evaluated using the Roe upwinding. The numerical fluxes for a third order accurate scheme are given by

$$f_{i,k} = h(q_{i+1,k}, q_{i,k}) - \frac{1}{6}\left[df^{-}_{i+3/2,k} + 2df^{-}_{i+1/2,k}\right] \qquad (54)$$

$$+ \frac{1}{6}\left[2df^{-}_{i+1/2,k} + df^{-}_{i-1/2,k}\right]$$

or in terms in expanded form

$$\tilde{E}_{i+1/2,k} = \frac{1}{2}\left[\tilde{E}(Q_{i,k}, \xi_{i+1/2,k}) - \tilde{E}(Q_{i-1,k}, \xi_{i+1/2,k})\right] \qquad (55)$$

$$- \frac{1}{6}\left[\Delta E^{-}(Q_{i,k}, Q_{i+1,k}, \xi_{i+1/2,k}) + 2\Delta E^{-}(Q_{i+2,k}, Q_{i+1,k}, \xi_{i+3/2,k})\right]$$

$$+ \frac{1}{6}\left[2\Delta E^{+}(Q_{i+1,k}, Q_{i,k}, \xi_{i+1/2,k}) + \Delta E^{+}(Q_{i,k}, Q_{i+1,k}, \xi_{i-1/2,k})\right]$$

Using the notation of Eq.(54), h corresponds to the first order accurate flux, and the df^{+} and df^{-} terms represent the correction terms added to the first order accurate fluxes.

Higher order accurate shock-capturing schemes have some limitations: they may select a nonphysical solution, they produce spurious oscillations and they may develop nonlinear instability in nonsmooth and discontinuous flow regions. More appropriate shock-capturing schemes suitable for the computation of weak solutions are the TVD schemes, described earlier. For this simulation, the Osher-Chakravarthy TVD scheme [Ref. 20] was implemented. This scheme uses flux limiters to impose constaints on the gradient of the fluxes. The flux-limited values are computed as follows:

$$\begin{aligned}
\bar{df}^{-}_{i+3/2,k} &= minmod[df^{-}_{i+3/2,k}, \beta df^{-}_{i+1/2,k}] \\
\bar{df}^{-}_{i+1/2,k} &= minmod[df^{-}_{i+1/2,k}, \beta df^{-}_{i+3/2,k}] \\
\bar{df}^{-}_{i+1/2,k} &= minmod[df^{+}_{i+1/2,k}, \beta df^{+}_{i-1/2,k}] \\
\bar{df}^{-}_{i-1/2,k} &= minmod[df^{+}_{i-1/2,k}, \beta df^{+}_{i+1/2,k}]
\end{aligned} \tag{56}$$

where the *minmod* operator is defined by

$$minmod[x,y] = sign(x)\ x\ max[0,min\{|x|,ysign(x)\}] \tag{57}$$

and the comparison parameter β is in the range $1 \le \beta \le 4$. Substitution of the flux limited values given by Eq.(56) into Eq.(54) makes the entire scheme TVD.

The flux differences ΔE are evaluated by the Roe scheme described earlier. The viscous fluxes $\hat{s}_{i,k+1/2}$ are computed using central differences as shown below

$$\tilde{S}_{i,k+1/2} = \tilde{S}[Q_{i,k+1/2}, (Q_\zeta)_{i,k+1/2}, \zeta_{i,k+1/2}]$$

$$Q_{i,k+1/2} = \frac{1}{2}(Q_{i,k} - Q_{i+1,k}) \tag{58}$$

$$(Q_\zeta)_{i,k+1/2} = Q_{i,k+1} - Q_{i,k}$$

The eigenvalues of the flux Jacobian matrices A ,B are evaluated as suggested in Ref. 24 to prevent expansion shocks. The terms A ,C of the left hand side operators of Eq.(53) have been linearized using the Steger-Warming flux vector splitting. A validation of the viscous flow algorithm for a transonic airfoil is shown in Fig. D2.

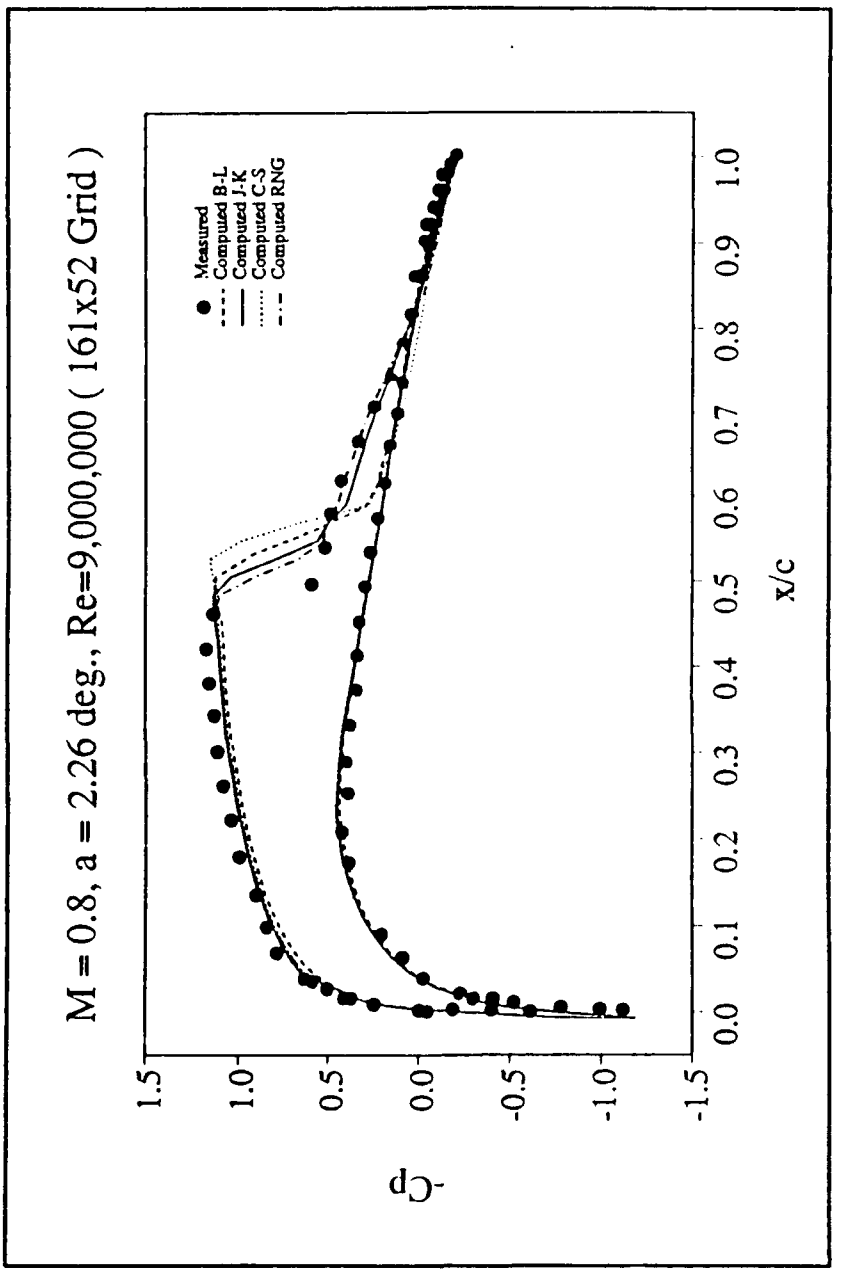

Figure D1. Comparison of Turbulence Model Predictions [Ref. 23]

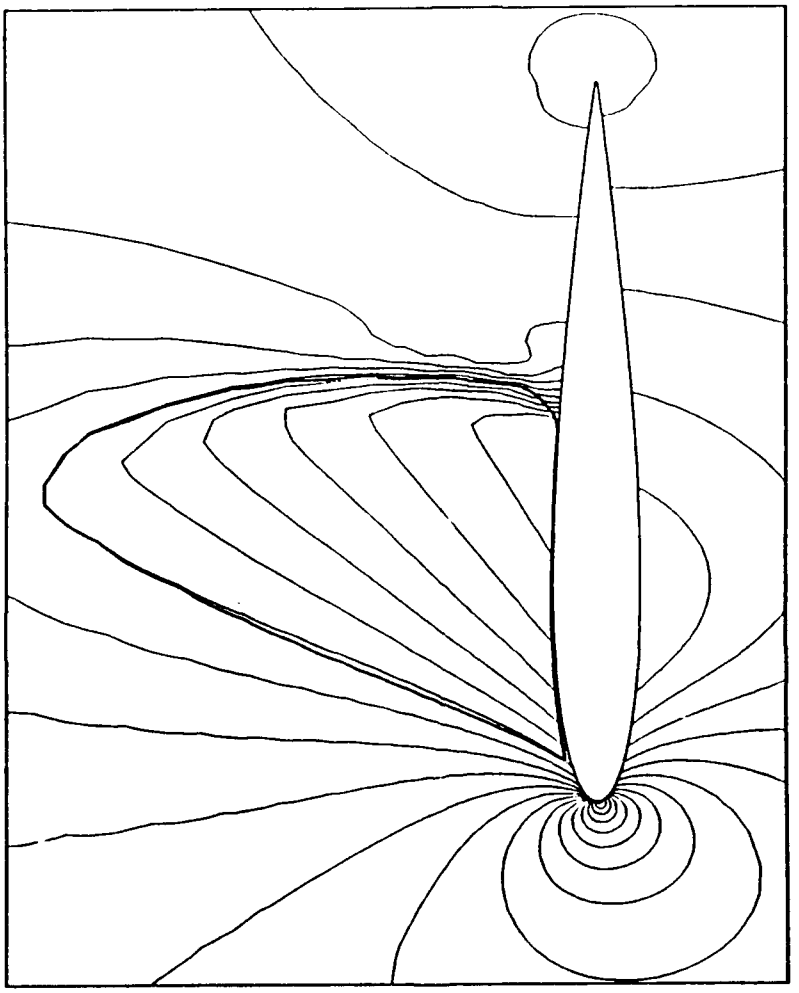

Figure D2. Viscous Flow Validation [Ref. 23]

APPENDIX E

GRAPE

The following is a summary of the grid-generating algorithm GRAPE. Reference 25 provides a detailed explanation of the algorithm theory and Ref. 26 is a detailed user's manual. GRAPE is an algorithm that transforms x and y coordinates in real space to ξ and η coordinates in computational space. GRAPE stands for **GR**ids about **A**irfoils using **P**oisson's **E**quation. $\eta = 0$ forms the inner boundary of the grid, and $\eta = \eta_{max}$ forms the outer boundary. For the C-grids, $\xi = 0$ is located at the rear boundary, and ξ moves forward clockwise around the airfoil until it reaches ξ_{max} at the rear boundary again. The mapping functions are required to satisfy the following:

$$\xi_{xx} + \xi_{yy} = P \tag{1a}$$

$$\eta_{xx} + \eta_{yy} = Q \tag{1b}$$

The following relations are useful in transforming the equations from real space to computational space:

$$\xi_x = y_\eta / J \tag{2a}$$

$$\xi_y = -x_\eta / J \tag{2b}$$

$$\eta_x = -y_\xi / J \tag{2c}$$

$$\eta_y = x_\xi / J \tag{2d}$$

where

$$J = x_\xi y_\eta - x_\eta y_\xi \tag{2e}$$

Applying Eqns. (2) to (1) yields the following transformed Poisson Equations:

$$\sigma x_{\xi\xi} - 2\mu x_{\xi\eta} + \tau x_{\eta\eta} = -J^2(Px_{\xi} + Qx_{\eta}) \tag{3a}$$

$$\sigma y_{\xi\xi} - 2\mu y_{\xi\eta} + \tau y_{\eta\eta} = -J^2(Py_{\xi} + Qy_{\eta}) \tag{3b}$$

where

$$\sigma = x_{\eta}^2 + y_{\eta}^2 \tag{3c}$$

$$\mu = x_{\xi}x_{\eta} + y_{\xi}y_{\eta} \tag{3d}$$

$$\tau = x_{\xi}^2 + y_{\xi}^2 \tag{3e}$$

Solving Eqn. (3) for a particular choice of inhomogeneous terms P and Q (forcing functions) and a particular set of boundary conditions causes the grid to be generated.

There is latitude that exists with the choices of P and Q. Different choices of P and Q result in different grids. In an effort to choose P and Q to allow reasonable effort in the computation, P and Q are redefined in terms of four new variables. In addition to geometric constraints and the original Poisson equations, six equations with six unknowns are left. These equations can be solved in a straightforward iterative scheme.

The following geometric constraints are imposed on the grid:

1. Spacing along ξ = constant lines between the body at $\eta = 0$ and next grid node $\eta = 1$ is specified by the user

2. The angle of intersection between the body and ξ = constant lines is specified by the user

3. Same geometric constraint as 1) but applied to the outer boundary

4. Same geometric constraint as 2) but applied to the outer boundary

These geometric constraints are embedded in the P and Q terms.

The program uses a method called Coarse-Fine Sequencing (CFS). This method greatly accelerates the numerical convergence of the program. The coarse solution solves the grid at every third point in the α direction and every third point in the β direction. The fine solution uses a cubic spline fit to find the rest of the points.

Reference 27 details changes made to the original GRAPE code to allow the generation of periodic cascade C-grids for turbomachinery flow. In addition, the outer and inner boundary routines were modified. All the features of the original GRAPE code were retained.

APPENDIX F

GRAPE INPUT FILES

```
$GRID1
JMAX=199,KMAX=64,NTETYP=3,NAIRF=5,JAIRF=316,NIBDST=3,
NDS=2,DSI=0.001,JTEBOT=13,JTETOP=187,XLE=0,XTE=1,NOBSHP=4,NOBDST=1,
XLEFT=-0.3,
XRIGHT=1.5,YBOTOM=-0.276,YTOP=0.276,RCORN=0.20,ALAMF=1.0,ALAMR=0.0,
NORDA=4,1,
MAXITA=10,10,JPRT=-1,NOUT=0
$END
$GRID2
XTFRAC=1.0,ROTANG=0.0,WAKEP=1.0
$END
$GRID3
AIRFX = 6.00000,5.99948,5.99891,5.99815,5.99667,
        5.99481,5.99264,5.99106,5.98939,5.98766,
        5.98500,
        5.98200,5.97870,5.97507,5.97108,5.96668,
        5.96185,5.95654,5.95069,5.94426,5.93719,
        5.92941,5.92085,5.91143,5.90108,5.88968,
        5.87715,5.86337,5.84820,5.83152,5.81318,
        5.79299,5.77079,5.74637,5.71951,5.68996,
        5.65745,5.62170,5.58237,5.53911,5.49152,
        5.43917,5.38159,5.31825,5.25556,5.19286,
        5.13016,5.06747,5.00477,4.94208,4.87938,
        4.81668,4.75399,4.69129,4.62860,4.56590,
        4.50320,4.44051,4.37781,4.31512,4.25242,
        4.18973,4.12703,4.06433,4.00164,3.93894,
        3.87625,3.81355,3.75085,3.68816,3.62546,
        3.56277,3.50007,3.43738,3.37468,3.31198,
        3.24929,3.18659,3.12390,3.06120,2.99850,
        2.93581,2.87311,2.81042,2.74772,2.68503,
        2.62233,2.55963,2.49694,2.43424,2.37155,
        2.30885,2.24616,2.18346,2.12076,2.05807,
        1.99537,1.93268,1.86998,1.80728,1.74459,
        1.68189,1.61920,1.55650,1.49381,1.43111,
        1.36841,1.30572,1.24302,1.18033,1.11763,
        1.05493,0.99224,0.92954,0.86685,0.80415,
        0.74146,
        0.67876,0.61541,0.55783,0.50548,0.45789,
        0.41460,0.37530,0.33955,0.30704,0.27749,
        0.25063,0.22621,0.20401,0.18383,0.16548,
        0.14880,0.13363,0.11985,0.10732,0.09593,
        0.08557,0.07615,0.06759,0.05981,0.05274,
        0.04631,0.04046,0.03515,0.03032,0.02592,
        0.02193,0.01830,0.01500,
        0.01369,0.01112,0.00987,0.00750,0.00536,
        0.00351,0.00201,0.00091,0.00023,
        0.00000,0.00023,0.00091,0.00201,0.00351,
        0.00536,0.00750,0.00987,0.01112,0.01369,
        0.01699,0.02062,0.02461,0.02901,0.03384,
        0.03915,0.04500,0.05143,0.05850,0.06628,
        0.07483,0.08426,0.09462,0.10601,0.11854,
        0.13232,0.14749,0.16417,0.18252,0.20270,
        0.22490,0.24932,0.27887,0.31138,0.34713,
        0.38646,0.42972,0.47731,0.52966,0.58724,
        0.65058,0.71308,0.77608,0.83908,0.90208,
        0.96508,1.02508,1.09108,1.15108,1.21408,
        1.27708,1.34008,1.40308,1.46608,1.52908,
        1.59208,1.65208,1.71508,1.77808,1.84108,
        1.90408,1.96708,2.03008,2.09308,2.15608,
```

Figure F1. GRAPE Input for Channel C-grid

```
                  2.21908,2.28208,2.34208,2.40508,2.46808,
                  2.53108,2.59408,2.65708,2.72008,2.78308,
                  2.85000,2.92118,2.99378,3.05371,3.11665,
                  3.17956,3.24256,3.30553,3.36851,3.43149,
                  3.49449,3.55748,3.61749,3.68049,3.74349,
                  3.80648,3.86948,3.93247,3.99546,4.05844,
                  4.12141,4.18137,4.24431,4.30725,4.37108,
                  4.43309,4.49598,4.55886,4.62171,4.68455,
                  4.74736,4.81015,4.87292,4.93566,4.99837,
                  5.06105,5.12371,5.18633,
                  5.24892,5.31849,5.38183,
                  5.43945,5.49176,5.53935,5.58262,5.62195,
                  5.65770,5.68899,5.71975,5.74662,5.77104,
                  5.79324,5.81350,5.83177,5.84845,5.86361,
                  5.87740,5.88993,5.90132,5.91168,5.92109,
                  5.92965,5.93743,5.94451,5.95094,5.95678,
                  5.96210,5.96741,5.97224,5.97664,5.98063,
                  5.98426,
                  5.98756,5.98930,5.99097,5.99256,5.99474,
                  5.99603,5.99810,5.99888,5.99945,6.00000,
          AIRFY = 0.01500,0.01109,0.00940,0.00779,0.00557,
                  0.00365,0.00209,0.00128,0.00066,0.00024,
                  0.00000,
                  0.00000,0.00000,0.00000,0.00000,0.00000,
                  0.00000,0.00000,0.00000,0.00000,0.00000,
                  0.00000,0.00000,0.00000,0.00000,0.00000,
                  0.00000,0.00000,0.00000,0.00000,0.00000,
                  0.00000,0.00000,0.00000,0.00000,0.00000,
                  0.00000,0.00000,0.00000,0.00000,0.00000,
                  0.00000,0.00000,0.00000,0.00000,0.00000,
                  0.00000,0.00000,0.00000,0.00000,0.00000,
                  0.00000,0.00000,0.00000,0.00000,0.00000,
                  0.00000,0.00000,0.00000,0.00000,0.00000,
                  0.00000,0.00000,0.00000,0.00000,0.00000,
                  0.00000,0.00000,0.00000,0.00000,0.00000,
                  0.00000,0.00000,0.00000,0.00000,0.00000,
                  0.00000,0.00000,0.00000,0.00000,0.00000,
                  0.00000,0.00000,0.00000,0.00000,0.00000,
                  0.00000,0.00000,0.00000,0.00000,0.00000,
                  0.00000,0.00000,0.00000,0.00000,0.00000,
                  0.00000,0.00000,0.00000,0.00000,0.00000,
                  0.00000,0.00000,0.00000,0.00000,0.00000,
                  0.00000,0.00000,0.00000,0.00000,0.00000,
                  0.00000,0.00000,0.00000,0.00000,0.00000,
                  0.00000,
                  0.00000,0.00000,0.00000,0.00000,0.00000,
                  0.00000,0.00000,0.00000,0.00000,0.00000,
                  0.00000,0.00000,0.00000,0.00000,0.00000,
                  0.00000,0.00000,0.00000,0.00000,0.00000,
                  0.00000,0.00000,0.00000,0.00000,0.00000,
                  0.00000,0.00000,0.00000,0.00000,0.00000,
                  0.00000,0.00000,0.00000,
                  0.00006,0.00051,0.00091,0.00201,0.00351,
                  0.00536,0.00750,0.00987,0.01240,0.01500,
                  0.01761,0.02013,0.02250,0.02464,0.02640,0.02799,
                  0.02910,0.02940,0.02994,
                  0.03015,0.03034,0.03061,0.03089,0.03118,
                  0.03150,0.03186,0.03225,0.03272,0.03316,
                  0.03364,0.03426,0.03493,0.03559,0.03639,
                  0.03720,0.03813,0.03915,0.04025,0.04150,
```

Figure F1 (cont). GRAPE Input for Channel C-grid

```
          0.04282,0.04436,0.04612,0.04814,0.05034,
          0.05272,0.05539,0.05830,0.06153,0.06502,
          0.06887,0.07273,0.07658,0.08043,0.08428,
          0.08814,0.09181,0.09584,0.09951,0.10337,
          0.10722,0.11107,0.11493,0.11878,0.12263,
          0.12649,0.13016,0.13401,0.13786,0.14172,
          0.14557,0.14942,0.15328,0.15713,0.16098,
          0.16484,0.16869,0.17236,0.17621,0.18007,
          0.18392,0.18777,0.19163,0.19548,0.19933,
          0.20342,0.20763,0.21145,0.21434,0.21709,
          0.21955,0.22172,0.22359,0.22517,0.22645,
          0.22745,0.22814,0.22854,0.22866,0.22850,
          0.22804,0.22728,0.22623,0.22489,0.22326,
          0.22133,0.21923,0.21673,0.21394,0.21085,
          0.20747,0.20380,0.19984,0.19558,0.19103,
          0.18619,0.18106,0.17563,0.16991,0.16390,
          0.15760,0.15101,0.14412,
          0.13695,0.12859,0.12073,
          0.11328,0.10630,0.09977,0.09367,0.08802,
          0.08278,0.07811,0.07345,0.06931,0.06551,
          0.06201,0.05879,0.05585,0.05316,0.05064,
          0.04841,0.04634,0.04444,0.04271,0.04113,
          0.03969,0.03781,0.03717,0.03608,0.03508,
          0.03417,0.03326,0.03242,0.03167,0.03098,
          0.03035,
          0.02978,0.02937,0.02876,0.02796,0.02641,
          0.02451,0.02230.0.02069,0.01901,0.01500,
$END
```

Figure F1 (cont). GRAPE Input for Channel C-grid

```
$GRID1
JMAX=169, KMAX=40, NTETYP=3, NAIRF=5, NIBDST=7, NOBSHP=7,
JAIRF=316, JTEBOT= 25, JTETOP=145, NORDA=0,3, MAXITA=  0,50, NOUT=4,
DSI=.0025, XLE=0.0, XTE=0.61786,
XLEFT=-0.3089, XRIGHT=1.235, RCORN= 0.0333,
$END
$GRID2
NOBCAS=0, NLE=20, NTE= 10, DSPA= 0.5,
DSLE= 0.0005, DSTE= 0.0010, PITCH= 0.50,
YSCL=1.0 , XTFRAC=0.8 , ROTANG= -51.84,
WAKEP= 0.8,
$END
$GRID3
AIRFX=
        6.00000, 5.99948, 5.99891, 5.99815, 5.99667
        5.99481, 5.99264, 5.99106, 5.98939, 5.98766,
        5.98500,
        5.98200, 5.97870, 5.97507,5.97108,5.96668,
        5.96185, 5.95654, 5.95069,5.94426,5.93719,
        5.92941, 5.92085, 5.91143,5.90108,5.88968,
        5.87715, 5.86337, 5.84820,5.83152,5.81318,
        5.79299, 5.77079, 5.74637,5.71951,5.68996,
        5.65745, 5.62170, 5.58[illegible].53911 5.49152,
        5.43917, 5.38159, 5.[illegible].25556,5.19286,
        5.13016, 5.06747, [illegible].00477,4.94208,4.87938,
        4.81668, 4.[illegible]99, 4.69129,4.62860,4.56590,
        4.5032[illegible], 4.44051, 4.37781,4.31512,4.25242,
        4.[illegible]8973, 4.12703, 4.06433,4.00164,3.93894,
        3.87625, 3.81355, 3.75085,3.68816,3.62546,
        [illegible] 56277, 3.[illegible]50007, 3.43738,3.37468,3.31198,
        3.24929, 3.[illegible], 3.1[illegible]0,3.06120,2.99850,
        2.93581, 2.87311, 2.81042,2.74772,2.68503,
        2.62233, 2.55963, 2.49694,2.43424,2.37155,
        2.30885, 2.24616, 2.18346,2.12076,2.05807,
        1.99537, 1.93268, 1.86998,1.80728,1.74459,
        1.68189, 1.61920, 1.55650,1.49381,1.43111,
        1.36841, 1.30572, 1.24302,1.18033,1.11763,
        1.05493, 0.99224, 0.92954,0.86685,0.80415,
        0.74146,
        0.67876, 0.61541, 0.55783,0.50548,0.45789,
        0.41460, 0.37530, 0.33955,0.30704,0.27749,
        0.25063, 0.22621, 0.20401,0.18383,0.16548,
        0.14880, 0.13363, 0.11985,0.10732,0.09593,
        0.08557, 0.07615, 0.06759,0.05981,0.05274,
        0.04631, 0.04046, 0.03515,0.03032,0.02592,
        0.02193, 0.01830, 0.01500,
        0.01369, 0.01112, 0.00987,0.00750,0.00536,
        0.00351, 0.00201, 0.00091,0.00023,
        0.00000, 0.00023, 0.00091,0.00201,0.00351,
        0.00536, 0.00750, 0.00987,0.01112,0.01369,
        0.01699, 0.02062, 0.02461,0.02901,0.03384,
        0.03915, 0.04500, 0.05143,0.05850,0.06628,
        0.07483, 0.08426, 0.09462,0.10601,0.11854,
        0.13232, 0.14749, 0.16417,0.18252,0.20270,
        0.22490, 0.24932, 0.27887,0.31138,0.34713,
        0.38646, 0.42972, 0.47731,0.52966,0.58724,
        0.65058, 0.71308, 0.77608,0.83908,0.90208,
        0.96508, 1.02508, 1.09108,1.15108,1.21408,
        1.27708, 1.34008, 1.40308,1.46608,1.52908,
        1.59208, 1.65208, 1.71508,1.77808,1.84108,
```

Figure F2. GRAPE Input for Cascade C-grid

```
          1.90408, 1.96708, 2.03008,2.09308,2.15608,
          2.21908, 2.28208, 2.34208,2.40508,2.46808,
          2.53108, 2.59408, 2.65708,2.72008,2.78308,
          2.85000, 2.92118, 2.99378,3.05371,3.11665,
          3.17956, 3.24256, 3.30553,3.36851,3.43149,
          3.49449, 3.55748, 3.61749,3.68049,3.74349,
          3.80648, 3.86948, 3.93247,3.99546,4.05844,
          4.12141, 4.18137, 4.24431,4.30725,4.37108,
          4.43309, 4.49598, 4.55886,4.62171,4.68455,
          4.74736, 4.81015, 4.87292,4.93566,4.99837,
          5.06105, 5.12371, 5.18633,
          5.24892, 5.31849, 5.38183,
          5.43945, 5.49176, 5.53935,5.58262,5.62195,
          5.65770, 5.68899, 5.71975,5.74662,5.77104,
          5.79324, 5.81350, 5.83177,5.84845,5.86361,
          5.87740, 5.88993, 5.90132,5.91168,5.92109,
          5.92965, 5.93743, 5.94451,5.95094,5.95678,
          5.96210, 5.96741, 5.97224,5.97664,5.98063,
          5.98426,
          5.98756, 5.98930, 5.99097,5.99256,5.99474,
          5.99603, 5.99810, 5.99888,5.99945,6.00000,
AIRFY=
          0.01500,0.01109,0.00940,0.00779,0.00557,
          0.00365,0.00209,0.00128,0.00066,0.00024,
          0.00000,
          0.00000,0.00000,0.00000,0.00000,0.00000,
          0.00000,0.00000,0.00000,0.00000,0.00000,
          0.00000,0.00000,0.00000,0.00000,0.00000,
          0.00000,0.00000,0.00000,0.00000,0.00000,
          0.00000,0.00000,0.00000,0.00000,0.00000,
          0.00000,0.00000,0.00000,0.00000,0.00000,
          0.00000,0.00000,0.00000,0.00000,0.00000,
          0.00000,0.00000,0.00000,0.00000,0.00000,
          0.00000,0.00000,0.00000,0.00000,0.00000,
          0.00000,0.00000,0.00000,0.00000,0.00000,
          0.00000,0.00000,0.00000,0.00000,0.00000,
          0.00000,0.00000,0.00000,0.00000,0.00000,
          0.00000,0.00000,0.00000,0.00000,0.00000,
          0.00000,0.00000,0.00000,0.00000,0.00000,
          0.00000,0.00000,0.00000,0.00000,0.00000,
          0.00000,0.00000,0.00000,0.00000,0.00000,
          0.00000,0.00000,0.00000,0.00000,0.00000,
          0.00000,0.00000,0.00000,0.00000,0.00000,
          0.00000,0.00000,0.00000,0.00000,0.00000,
          0.00000,0.00000,0.00000,0.00000,0.00000,
          0.00000,0.00000,0.00000,0.00000,0.00000,
          0.00000,0.00000,0.00000,0.00000,0.00000,
          0.00000,0.00000,0.00000,
          0.00006,0.00051,0.00091,0.00201,0.00351,
          0.00536,0.00750,0.00987,0.01240,0.01500,
          0.01761,0.02013,0.02250,0.02464,0.02640,0.02799,
          0.02910,0.02940,0.02994,
          0.03015,0.03034,0.03061,0.03089,0.03118,
          0.03150,0.03186,0.03225,0.03272,0.03316,
```

Figure F2 (cont). GRAPE Input for Cascade C-grid

```
          0.03364,0.03426,0.03493,0.03559,0.03639,
          0.03720,0.03813,0.03915,0.04025,0.04150,
          0.04282,0.04436,0.04612,0.04814,0.05034,
          0.05272,0.05539,0.05830,0.06153,0.06502,
          0.06887,0.07273,0.07658,0.08043,0.08428,
          0.08814,0.09181,0.09584,0.09951,0.10337,
          0.10722,0.11107,0.11493,0.11878,0.12263,
          0.12649,0.13016,0.13401,0.13786,0.14172,
          0.14557,0.14942,0.15328,0.15713,0.16098,
          0.16484,0.16869,0.17236,0.17621,0.18007,
          0.18392,0.18777,0.19163,0.19548,0.19933,
          0.20342,0.20763,0.21145,0.21434,0.21709,
          0.21955,0.22172,0.22359,0.22517,0.22645,
          0.22745,0.22814,0.22854,0.22866,0.22850,
          0.22804,0.22728,0.22623,0.22489,0.22326,
          0.22133,0.21923,0.21673,0.21394,0.21085,
          0.20747,0.20380,0.19984,0.19558,0.19103,
          0.18619,0.18106,0.17563,0.16991,0.16390,
          0.15760,0.15101,0.14412,
          0.13695,0.12859,0.12073,
          0.11328,0.10630,0.09977,0.09367,0.08802,
          0.08278,0.07811,0.07345,0.06931,0.06551,
          0.06201,0.05879,0.05585,0.05316,0.05064,
          0.04841,0.04634,0.04444,0.04271,0.04113,
          0.03969,0.03781,0.03717,0.03608,0.03508,
          0.03417,0.03326,0.03242,0.03167,0.03098,
          0.03035,
          0.02978,0.02937,0.02876,0.02796,0.02641,
          0.02451,0.02230,0.02069,0.01901,0.01500,
$END
```

Figure F2 (cont). GRAPE Input for Cascade C-grid

LIST OF REFERENCES

1. United Technologies Research Center Report R90-957946, Transonic Fan Shock-Boundary Layer Separation Control, April 1990.
2. AIAA Paper 91-0042, Exploratory Study of Vortex-Generating Devices for Turbulent Flow Separation Control, by J.C. Lin, G.V. Selby and F.G. Howard, January 1991.
3. Aero Note 110, The Use of Air Jets for Boundary Layer Control, by Wallis, R.A., Aerodynamics Research Laboratory, Australia, 1952.
4. Johnston, J.P., and Nishi, M., Vortex Generator Jets - Means for Flow Separation Control, AIAA Journal, v.28, No.6, pp. 989-994, June 1990.
5. Demo, W.J.,Jr., Cascade Wind Tunnel for Transonic Blade Studies, Master's Thesis, Naval Postgraduate School, June 1978.
6. Volland, K.F.,Jr., Transonic Cascade Wind Tunnel Modification and Initial Tests, Master's Thesis, Naval Postgraduate School, June 1980.
7. Geopfarth, R.N., Development of a Device for the Incorportation of Multiple Scanivalves into a Computer-Controlled Data System, Master's Thesis, Naval Postgraduate School, March 1979.
8. Hegland, M.G., Investigation of a Mach 1.4 Compressor Cascade with Variable Back Pressure using Flow Visualization, Master's Thesis, Naval Postgraduate School, March 1986.

9. Schlichting, H., Boundary Layer Theory, pp. 47-68, McGraw-Hill Co., Seventh Edition, 1979.

10. NASP Technical Memorandum 1087, Turbulence Modeling in Hypersonic Flows, by J.G. Marvin and T.J. Coakley, November 1989.

11. NASA TM X-62248, The Turbulent Mean Flow, Reynolds-Stresses, and Heat Flux Equations in Mass-Averaged Dependent Variables, by M.W. Rubesin and W.C. Rose, 1973.

12. Johnson, D.A., and King, L.S., A Mathematically Simple Turbulence Closure Model for Attached and Separated Turbulent Boundary Layers, AIAA Journal, v.23, No. 11, pp. 1684-1692, November 1985.

13. AIAA Paper 78-257, Thin Layer Approximation and Algebraic Model for Separated Turbulent Flows, by Baldwin, B.S., and Lomax, H., January 1978.

14. Lax, P.D. and Wendroff, B., System of Conservation Laws, Community of Pure Applied Mathematics, v. 13, pp. 217-237, 1960.

15. Boris, J.P., and Book, D.L., Flux-Corrected Transport. I. SHASTA, A Fluid Transport Algorithm that Works, Journal of Computational Physics, v. 11, pp. 38-69, 1973.

16. Van Leer, Towards the Ultimate Conservation Difference Scheme V, A Second-Order Sequel to Gudunov's Method, Journal of Computational Physics, v. 32, pp. 101-136, 1979.

17. Collela, P. and Woodward, P.R., Piecewise Parabolic Method (PBM) for Gas Dynamical Simulations, Journal of Computational Physics, v. 54, pp. 174-201, 1984.

18. Harden, H., On a Class of High-Resolution Total-Variation-Stable Finite Difference Schemes, SIAM Journal of Numerical Analysis, v. 21, pp. 1-23, 1984.

19. Roe, P.L.,Some Contributions to the Modeling of Discontinuous Flows, Lectures in Applied Mathematics, v. 22, 1985.

20. Osher, S., and Chakravarthy, S.,Very High-Order Accurate TVD Schemes, The IMA Volumes in Mathematics and its Applications, v. 2, Springer-Verlag, pp. 229-382, March 1986.

21. Roe, P.L., Generalized Formulation of TVD Lax-Wendroff Schemes, ICASE Report No. 84-53, October 1984.

22. Yee, H.C., Construction of Explicit and Implicit Symmetric TVD Schemes and their Applications, Journal of Computational Physics, v. 68, pp. 151-179, 1987.

23. Ekaterinaris, J.A., Airfoil Flow Predictions with an Upwind Scheme using Algebraic and One-Equation Turbulence Models, paper submitted to the Journal of Fluid Mechanics, March 1991.

24. NASA TM-84323, Implicit Total Variation Diminishing (TVD) Schemes for Steady State Calculations, by Yee, H.C., Warming, R.F., and Harden, A., 1983.

25. NASA Technical Memorandum 81198, A Computer Program to Generate Two-Dimensional Grids About Airfoils and Other Shapes by the Use of Poisson's Equation, by R.L. Sorenson, May 1980.

26. Steger, J.L., and Sorenson, R.L., Automatic Mesh Point Clustering Near a Boundary in Grid Generation with Elliptic Partial Differential Equations, Journal of Computational Physics, v. 33, No. 3, pp. 405-410, December 1979.

27. NASA Lewis Research Center, M.S. 77-6, Revised Grape Code Input for Cascades, by R.V. Chima, June 1990.